EXCLUSIVE TWO BODY DECAYS OF THE BOTTOM MESON

By

JORGE LUIS RODRIGUEZ

A DISSERTATION PRESENTED TO THE GRADUATE SCHOOL OF THE UNIVERSITY OF FLORIDA IN PARTIAL FULFILLMENT OF THE REQUIREMENTS FOR THE DEGREE OF DOCTOR OF PHILOSOPHY

UNIVERSITY OF FLORIDA

1995

A Lori y a mi Familia

ACKNOWLEDGEMENTS

First of all, I would like to acknowledge the contributions made to this analysis by the entire CLEO collaboration and the CESR machine staff. With out their dedicated efforts none of the work described in the following pages would have been possible. The machines studies staff have created the highest luminosity e^+e^- accelerator in the world, which provided the huge data sample essential to the successful completion of this work. The tireless efforts of the CLEO run managers, J. Kandaswamy and Richard Ehrlich made possible the smooth running of the detector, essential in gathering the large data sample. None of the splendid equipment used for this analysis would have been available without the support of the American Public, whose tax dollars and elected representatives have supported Big Science for the better part of this century. My thanks to John Q. Public.

I would also like to thank the individuals who have contributed to my graduate student experience here at Florida. First I would like to express my deep gratitude to Paul Avery, my advisor, for his inspiring lectures which greatly influenced my decision to pursue high energy physics. I will always admire and respect him for his intellect, his curiosity and his enthusiasm. He has also been provided our group with a wealth of computer resources which I will truly miss. I greatly appreciate John Yelton's help and advice with the many questions I put to him. I found uncanny his ability to plow right through a problem, and when arriving at a solution, explaining it clearly enough even for me. Finally, I would like to thank Dr. Pierre Ramond for his wonderful lectures on the Standard Model. The few hours I spent in his lectures will always remind me of why I stay in this field. Moments of understanding are what make it all worth while.

This thesis would not have been possible without the direction and guidance of Professor Tom Browder who rescued me from the clutches of PASS2 and guided me to the interesting work discussed in this dissertation. Working with him on the big B paper was a truly rewarding and stimulating experience. I would also like to thank Bill Ross and Arne Fryberger, who not only helped me with analysis problems, but also made the four Summers I spent in Ithaca truly pleasant.

I have been most fortunate in being amongst a group of friends who made my stay in Gainesville both enjoyable and interesting. Two of these guys, Sam Mikaelian and Chandra Chegireedy have not only been good friends, but have contributed to my development as an experimentalist. Sam provided me with many insights in particle theory and physics in general. He was always willing and eager to answer questions, as long as he could throw in a couple of mild but witty insults. Chandra answered my computer related questions succinctly and without arrogance. Although he and I butted heads on occasion, I know that pound for pound he is the best system manager around.

I would also like to acknowledge the sacrifices made by my new wife Lori and my family in Miami. I will never be able to express the gratitude I feel for what these individuals have contributed to my life. Lori especially, has stuck with me even though I have not paid her the attention she truly deserves. She has made graduate student life enjoyable and most importantly sane. Without her I would be lost and my life would be pointless. Finally, I would like to thank my rather large and boisterous extended family for their support throughout the years. My uncle Pepe and his family especially, for keeping me away from serious trouble during my adolescence. The thought of them all in one place has given me a sense of home and belonging. It is one of my greatest pleasures to go home frequently to visit, especially my brother Juan, his kids, Matthew and Steven, his wife Yvonne and their most recent addition Stephanie. Also, I thank my father Ornaldo for moving us to America and both my parents for raising and giving me life. I have been especially close to my mother throughout my life and have thought of her often in moments of weakness and despair. Her great courage will forever be an inspiration to me. Everything I come to achieve will be a direct result of her efforts.

TABLE OF CONTENTS

LIST OF TABLES

LIST OF FIGURES

Figure | Page

Abstract of Dissertation Presented to the Graduate School
of the University of Florida in Partial Fulfillment of the
Requirements for the Degree of Doctor of Philosophy

EXCLUSIVE TWO BODY DECAYS
OF THE BOTTOM MESON

By

Jorge Luis Rodriguez

August 1995

Chairman: Paul R. Avery
Major Department: Physics

Hadronic two body decays of bottom mesons to a single charmed meson plus a "light" pseudoscalar, vector or axial-vector meson are fully reconstructed using data collected with the CLEO II detector at the CESR e^+e^- storage ring. The data sample used consists of 2.04 fb^{-1} on and 0.97 fb^{-1} just below $B\bar{B}$ threshold. Branching ratios and final state polarizations are measured for three classes of bottom meson decays, $B^0 \rightarrow D^{(*)+}X^-$, $B^0 \rightarrow D^{(*)0}X^0$ and $B^- \rightarrow D^{(*)0}X^-$ where X is either a π, ρ or a_1. The results are used to determine the BSW parameters a_1, a_2 and the relative sign of a_2/a_1. The results are also found to be consistent with both the factorization hypothesis and color suppression.

CHAPTER 1
INTRODUCTION AND THE STANDARD MODEL

1.1 The Fundamental Particles

In the standard model all matter is composed of electrically charged fundemental particles known as quarks and leptons. Ordinary matter, that is atoms and molecules, consists of two types of quarks, the up and down quarks arranged into protons and neutrons (nucleons), and one type of lepton, the electron. The nucleons are confined in the nucleus while electrons are found in quantum mechanical orbits in and around the center of the atom or molecule. The quarks differ from leptons in two fundamental ways: they have fractional electric charge and possess, in addition, a distinct quantum number analogous to the electric charge known as color. The color charges come in three different varieties known commonly as red (R), green (G) and blue (B) and give rise to the strong interactions. Since quarks are endowed with both electric and color charges they, unlike leptons, are influenced by both electromagnetic and strong forces.

The up and down quarks and the electron with its doublet partner, the electron neutrino, make up the first fermionic generation from which all of the familiar matter is constructed. We now know that two more generations of doublet pairs exist; they duplicate almost exactly the first generation but possess significantly larger masses. These two new generations consist of doublets with progressively heavier masses culminating with the recently discovered top

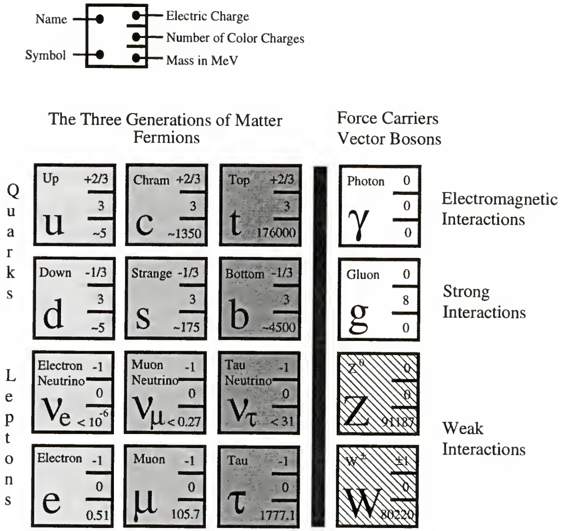

Figure 1.1 The fundamental particles.

quark with a mass of 176 GeV (roughly the mass of a tungsten atom) [1]. Additional generations with neutrino masses less then 45 GeV have been ruled out by LEP measurement on the width of the Z^0. The origin of the heavier generations remains a mystery.

In addition to the fermions (spin-half particles) a set of fundamental integer spin particles known as vector bosons are known to exist. These particles mediate the weak, electromagnetic, strong and gravitational forces. † In quantum field theories, particle interactions are a result of the exchange of gauge bosons. For example, the photon is the particle exchanged in electromagnetic interactions. Its exchange mediates electromagnetic interactions and thus all chemical and light phenomena can, in principle, be described as a consequence of the exchange of the photon. Eight gauge bosons, known as gluons, mediate the strong interactions which bind quarks into hadrons and nucleons into nuclei. Both gluons and photons are massless and are the force carriers or "gauge quanta" of the theories describing the dynamics of the respective interactions. In weak interactions three spin-one fundamental bosons, two with opposite electric charge, and one with no charge are exchanged. Unlike the force carriers of the strong and electromagnetic interactions the weak force carriers are massive. The weak interaction allows quark and lepton species to transform amongst themselves and is responsible for radioactive beta decay in heavy nuclei. The fermions and vector bosons are listed in Figure 1.1 with their approximate masses, intrinsic charge electric and number of color charges.

1.2 The Elementary Particles

Particles with quantum numbers consistent with those associated with free quarks have never been observed in isolation. This has led physicists to postulate that the strong interactions exhibit a property known as color confinement. The hypothesis asserts that quarks are so strongly bound within hadrons that they can not escape as isolated entities but must combine with other quarks

† A spin two boson is postulated as the carrier of the gravitational force. Gravitational interactions between subatomic particles, however, are negligible when compared to the other three forces and are thus excluded from further discussion.

into final states which posses no net color. In the language of group theory a state which possess no net charge is known as a color-singlet.

As already stated quarks come in three varieties, red, green and blue. These compose a fundamental triplet representation under the color $SU(3)_C$ symmetry. To form hadrons we look for quark combinations which transform as singlets under $SU(3)_C$. The simplest of these are a quark anti-quark pair and the three quark combination of red, green and blue quarks. These particle combinations correspond to the following direct product decomposition of irreducible $SU(3)$ representations

$$3 \otimes \bar{3} = 8 \oplus 1 \quad \text{and} \quad 3 \otimes 3 \otimes 3 = 10 \oplus 8 \oplus 8 \oplus 1. \tag{1.1}$$

The quark anti-quark pair forms an octet and a singlet and is known as the meson nonet. The states in the three quark decomposition, properly symmetrized, are known as baryons.

Of particular interest to this analysis are the "heavy flavor" mesons which consist of the pairing of either a c or b quark with an up or down light quark. Heavy flavor mesons will be treated separately in the following chapters with emphasis on the B meson and its decay. The light mesons and heavy charmed mesons are shown in Figure 1.2. The figure shows the mesons arranged in the badly broken $SU(4)_f$ flavor symmetry of the quark model. (Exact $SU(4)$ would give an unmixed 15-plet and a singlet, but the mass of the c quark breaks the flavor symmetry and allows the mixing between the $SU(3)_f$ triplet and the $SU(4)_f$ singlet.) A similar analysis of the symmetry in flavor $SU(3)_f$ gave physicists suggestive evidence of a deeper structure in elementary particles and led eventually to the creation of the modern quark model.

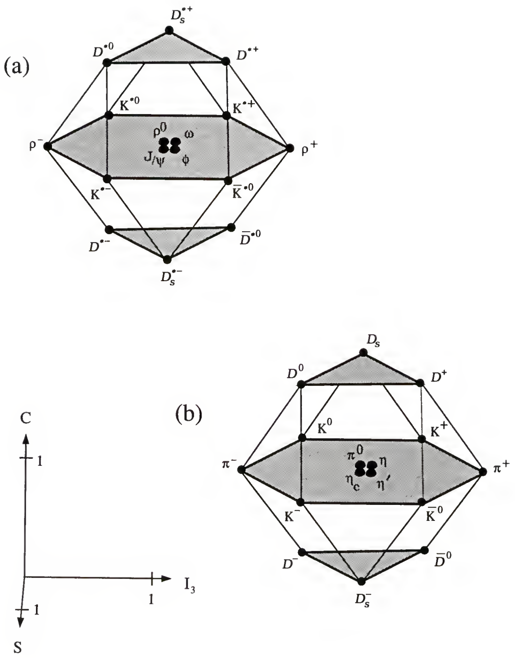

Figure 1.2 The $SU(4)_f$ flavor $q\bar{q}$ multiplets.

In (a) the 16-multiplet for the vector spin-one mesons in (b) the spin zero pseudoscalars. The middle level corresponds to the $SU(3)_f$ flavor octet. The figure is taken from Ref. [2].

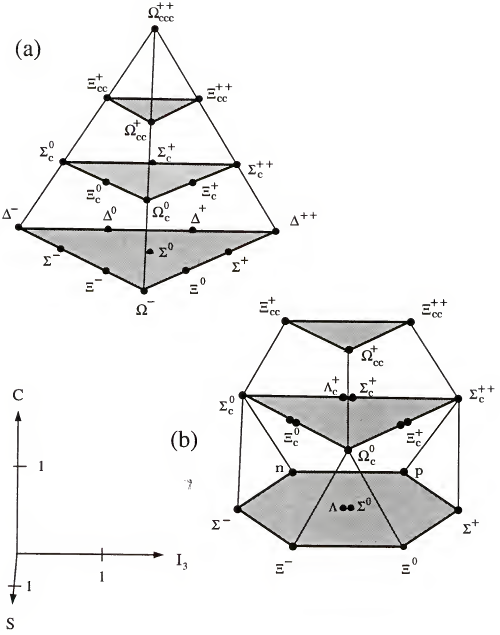

Figure 1.3 The $SU(4)_f$ flavor three quark multiplets.

In (a) the 20-multiplet for the spin-3/2. In (b) the spin 1/2 ground state baryons. The ground floors in (a) and (b) correspond to the $SU(3)_f$ flavor decuplet and octet respectively. In (b) the first floor shows two members in the $I_3 = \pm\frac{1}{2}$ position: the Ξ_c^0 and the Ξ_c^{++}. These correspond to the two possible states with the same third component of Vspin V_3 but different total V. The figure is taken from Ref. [2].

As described previously, the baryons are composed of color-singlet products of three quark triplets. Using the flavor $SU(4)_f$ symmetry we find that the 64 possible qqq combinations are decomposed into a fully symmetric (S) 20-plet with a $SU(3)$ decuplet, two other 20-plets with $SU(3)$ octets of mixed symmetry and a $SU(4)_f$ quadruplet. The $SU(3)$ octets of mixed symmetry are either symmetric (M_S) or anti-symmetric (M_A) under the interchange of the first two quarks. In Figure 1.3(a) the particles associated with the totally symmetric combination of the product of the symmetric $SU(4)_f$ 20-plet and symmetric spin $SU(2)$ multiplets give the ground state spin 3/2 baryons. To arrive at the spin 1/2 ground state baryons, Figure 1.3(b), we form totally symmetric combinations from the two 20-plets and two spin multiplets of mixed symmetry. The symmetric combination is necessary to form a totally anti-symmetric wavefunction states when including the completely antisymmetric color-singlet part into the total wavefunction. For the spin 3/2 baryons the total wavefunction $\psi = (20_S, 4_S, 1_A)$, expressed in terms of the spin, flavor and color multiplicities $SU(4)_f$, $SU(2)_s$, $SU(3)_C$ is

$$\psi = \frac{1}{\sqrt{2}}\left[(20_{M_S}, 4_{M_S}, 1_A) + (20_{M_A}, 4_{M_A}, 1_A)\right].$$

The flavor and spin decompositions are

$$SU(4)_f : 4 \otimes 4 \otimes 4 = 20_S \oplus 8_{M_S} \oplus 8_{M_A} \oplus \bar{4}_A$$
$$SU(2)_s : 2 \otimes 2 \otimes 2 = 4_S \oplus 2_{M_S} \oplus 2_{M_A}.$$

for color the decomposition is given in by Equation (1.1).

Because of the large mass of the c quark relative to the light quarks, flavor $SU(4)_f$ is not a useful symmetry. However, it provides a convenient framework for presenting all charmed mesons and baryons. In fact, the quarks are usually divided into the light quarks, the u, d and s, and heavy quarks, c, b and t. The approximate flavor symmetry of the light quarks is used extensively in chiral perturbation theory which attempts a quantitative description of low energy QCD phenomena. At the other end of the mass spectra the large masses of the c and b quarks are exploited in Heavy Quark Effective Theory (HQET) to achieve a model independent description of the behavior of hadrons containing heavy flavored quarks.

1.3 $SU(3) \times SU(2) \times U(1)$: The Standard Model

The description of the subatomic world given in the previous sections consisted mainly of a discussion of the composition of hadrons without much emphasis placed on the dynamics of the constituents. In the remainder of this chapter we focus our attention on a somewhat brief but general description of the fundamental interactions which influence the microscopic behavior of the fundamental fermions.

Of primary importance in describing the dynamics of the fully interacting particle theories is the principle of gauge or phase invariance. This principle asserts that the equations which govern fundamental particles do not change when an arbitrary phase is introduced. If the phase is a constant then by Noether's theorem a conserved quantity results. If the constant phase is associated with the charge of the fundamental particle then global gauge invariance implies the conservation of the charge. By generalizing the constant phase to a local or space-time dependent phase and imposing invariance under the gauge transformation the dynamics of the theory can, in principle, be derived. Theories which are gauge invariant, locally, are known as gauge theories and are believed to allow a description of all the microscopic behavior, that is the strong, weak and electromagnetic interactions between the fundamental fermions.

1.3.1 Quantum Electrodynamics

To best illustrate the generalization of the global gauge symmetry to a local one we will do so by first applying the procedure to the prototypical gauge theory of particle interactions: the theory of quantum electrodynamics (QED). In QED the dynamics of the theory can be completely derived by demanding invariance of the free particle Lagrangian under a local gauge transformation. We begin with the Lagrangian for a free fermion field

$$\mathcal{L}_0 = \bar{\psi}(x)(i\gamma^\mu\partial_\mu - m)\psi(x) \tag{1.2}$$

In a local gauge transformation the constant phase is generalized by making it a space-time dependent function

$$\psi \to \psi' = e^{i\alpha(x)}\psi. \tag{1.3}$$

This transformation no longer preserves the form of the original free particle Lagrangian since the derivative acts on the space-time dependent phase

$$\partial_\mu\psi \to e^{i\alpha(x)}\partial_\mu\psi + ie^{i\alpha(x)}\psi\partial_\mu\alpha \tag{1.4}$$

and produces a term proportional to $\partial_\mu\alpha$ which breaks the invariance of $\mathcal{L}_0$.

To restore covariance to the Lagrangian we replace the derivative with the covariant derivative

$$D_\mu \equiv \partial_\mu - ieA_\mu.$$

This covariant derivative transforms like $\psi(x)$ *i.e.*, $D_\mu\psi(x) \to e^{i\alpha(x)}D_\mu\psi(x)$. The transformation law of the covariant derivative determines the transformation property of the vector field which will introduce a term that exactly cancels the unwanted $\partial_\mu \alpha$ in Equation (1.4). The vector field thus transforms as

$$A_\mu \to A_\mu{}' = A_\mu + \frac{1}{e}\partial_\mu$$

and thus gives rise to an interaction term in the original free particle Lagrangian. This field has the form expected for the electromagnetic potential and is associated with the spin-one photon field.

The Classical QED Lagrangian can now be written down from the free particle Lagrangian with the replacement of the derivative with the covariant derivative. Since we want to associate the gauge field A_μ with a physical photon field, we need to add a covariant kinetic energy term for the vector field to the original Lagrangian

$$\frac{1}{4}F_{\mu\nu}F^{\mu\nu}$$

where

$$F_{\mu\nu} = \partial_\mu A_\nu - \partial_\mu A_\mu$$

arriving, finally, at the full QED Lagrangian

$$\mathcal{L}_{QED} = \bar{\psi}(i\partial\!\!\!/ - eA\!\!\!/)\psi - m\bar{\psi}\psi - \frac{1}{4}F_{\mu\nu}F^{\mu\nu}. \tag{1.5}$$

The tree level Feynman rules can be read directly off equation Equation (1.5). The coupling of fermion fields to the photon vector field is of strength e and is given by the $\bar{\psi}A\!\!\!/\psi$ term. We also note that the a mass term $(A_\mu A^\mu)$ for the vector field is absent from the Lagrangian which implies that the gauge field is massless. From the kinetic energy terms we find that the propagator for the vector field, after gauge fixing, is proportional to $1/q^2$ where q is the momentum transfer of the exchange photon. From the $\bar{\psi}\partial\!\!\!/\psi$ term the propagator for fermion fields is proportional to $1/(p\!\!\!/ - m)$.

In the quantization procedure, using the path integral formulation, the classical Lagrangian Equation (1.5) is used as an input to the effective Lagrangian written as an expansion in $\hbar$,

$$\mathcal{L}_{eff} = \mathcal{L}_{cl} + \hbar\mathcal{L}_1 + \hbar^2\mathcal{L}_2 + \cdots$$

The higher order terms generate loop corrections to the classical Lagrangian which introduce new interactions and or finite corrections to the basic interactions. Evaluating the loop contributions introduces divergences which can be effectively removed by renormalizing the input parameters and fields of the theory. The renormalization procedure results in the modification of the parameters which make them dependent on an arbitrary scale. The parameter can be evaluated at convenient scale and then extrapolated, through the use of the renormalization group equations, to the scale of interest. For example, the renormalization group equations give the running of the QED coupling constant to all orders in perturbation theory as

$$\alpha(q^2) = \frac{\alpha(\mu^2)}{1 - \frac{\alpha(\mu^2)}{3\pi}\log\left(\frac{q^2}{\mu^2}\right)} \ . \tag{1.6}$$

Here μ is the arbitrary scale and q is the mass scale of the interaction. A convenient point for QED calculation is usually taken at $q^2 = 2m_e^2$ where α^2 is the well known value of $1/137$.

1.3.2 Quantum Chromodynamics

While few similarities appear to exist between strong and electro-magnetic interactions the same gauge principle used to derive the dynamics of QED can, when applied to the $SU(3)$ color symmetry, be used to derive the dynamics of the strong interaction [3,4]. We begin as before with the free quark Lagrangian

$$\mathcal{L}_0 = \bar{q}(x)(i\partial\!\!\!/ - m)q(x) \tag{1.7}$$

in analogy with QED Equation (1.3) a gauge transformation takes the form of

$$q(x) \to U(x)q(x) = e^{i\alpha_a(x)\frac{\lambda^a}{2}}q(x)$$

where α_a is an space-time dependent phase, the λ^a are the Gell-Mann matrices that satisfy the $SU(3)$ commutation relations and normalization conditions

$$\left[\frac{\lambda_a}{2}, \frac{\lambda_b}{2}\right] = if^{abc}\frac{\lambda^c}{2} \quad ; \quad \mathrm{tr}\,(\lambda^a\lambda^b) = 2\ \delta^{ab}. \tag{1.8}$$

and the unitary transformation $U(x)$ is now an arbitrary 3×3 unitary matrix. Unlike the $U(1)$ case, the generators of $SU(3)$ do not commute. This has important consequences to the possible interactions of the theory since it implies that the gauge bosons themselves carry charge and can thus self interact. Gauge groups with non-commuting generators are know as non-Abelian gauge groups.

We now proceed as in QED and demand covariance by replacing the derivative ∂_μ with the covariant derivative

$$D_\mu = \partial_\mu - ig_s T_a G^a_\mu \quad ; \quad a = 1 \cdots 8,$$

where $T_a = \frac{\lambda_a}{2}$ and g_s is the strong coupling constant. The transformation of the vector field is augmented by an additional term to cancel the extra terms introduced by the gauge transformations of a non-Abelian group. The transformation of the gluon field is thus given by

$$G^a_\mu \to G^a_\mu - \frac{1}{g_s}\partial_\mu\alpha_a - f_{abc}\alpha_b G^c_\mu \tag{1.9}$$

To complete the QCD Lagrangian we need to add a kinetic energy term which is invariant under the transformation similar to Equation (1.9). The covariant kinetic energy term is

$$F^a_{\mu\nu} = \partial_\mu G^a_\nu - \partial_\nu G^a_\mu - g f_{abc} G^b_\mu G^c_\nu$$

Adding the kinetic energy term to the original Lagrangian, Equation (1.7), and replacing the derivative with the covariant derivative, we arrive at the classical QCD Lagrangian

$$\mathcal{L}_{QCD} = -\frac{1}{4} F^a_{\mu\nu} F^{\mu\nu}_a + \bar{q}(x) \left(i\gamma^\mu \partial_\mu + \frac{g_s}{2} \gamma^\mu G^a_\mu \lambda_a \right) q(x) - \bar{q}(x) m q(x) \quad (1.10)$$

where the quark fields are described by $q(x)$ and the gluons by the gauge fields G^a_μ.

Similarly to QED we can qualitatively derive the Feynman rules by inspection. Propagators for the quarks and gluons are obtained from the terms proportional to $\bar{q}q$ and A^2 respectively and quark gluon couplings of strength g are given by $g\bar{q}qA$ term. In addition, the non-Abelian fields in the kinetic energy term introduce additional interactions that involve gluons coupling to themselves. These terms, $g_s A^3$ and $g_s^2 A^4$, give rise to three and four gluon couplings of strength g_s and g_s^2 respectively and have no analog in QED.

The self-interactions of the gluons are a result of the non-Abelian character of the gauge group and imply that the gauge fields themselves carry the color charge. Observationally, this property of the theory manifests itself in the confinement of the quarks in hadronic final states. The theory also exhibits the property known as asymptotic freedom which states that at short distances the force between quarks goes to zero. This is illustrated in the running coupling constant

$$\alpha_s(q^2) = \frac{4\pi}{(11 - \frac{2}{3}n_f)\ln q^2/\Lambda^2_{QCD}} \tag{1.11}$$

where α_s is expressed as a function of the energy scale q and Λ_{QCD} is the scale at which the coupling constant becomes infinite. Asymptotic freedom follows since as $\alpha_s \to 0$, $q \to \infty$. In Equation (1.11), the group properties of $SU(3)_C$ are reflected in the value of the constant 11.

1.3.3 The Theory of Electroweak Interactions

The weak interaction is not only responsible for the transmutation of quarks and leptons species but also changes the charge of the quark or lepton undergo the transition. The fact that both flavor and charge undergoing a change during the same transition suggests that the weak and electromagnetic interactions are different aspects of a single theory. We now believe that the weak and electromagnetic forces are indeed unified and are described by a gauge theory commonly referred to as the standard model of the electroweak interactions [5].

The masses of the intermediate vector bosons mediating the weak interactions have been measured and are 80.2 GeV for the $W^{\pm}$ and 91.2 GeV for the Z^0 [2]. The masses, however, cannot be added to the Lagrangian in terms bilinear in the fields since this would break gauge invariance and thus render the theory unrenormalizable. In the Weinberg-Salam model the gauge bosons are initially massless. They acquire mass when the vacuum, which does not posses the original symmetry of the Lagrangian, is selected from among the many possible vacuum configurations. In this way masses for the vector bosons are generated in a gauge invariant way rendering the theory renormalizable [6]. In the electroweak theory three of the four massless vector bosons acquire mass while one remains massless. The details of how this is accomplished through the Higgs mechanism will be described in the following sections.

Unbroken electroweak theory. The electroweak theory is based on the non-Abelian gauge group formed by the product of a left-handed $SU(2)_L$ and $U(1)_Y$ for hypercharge or $SU(2)_L \times U(1)_Y$. The form of this gauge group is motivated by the need for an interaction which violates parity, is invariant under rotations in weak isospin $SU(2)_L$ and hypercharge $U(1)_Y$ space, and gives at least four gauge bosons: two massive charged vector bosons ($W^{\pm}$), a massive neutral boson (Z^0) and a massless vector boson (photon). The simplest group structure that can accommodate these conditions is the product of an $SU(2)_L \times U(1)_Y$. Before spontaneous symmetry breaking all gauge bosons are massless and the arguments that led to the derivation of the dynamics of QCD apply. The unbroken Lagrangian, in analogy with QCD is

$$\mathcal{L}_1 = -\frac{1}{4}(F^i_{\mu\nu}F^{i\mu\nu} + G_{\mu\nu}G^{\mu\nu}) \tag{1.12}$$

where

$$F^i_{\mu\nu} = \partial_\mu W^i_\nu - \partial_\nu W^i_\mu + g\epsilon^{ijk}W^j_\mu W^k_\nu, \qquad i = 1, 2, 3$$

and

$$G_{\mu\nu} = \partial_\mu B_\nu - \partial_\nu B_\mu$$

The potential energy term, also know as the Weyl Dirac term,† is given by

$$\mathcal{L}_2 = \bar{\psi}\left(i\gamma^\mu D_\mu\right)\psi$$

† At this point in the derivation, the Weyl Dirac part of the Lagrangian does not have a term bilinear in the fermion fields since this would break the $SU(2) \times U(1)$ symmetry. Fermion mass terms will be introduced in the Higgs sector and are also a product of spontaneous symmetry breaking.

Table 1.1

Table of fermion weak isospin and hypercharge assignments

Fermion	T	T_3	Y	Q
ν_e, ν_μ, ν_τ	$\frac{1}{2}$	$\frac{1}{2}$	-1	0
e_L, μ_L, τ_L	$\frac{1}{2}$	$-\frac{1}{2}$	-1	-1
u_L, c_L, t_L	$\frac{1}{2}$	$\frac{1}{2}$	$\frac{1}{3}$	$\frac{2}{3}$
d_L, s_L, b_L	$\frac{1}{2}$	$-\frac{1}{2}$	$\frac{1}{3}$	$-\frac{1}{3}$
e_R, μ_R, τ_R	0	0	-2	-1
u_R, c_R, t_R	0	0	$\frac{4}{3}$	$\frac{2}{3}$
d_R, s_R, b_R	0	0	$-\frac{2}{3}$	$-\frac{1}{3}$

Demand of local gauge invariance gives the form of the covariant derivative

$$\partial_\mu \to D_\mu = \partial_\mu - ig\mathbf{T} \cdot \mathbf{W}_\mu - ig'\frac{Y}{2}B_\mu.$$

Here $\mathbf{T} = T\boldsymbol{\tau}$ and the $\boldsymbol{\tau}$ are the Pauli matrices that satisfy the commutation relations

$$\left[\sigma_i, \sigma_j\right] = 2\epsilon_{ijk}\sigma_k \tag{1.13}$$

and generate the $SU(2)$ group. The $U(1)$ group is generated by the weak hypercharge $Y = 2(Q - T_3)$.

The quantum number assignment for all fermions is shown in Table 1.1. The group structure allows for any choice of hypercharge assignment but the particular values chosen allow for the cancelation of Adler-Bell-Jackiw (ABJ) anomalies . With the quantum number assignments above the covariant derivative acts on the left-handed lepton fields as

$$D_\mu \begin{pmatrix} \nu_e \\ e \end{pmatrix}_L = \left(\partial_\mu - ig\frac{\boldsymbol{\tau}}{2} \cdot \mathbf{W}_\mu + ig'\frac{1}{2}B_\mu\right) \begin{pmatrix} \nu_e \\ e \end{pmatrix}_L$$

and right-handed singlet as

$$D_\mu e_R = \left(\partial_\mu + ig' B_\mu\right) e_R.$$

Spontaneous symmetry breaking. To generate masses for three of the gauge bosons while preserving the masslessness of the boson associated with the electromagnetic interactions, the $SU(2)_L \times U(1)_Y$ symmetry must broken while preserving the $U(1)$ symmetry of QED. To begin we introduce, to the original Lagrangian, an additional $SU(2)_L \times U(1)_Y$ invariant term such as as

$$\mathcal{L}_3 = (D_\mu \Phi)^\dagger (D^\mu \Phi) - V(\Phi). \tag{1.14}$$

This term is known as the Higgs term or Higgs sector. The Higgs field Φ is a complex two-component scalar field

$$\Phi = \begin{pmatrix} \phi^+ \\ \phi^0 \end{pmatrix}, \qquad Y(\Phi) = 1 \tag{1.15}$$

which transforms as weak iso-doublet. To allow for the required spontaneous breakdown of the electroweak symmetry, we let the potential (the Higgs potential) take the form of

$$V(\Phi) = -\mu^2 \Phi^\dagger \Phi + \lambda (\Phi^\dagger \Phi)^2. \tag{1.16}$$

The potential describes the interaction of four scalar particles (two complex components for each member of the doublet) interacting with the four gauge bosons $\mathbf{W}$ and the B. For positive μ^2 and λ the minimum of the potential gives the vacuum expectation value (VEV).

$$\Phi^\dagger \Phi = -\frac{\mu^2}{2\lambda}$$

We now want to expand about the minima of the potential and we do so by picking a particular configuration of the physical vacuum from among the many possibilities. The particular vacuum configuration is not chosen arbitrarily, instead a configuration is picked such that the original $SU(2) \times U(1)$ symmetry is broken down to the $U(1)_{em}$ of QED. The choice made, expanded about the minima, is

$$\langle \Phi \rangle_0 = \begin{pmatrix} 0 \\ \frac{v+\eta(x)}{\sqrt{2}} \end{pmatrix}, \qquad \text{with} \quad v = (\mu^2/\lambda)^{\frac{1}{2}}.$$

Since Φ_0 has $T = \frac{1}{2}$ and $T^3 = -\frac{1}{2}$, the generators for both the $SU(2)$ and $U(1)$ are broken. But since Φ_0 is neutral the generator of QED

$$Q = T^3 + \frac{Y}{2}$$

remains unbroken and thus the vacuum is invariant under the $U(1)_{em}$. This then implies that the gauge boson associated with this symmetry remains massless and we get the massless gauge boson sought.

The Higgs mechanism. To see the explicit mass generation through the Higgs mechanism, we introduce four new fields $\boldsymbol{\xi}(\boldsymbol{x})$ and $h(x)$ and express the electroweak vacuum in terms of the new fields

$$\Phi = e^{-i\boldsymbol{\xi}(x)\cdot\boldsymbol{\tau}/v} \begin{pmatrix} 0 \\ \frac{v+h(x)}{\sqrt{2}} \end{pmatrix}.$$

This particular form allow us to gauge away the three massless Nambu-Goldstone bosons arising from the spontaneously broken continuous symmetry (the Goldstone theorem). In gauging away the extra degrees of freedom the massless bosons acquire mass terms when the fields are transformed by a unitary transformation of the form

$$U(\xi) = e^{i\boldsymbol{\xi}(x)\cdot\boldsymbol{\tau}/v}. \tag{1.17}$$

The new transformed fields are defined by

$$\Phi' = U(\xi)\Phi = \frac{v + h(x)}{\sqrt{2}}\chi, \quad \text{where} \quad \chi = \begin{pmatrix} 0 \\ 1 \end{pmatrix} \tag{1.18}$$

and

$$\begin{aligned} f'_L &= U(\xi) f_L, \quad f'_R = f_R \\ \frac{\boldsymbol{\tau}\cdot\mathbf{W}'}{2} &= U(\xi)\left(\frac{\boldsymbol{\tau}\cdot\mathbf{W}}{2}\right)U^{-1}(\xi) - \frac{i}{g}[\partial_\mu U(\xi)]U^{-1}(\xi) \\ B'_\mu &= B_\mu. \end{aligned} \tag{1.19}$$

This procedure is known as the Higgs mechanism. The three degrees of freedom associated with the massless Goldstone bosons are transformed into the longitudinal polarization associated with the now massive vector boson of the broken theory.

We now show the emergence of the mass terms in the Higgs sector of the Lagrangian by expressing Equation (1.14) in terms of the new fields

$$\mathcal{L}_3 = (D_\mu\Phi')^\dagger(D^\mu\Phi') - V(\Phi'). \tag{1.20}$$

The kinetic energy term

$$\begin{aligned} (D_\mu\Phi')^\dagger(D^\mu\Phi') &= \Phi^\dagger\left(\partial_\mu + g\frac{\boldsymbol{\tau}}{2}\cdot\mathbf{W}'_\mu + \frac{g'}{2}B'_\mu\right)\left(\partial_\mu + g\frac{\boldsymbol{\tau}}{2}\cdot\mathbf{W}'_\mu + \frac{g'}{2}B'_\mu\right)\Phi \\ &= \frac{1}{2}\partial_\mu h(x)\partial^\mu h(x) + \frac{1}{8}\Big[g^2(W'^1_\mu - iW'^2_\mu)(W'^1_\mu + iW'^2_\mu) \\ &\qquad + (gW'^3_\mu - g'B'_\mu)^2\Big](v + h(x))^2 \end{aligned} \tag{1.21}$$

contains the anticipated mass terms for the gauge vector fields. This can be shown if we redefine W'^1 and W'^2 as

$$W^\pm_\mu = \frac{1}{\sqrt{2}}(W'^1_\mu \pm iW'^2_\mu) \tag{1.22}$$

and introduce two new fields Z_μ and A_μ defined to be a linear combinations of the W'^3_μ and B'_μ gauge fields. These are associated with the neutral intermediate vector boson and the electromagnetic vector potential by the relations

$$Z_\mu = \cos\theta_W W'^3_\mu - \sin\theta_W B'_\mu$$
$$A_\mu = \cos\theta_W W'^3_\mu + \sin\theta_W B'_\mu$$

where

$$\cos\theta_W \equiv \frac{g}{\sqrt{g^2+g'^2}}. \tag{1.23}$$

plugging all of this into the kinetic energy terms in Equation (1.21) gives

$$\begin{aligned}\frac{1}{2}\partial_\mu h(x)\partial^\mu h(x) &+ \frac{1}{2}m_Z^2 Z^\mu Z_\mu + m_W^2 W^+_\mu W^{\mu-} \\ &+ \frac{h(x)}{v}(2+\frac{h(x)}{v})\left(\frac{1}{2}m_Z^2 Z^\mu Z_\mu + m_W^2 W^+_\mu W^{\mu-}\right),\end{aligned} \tag{1.24}$$

The masses of the intermediate vector bosons are given by

$$\begin{aligned} m_Z^2 &= \frac{1}{4}v^2(g^2+g'^2) \\ m_W^2 &= \frac{1}{4}v^2 g^2. \end{aligned} \tag{1.25}$$

The kinetic energy term for the Higgs scalar $h(x)$ and couplings to the vector bosons also originate in Equation (1.24). Finally the mass of the Higgs field

$$m_h = v\sqrt{s\lambda} = \mu\sqrt{2}$$

can be read off the quadratic term of the Higgs potential.

With the addition of the Higgs field, couplings to the fermions need to be included in the Lagrangian. The most general $SU(2)\times U(1)$ Yukawa couplings between scalars and fermions is given by

$$\mathcal{L}_4 = \mathbf{Y}^{(l)}\bar{L}^i_L e^j_R \Phi + \mathbf{Y}^{(u)}\bar{Q}^i_L u^j_R \tilde{\Phi} + \mathbf{Y}^{(d)}\bar{Q}^i_L d^j_R \Phi \tag{1.26}$$

where the L_L, Q_L and (e_R, u_R, d_R) are the left-handed (right-handed) lepton, quark doublets (singlets), $ij = 1,2,3$ are the family indices and $\mathbf{Y} \equiv y^{ij}$ are the

Yukawa matrices. The states so far discussed are gauge eigenstates and thus the Yukawa mass matrices y_{ii} are in general not necessarily diagonal. Since any matrix can be expressed as the product of two unitary matrices times a real diagonal matrix (biunitary transformation), we can express the Yukawa mass matrices as Equation (1.26) as

$$\begin{aligned}\mathbf{Y}^{(l)} &= \mathbf{S}_l^T \mathbf{M}_{\mathrm{d}}{}^{(l)} \mathbf{R}_l,\\ \mathbf{Y}^{(d)} &= \mathbf{S}_d^T \mathbf{M}_{\mathrm{d}}{}^{(d)} \mathbf{R}_d,\\ \mathbf{Y}^{(u)} &= \mathbf{S}_u^T \mathbf{M}_{\mathrm{d}}{}^{(u)} \mathbf{R}_u\end{aligned}$$

In the lepton sector the biunitary transformations can be absorbed in the definition of the fields by redefining them as

$$L'_L \to \mathbf{S}_l L_L, \qquad e'_R \to \mathbf{R}_l e_R. \tag{1.27}$$

In the quark sector the right-hand quark fields can be similarly redefined; however, the left-handed quark doublets couple to both up and down types of right-handed quarks thus redefining say

$$Q'_L \to \mathbf{S}_d Q_L, \tag{1.28}$$

will introduce a $\mathbf{S}^\dagger$ in the right-handed up type coupling term. The usual procedure is to redefine the left-handed fields as in Equation (1.28) and introduce a matrix to fix up the right-hand quark coupling. The matrix $\mathbf{V} = \mathbf{S}_u \mathbf{S}_d^\dagger$ is known as the Cabibbo-Kobayashi-Maskawa (CKM) quark mixing matrix

$$\mathbf{V} = \begin{pmatrix} V_{ud} & V_{us} & V_{ub} \\ V_{cd} & V_{cs} & V_{cb} \\ V_{td} & V_{ts} & V_{tb} \end{pmatrix} \tag{1.29}$$

and arises when the Yukawa matrices are diagonalized. The matrix has four independent parameters and can be described by three mixing angles and a complex phase. A non-zero value for the phase is the source of CP-violation in the Standard Model.

After diagonalizing the mass matrix, the form of the Yukawa coupling is

$$\mathcal{L}_4 = \mathrm{M}_{\mathrm{d}}^{(l)} \bar{L}_L e_R \Phi + \mathrm{M}_{\mathrm{d}}^{(u)} \bar{Q}_L \left(\mathbf{V}^T\right) u_R \tilde{\Phi} + \mathrm{M}_{\mathrm{d}}^{(d)} \bar{Q}_L d_R \Phi. \tag{1.30}$$

Expanding Equation (1.30) in the unitary gauge we see that the VEV of the Higgs doublet gives masses to fermions in a universal way,

$$\begin{aligned}
\mathcal{L}_4^{(l)} &= \left(1 + \frac{h(x)}{v}\right) \left[m_e \bar{e} e + m_\mu \bar{\mu} \mu + m_\tau \bar{\tau} \tau\right] \\
\mathcal{L}_4^{(d)} &= \left(1 + \frac{h(x)}{v}\right) \left[m_d \bar{d} d + m_s \bar{s} s + m_b \bar{b} b\right] \\
\mathcal{L}_4^{(u)} &= \left(1 + \frac{h(x)}{v}\right) \left[m_u \bar{u} u + m_c \bar{c} c + m_t \bar{t} t\right]
\end{aligned} \tag{1.31}$$

with the identifications

$$\begin{aligned}
\frac{v}{\sqrt{2}} y^{ii}(l) &= (m_e, m_\mu, m_\tau) \\
\frac{v}{\sqrt{2}} y^{ii}(d) &= (m_d, m_s, m_b) \\
\frac{v}{\sqrt{2}} y^{ii}(u) &= (m_u, m_c, m_t)
\end{aligned} \tag{1.32}$$

The tree level Feynman rules can be read off the Classical Lagrangian expressed as the sum of $\mathcal{L}_1$ through $\mathcal{L}_4$. The Higgs sector, however, increases the number of couplings and thus the total number of diagrams allowed. In particular, the newly introduced Higgs scalar couples not only to the vector bosons but to all the fermions as well. Also, additional couplings of the various vector bosons to each other make for somewhat more topologically complicated Feynman diagrams.

CHAPTER 2
THE PHYSICS OF THE b QUARK

Introduction

Experimental b physics began in 1977 with the discovery of a narrow resonance at 9.5 GeV in $p + N \rightarrow \mu^+\mu^- + X$ events at Fermilab's CFS [7] experiment. Shortly thereafter, the observation was confirmed by e^+e^- experiments including the CLEO [8] and CUSB [9] collaboration at CESR. These experiments also measured the hadronic cross-section in the region around $\sqrt{s} \simeq 10$ GeV and found a series of narrow resonance consistent with radial excitations of the $b\bar{b}$ quarkonium state. The states formed in e^+e^- annihilation share the quantum numbers of the parent virtual photon and are thus produced in a $J = 1, S = 0$ state. These states are known collectively as the Υ resonances. This discovery was followed shortly by the discovery of hadrons containing the new b quark paired with a light quark [10,11]. These states are known as the B mesons and measurement of their decay rates is the primary aim of this analysis.

In this chapter we sketch the theoretical framework which describes the decay mechanism of the B mesons. We will begin by briefly describing some of the more important points in the physics of the upsilon system since all B meson used in this analysis are decay products of the $\Upsilon(4S)$.

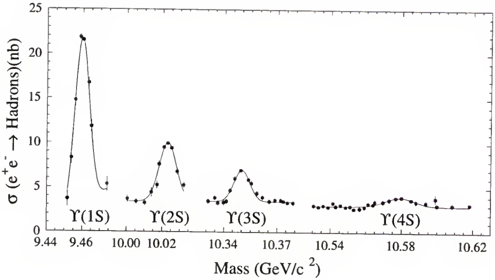

Figure 2.1 Hadronic cross-section of e^+e^- annihilation.

2.1 The Υ Resonances

In Figure 2.1 the hadronic cross-section is plotted as a function of the e^+e^- center of mass energy. The plot shows the first four Υ resonances. The first three states, $\Upsilon(1S) - \Upsilon(3S)$, show the characteristic narrow widths expected for quarkonium states with masses below open flavor threshold. In fact, the widths here are dominated by the beam-energy resolution rather than by the intrinsic widths of the states themselves. The widths and masses of the states are given in Table 2.1.

We can understand the small widths if we consider all possible decay diagrams accessible to states with masses below $B\bar{B}$ threshold. The possible diagrams are shown in Figure 2.2. In (a) and (b) the decay rate, and thus the overall width, is reduced, relative to open bottom production, by higher order

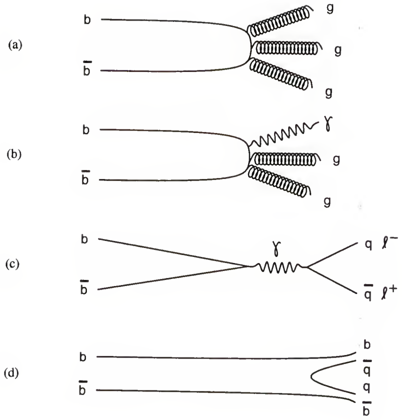

Figure 2.2 Diagrams which contribute to Υ decays.

In (a) the purely hadronic channel available to resonances with masses below open quark production. In (b) the radiative hadronic channel. In (c) the $q\bar{q}$ annihilation diagram. In (d) the open production of $B\bar{B}$.

couplings such as $(\alpha_s)^3$ and $(\alpha_s)^2(\alpha)$ respectively. Hadronic channels where a single gluon is exchanged are forbidden due to color conservation which disallows the production of color-singlet states from single colored gluons. Also, two gluon exchange C even processes are excluded since C is a conserved quantum number in strong interactions. In quark annihilation diagrams (Figure 2.2 (c)), decay rates are suppressed by factors of f_V^2 and order α^2 couplings.

Table 2.1

Upsilon States

Resonance	Mass (GeV)	$\Gamma_{e^+e^-}$ (keV)	Γ_{Total} (keV)
$\Upsilon(1S)$	9.46037 ± 0.00021	1.32 ± 0.03	52.5 ± 1.8
$\Upsilon(2S)$	10.02330 ± 0.00031	0.554 ± 0.030	44 ± 7
$\Upsilon(2S)$	10.3553 ± 0.0005	0.45 ± 0.04	26.3 ± 3.5
$\Upsilon(4S)$	10.5800 ± 0.0035	0.24 ± 0.05	$(23.8 \pm 1.8) \times 10^3$
$\Upsilon(5S)$	10.865 ± 0.008	0.31 ± 0.07	$(110 \pm 13) \times 10^3$
$\Upsilon(11020)$	11.019 ± 0.008	0.13 ± 0.030	$(79 \pm 16) \times 10^3$

2.1.1 Spectroscopy of the Υ System

The Υ resonances also decay into a rich spectrum of states through strong and electromagnetic processes. The spectroscopy of heavy flavor quarkonia can be described in close analogy with that of electromagnetically bound positronium. Because of the large mass of the b quark, the Υ system can in principle by described by nonrelativistic QCD potential models [12,13]. Recently, the symmetries of heavy quark effective theory (HQET) have been applied to bottom and charmonium systems [14].

Several spectroscopic transitions between the various $\Upsilon(nS)$ states have been observed. These include single photon transitions to the ^3P_J states known as χ_b, hadronic transitions to χ_b and hadronic transitions to lower lying radial excitations. The spectroscopy of the Υ system is shown in Figure 2.3.

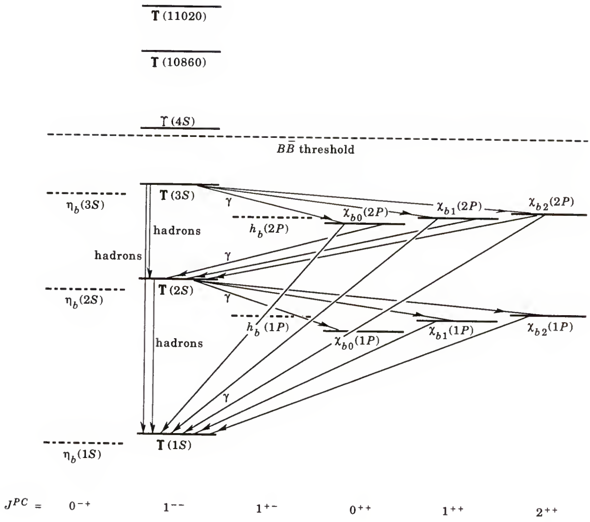

Figure 2.3 The spectrum of bottomonium.

2.1.2 The Decay of $\Upsilon(4S)$ Resonance

The first Υ resonance massive enough to allow for the production of $B\bar{B}$ mesons is the $\Upsilon(4S)$. The large width and the dramatic increase in the production of leptons gave the first direct evidence for open bottom meson production [11]. The lepton spectrum observed was consistent with production in decays of heavy quark through the $\bar{B} \to Xl\nu$ channel [10]. Eventually the B meson was reconstructed in exclusive channels and its mass was measured to be 5.2786 ± 0.0008 GeV [10].

The $\Upsilon(4S)$ is only 20 MeV above $B\bar{B}$ threshold. Due to phase-space limitations it can only decay to bottom mesons with either a u or d quark. Also, the first excited state, the B^*, is 46 MeV above the ground state; excluding the possibility of $B\bar{B}$ decays other than to those which are back to back decays. The small amount of energy above threshold also implies that the B mesons are produced nearly at rest. The average momentum of each B is approximately 330 MeV, a fact which will be exploited when reconstructing the exclusive decays of the B.

To calculate the branching fractions of B mesons we need to know the number of B mesons produced. The ratio of charged to neutral $B\bar{B}$ production (f_{+-}/f_{00}) and the fraction of $B\bar{B}$ pairs produced ($f_{B\bar{B}}$) in the decay of the $\Upsilon(4S)$ are thus important quantities to consider. Recently, the CLEO collaboration has determined the production ratio to be [15]

$$\frac{f_+}{f_0} = \frac{\Upsilon(4S) \to B^+B^-}{\Upsilon(4S) \to B^0\bar{B}^0} = 1.04 \pm 0.13 \pm 0.16 \; . \tag{2.1}$$

The systematic error includes uncertainties in the ratio of B^0 to B^+ lifetimes. The result is consistent with equal production of B^+B^- and $B^0\bar{B}^0$ pairs. In this analysis we assume that $f_{00} = f_{+-} = \frac{1}{2}$. Also, CLEO II has recently set an upper-limit on the number of non-$B\bar{B}$ decays of the $\Upsilon(4S)$ by comparing dilepton and single lepton yields. The value obtained is less than 0.05 at the 95% confidence level and is thus consistent with $f_{B\bar{B}} = 1$ [16].

2.2 The Decay of the B Meson

Weak decays of B mesons have been the subjects of great theoretical and experimental interest since their discovery in the early 1980s. The large mass of the b quark and the large momentum transfer involved in its decay provides an excellent laboratory to probe both the weak and strong interactions. Theoretical models which describe the decay processes of hadrons can be better tested at the large energy scales typical of b quark decays.

There are significant theoretical simplifications that arise in the study of QCD by considering mesons with large masses. In particular, the large mass of the heavy quark, when compared to Λ_{QCD}, implies that its actual value becomes irrelevant to the dynamics of the light degrees of freedom in the composite hadron. The heavy quark can thus be thought of as a static source of color which interacts with the remaining light quarks and gluons. In the infinite mass limit the particular flavor of the quark and its spin also become irrelevant in the dynamical behavior of the hadron and give rise to $SU(2N)$ spin-flavor symmetries. These ideas form the general framework upon which the Heavy Quark Effective Theory (HQET) is based [17]. In HQET the spin-flavor symmetry is exploited to build an effective Lagrangian density. The Lagrangian is then used to derive an effective theory analogous to QCD, complete with its own set of Feynman rules, in which the perturbative expansion is also now an expansion in $\Lambda_{\mathrm{QCD}}/m_Q$. These ideas have generated many new theoretical

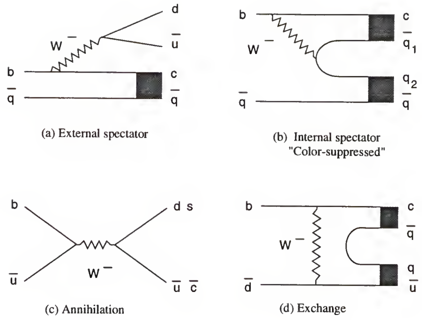

Figure 2.4 Possible B meson weak decay diagrams.

developments in the past decade which have led to a better understanding of the processes that govern the decays of heavy quarks.

The remainder of this chapter is devoted to the phenomenological description of the weak decay of heavy flavor mesons. While all of these ideas apply to charmed mesons as well, we will concentrate only on the decays of the B meson. Also, this analysis deals with the exclusive reconstruction of two-body B meson decays. The scope will thus be limited to the discussion of exclusive non-leptonic decays.

To begin the description of the decays of the B mesons, we first consider all the possible weak decay diagrams which can mediate the process. In Figure 2.4 all possible lowest order weak diagrams which contribute to the two-body decay of the B meson are shown. In (a), the external spectator, the quarks produced at the W vertex hadronize together into one of the two final states. This forms the simplest of the four decays diagrams to treat theoretically since it involves no $q\bar{q}$ popping and the final states consist of matched quark colors fields. In (b) the internal spectator or "color-suppressed" diagram things are a bit more complicated. Now the original light spectator quark hadronizes with one of the quarks produced at the W vertex. Hard gluon exchanges can no longer be ignored and must now be included in the theoretical description. There is also a requirement that the color degrees of freedom match within each composite hadron. This requirement would naively predict that processes which can proceed only through internal diagrams are suppressed relative to ones which proceed only through external diagrams. Since there are three colors to include, the naive expectation gives a suppression factor of $(1/N_c)^2 = 1/9$. We will see later that this situation is somewhat more complicated when hard gluons corrections are included. The suppression hence becomes somewhat larger than the naive expectation.

The other diagrams in Figure 2.4 are usually ignored since their contribution to the decay modes considered are small when compared to simple spectator processes [18]. For example, the contribution from the exchange diagram (d) is both helicity and color suppressed relative to the external spectator (a). The overall decay rate is reduced by a factor $\frac{f_B^2}{m_b^4}(m_c^2 + m_u^2)\frac{1}{9}$, where f_B is the B meson decay constant, m_u is the mass of the light quarks (a u or a d) and m_b is the mass of the b quark. The expected suppression is $\sim 10^{-5}$ and thus the usual procedure of ignoring this channel is well justified. The quark combinations possible in (d) do not provide a channel for the decay modes considered in this analysis.

The particular decay modes of the B meson considered for this analysis fall into three general categories:

$$\begin{array}{ll} B_d^0 \to M^+ m^- & \text{Class I decays} \\ B_d^0 \to M^0 m^0 & \text{Class II decays} \\ B_u^- \to M^0 m^- & \text{Class III decays} \end{array} \tag{2.2}$$

The M^+ or M^0 represent a charmed pseudoscalar or vector meson and the m represents a "light" pseudoscalar, vector or axial-vector state. The light mesons are all part of the family of isospin singlet or triplet states. The relevant daughters are:

$$\begin{array}{ll} M^+ = D^+, D^{*+} \quad \text{and} & M^0 = D^0, D^{*0} \\ m^- = \pi^-, \rho^-, a_1^- \quad \text{and} & m^0 = \pi^0, \eta, \eta', \rho^0, \omega \end{array} \tag{2.3}$$

We will see later that the three categories essentially separate the decays into modes which can proceed through either the external (class I) spectator, the internal spectator (class II) or through a combination of both weak decay diagrams (class III).

2.2.1 The Weak Hamiltonian

The starting point in the description of the phenomenology of non-leptonic decays of heavy-flavored mesons is the Lagrangian density. The bare current-current form of the Lagrangian density for a CKM allowed $b \to c$ transition is given by the coupling of the weak currents to the $W^\pm$ operators. The charged current-current Lagrangian is

$$\mathcal{L}cc = \frac{g}{2\sqrt{2}} \left(W_\mu^+ J_-^\mu + W_\mu^- J_+^\mu \right)$$

where the current

$$J_-^\mu = \left(J_+^\mu\right)^t = (\bar{u} \quad \bar{c} \quad \bar{t})\,\gamma^\mu(1-\gamma_5)V_{CKM}\begin{pmatrix} d \\ s \\ b \end{pmatrix}$$

are the left-handed currents in the $SU(2) \times U(1)$ standard model. The symbol V_{CKM} denotes the Cabibbo-Kobayashi-Maskawa mixing matrix of Equation (1.29) and relates the weak eigenstates to mass eigenstates. The values of the individual entries are not predicted in the Standard Model but must be determined by experiment [2].

From the Lagrangian density we can read off the effective weak Hamiltonian; which to lowest order in the weak coupling constant is

$$H_w = \left(\frac{ig}{2\sqrt{2}}\right)^2 V_{cb}V_{ud}\{\bar{c}(p')\gamma^\mu(1-\gamma_5)b(p)\frac{-ig^{\mu\nu}}{k^2 - M_W^2}\bar{d}(q')\gamma_\nu(1-\gamma_5)u(q)\}. \tag{2.4}$$

This expression corresponds to the quark level spectator diagrams in Figure 2.4 where a b quark decays to a c quark and the virtual W creates a $u\bar{d}$ pair. For $m_W \gg k$, the denominator in the gauge propagator reduces to a constant and the mass of the gauge boson is absorbed into the dimension-full coupling constant G_F,

$$H_w = \frac{G_F}{\sqrt{2}}V_{cb}V_{ud}\{\bar{c}(p')\gamma^\mu(1-\gamma_5)b(p)\bar{d}(q')\gamma_\mu(1-\gamma_5)u(q)\}. \tag{2.5}$$

This limit, which corresponds to a zero range interaction, is justified for the class of decays considered here since the energy scale k of the reaction is much smaller than m_W, the mass of the vector boson.

2.2.2 QCD Corrections to the Effective Hamiltonian

The form of the effective Hamiltonian, Equation (2.5), is significantly modified by QCD corrections. To lowest order in α_s the effects are included by

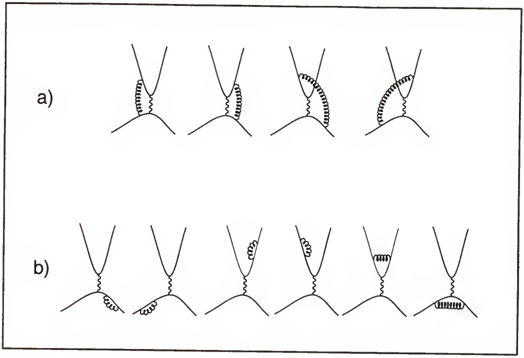

Figure 2.5 QCD corrected simple spectator decay diagram.

adding all topologically distinct weak decay diagrams which include the exchange of a single gluon. At this point in the derivation an assumption is made about long distance QCD effects. The assumption is simply that soft gluon exchange do not significantly affect the decay of the heavy mesons and are thus ignored in the calculation. Also, the energy scale is assumed to be sufficiently large such that higher order corrections give negligible contributions.

The possible Feynman diagrams which contribute to first order in α_s are shown in Figure 2.5. The diagrams are separated into (a) those that induce new effective 4-Fermi interactions with different color structure and (b) those that contribute to the renormalization of the weak couplings, quark masses and wavefunctions. In addition there are penguin type contributions which are of

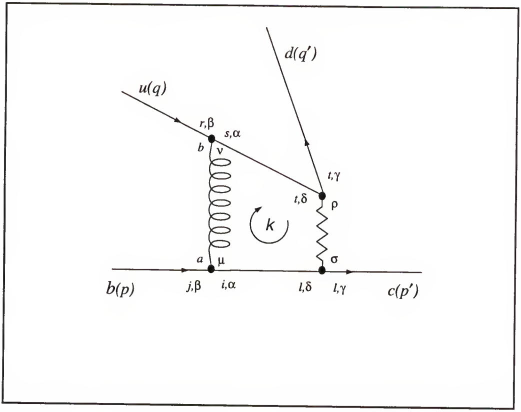

Figure 2.6 Hard gluon corrected simple spectator diagram.

the same order in α_s but lead to small contributions and are typically ignored for the decays considered here [18].

To see the origin of the new effective 4-Fermi interactions we first write down the effective Hamiltonian with explicit color indices. The Lorentz indices are suppressed in the expression and summation of the repeated indices is implied. The effective Hamiltonian is

$$H^a_{eff} = \left(\frac{ig_s}{2}\right)^2 \left(\frac{ig}{2\sqrt{2}}\right)^2 V_{cb}V^*_{ud} \int \frac{d^4k}{(2\pi)^4} \left[\frac{-ig_{\sigma\rho}}{(k-p')^2 - M_W^2}\right] \left[\frac{-i\delta_{ab}}{k^2} g_{\mu\nu}\right]$$
$$\times \left\{\bar{c}_l(p')\gamma^\sigma(1-\gamma_5)\left[\frac{i\delta^{li}}{(\not{k}-m_b)}\right]\frac{\lambda^a_{ij}}{2}\gamma^\mu b_j(p)\right\}$$
$$\times \left\{\bar{d}_t(q')\gamma^\rho(1-\gamma_5)\left[\frac{i\delta^{ts}}{(\not{k}-m_u)}\right]\frac{\lambda^b_{sr}}{2}\gamma^\nu u_r(q)\right\}. \tag{2.4}$$

It corresponds to the first of the four diagrams in figure 2.5(a) which has been recreated with explicit Lorentz and color indices in Figure 2.6.

To evaluate the integral in Equation (2.4) we first simplify the expression by setting the quark masses and external momenta to zero and collapse the W propagator to a point. The integral can now be evaluated from M_W down to an arbitrary cutoff scale μ [19]. We then sum the four diagrams in 2.5(a) and simplify the result by doing a bit of gamma matrix algebra [20]

$$H_{eff} = \frac{G_F}{\sqrt{2}}\frac{3}{8}\frac{\alpha_s}{\pi}\log\left(\frac{M_W^2}{\mu^2}\right) V_{cb}V^*_{ud}\left\{\bar{c}_i\gamma^\sigma(1-\gamma_5)\lambda^a_{ij}b_j \cdot \bar{d}_s\gamma_\sigma(1-\gamma_5)\lambda^a_{sr}u_r\right\}. \tag{2.5}$$

The derivation above shows how hard gluons, exchanged between the two quark currents, introduced a λ^a matrix to each current in the current-current operator. To show explicitly the generation of the new effective-neutral term we perform a Fierz transformation on Equation (2.5) by using the identity

$$(\lambda_a)_{ij}\,(\lambda_a)_{sr} = -\frac{2}{3}\,\delta_{ij}\delta_{sr} + 2\delta_{ir}\delta_{js}. \tag{2.6}$$

We now have Equation (2.5) in terms of effective charged and neutral current terms

$$H_{eff} = \frac{G_F}{\sqrt{2}}\frac{3}{8}\frac{\alpha_s}{\pi}\log\left(\frac{M_W^2}{\mu^2}\right) V_{cb}V^*_{ud}\Big\{ -\frac{2}{3}\,\bar{c}_i\gamma^\sigma(1-\gamma_5)b^i \cdot \bar{d}_s\gamma_\sigma(1-\gamma_5)u^s$$
$$+ 2\,\bar{c}_i\gamma^\sigma(1-\gamma_5)u^i \cdot \bar{d}_j\gamma_\sigma(1-\gamma_5)b^j\Big\}. \tag{2.7}$$

If we collect terms with definite flavor symmetries we can rewrite Equation (2.7) in terms of operators which belong to different flavor representations and thus do not mix under renormalization. The new operators ($O_\pm$) are given by

$$O_\pm = \frac{1}{2}\left[\bar{c}\gamma^\sigma(1-\gamma_5)b\cdot\bar{d}\gamma_\sigma(1-\gamma_5)u \pm \bar{c}\gamma^\sigma(1-\gamma_5)u\cdot\bar{d}\gamma_\sigma(1-\gamma_5)b\right] \quad (2.8)$$

Expressed in terms of $O_\pm$, H_{eff} now reads

$$H_{eff} = \frac{G_F}{\sqrt{2}}V_{cb}V_{ud}\left\{C_+(\mu)O_+ + C_-(\mu)O_-\right\}. \quad (2.9)$$

The scale dependent coefficients $C_\pm(\mu)$ provide a convenient place to store the effects from renormalization and hard gluon corrections. Before the renormalization procedure the coefficients $C_\pm$ are given by

$$\begin{aligned} C_+(\mu) &= 1 - \frac{\alpha_s}{2\pi}\log\left(\frac{M_W^2}{\mu^2}\right) \\ C_-(\mu) &= 1 + \frac{\alpha_s}{\pi}\log\left(\frac{M_W^2}{\mu^2}\right). \end{aligned} \quad (2.10)$$

Use of the renormalization group equations gives, in the leading logarithmic approximation (LLA) at the b quark scale [21],

$$C_\pm(\mu) = \left(\frac{\alpha_s\left(\mu^2\right)}{\alpha_s\left(m_W^2\right)}\right)^{\frac{2\gamma_\pm}{b}} \quad \text{with} \quad \alpha_s\left(\mu^2\right) = \frac{4\pi}{b\log(\mu^2/\Lambda_{QCD}^2)} \quad (2.11)$$

where $\gamma_- = -2\gamma_+$, $b = 11 - \frac{2}{3}n_f$ and $n_f = 4$ for b decays. With $\mu = m_b \simeq$ 5 GeV and $\Lambda_{QCD} = 0.250$ GeV we find

$$\begin{aligned} C_+ &= 0.85 \qquad C_- = 1.39 \quad \text{(LLA)} \\ C_+ &= 0.82 \qquad C_- = 1.49 \quad \text{(NLLA)} \end{aligned}. \quad (2.12)$$

The next-to-leading log (NLLA) corrections modify the (LLA) results only slightly [18] indicating that at the b scale the perturbative expansion gives reliable results.

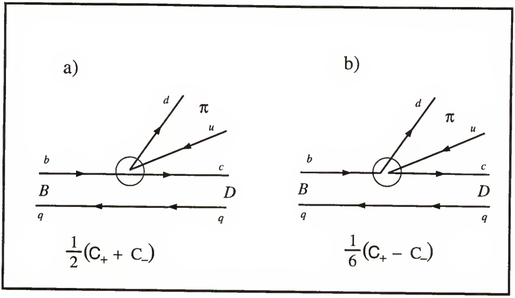

Figure 2.7 Valence quark diagram for the decay of a typical class I decay.

2.2.3 Models of Non-leptonic B Meson Decays

The previous section concluded with the QCD corrected weak Hamiltonian. The derivation showed how QCD corrections modify the bare weak Hamiltonian and how the effective neutral current term arises from the exchange of hard gluons between different quark currents. Also, the derivation showed that two scale dependent coefficients, each multiplying its own effective weak currents, absorb all relevant QCD effects. In this section we describe how the effective Hamiltonian is used to find the amplitude for the decay of the heavy flavor meson.

We begin by rewriting the Hamiltonian, Equation (2.9), with all effective charged and neutral currents terms grouped together. The Hamiltonian is

$$
\begin{aligned}
H_{eff} = \frac{G_F}{\sqrt{2}} V_{cb} V_{ud}^* \Big\{ C_1 \left[\bar{c}_i \gamma^\sigma (1-\gamma_5) b^i \bar{d}_j \gamma_\sigma (1-\gamma_5) u^j \right] \\
+ C_2 \left[\bar{c}_i \gamma^\sigma (1-\gamma_5) u^j \cdot \bar{d}_j \gamma_\sigma (1-\gamma_5) b^i \right] \Big\}
\end{aligned}
\tag{2.13}
$$

where

$$
C_1 = \frac{C_+ + C_-}{2} \quad \text{and} \quad C_2 = \frac{C_+ - C_-}{2}. \tag{2.14}
$$

are known as the scale dependent Wilson coefficients [22].

Each term in Equation (2.13) corresponds to one of the valence quark diagrams shown in Figure 2.7. Parts (a) and (b) correspond to the first and second term in Equation (2.13) respectively. The quark color structure of the first term forms combinations which are color-singlets and thus lead directly to real hadrons. In the second term the color degrees of freedom are mixed. We can obtain a color-singlet flavor combination by performing another Fierz transformation on the color mixed term. Applying the transformation, Equation (2.6), to the second term in Equation (2.13) projects out a color-singlet which now gets multiplied by $1/N_c$ and introduces an octet term $\mathcal{O}_1$. The effective Hamiltonian is now

$$
H_{eff} = \frac{G_F}{\sqrt{2}} V_{cb} V_{ud}^* \Big\{ a_1 \left[\bar{c}_i \gamma^\sigma (1-\gamma_5) b^i \bar{d}_j \gamma_\sigma (1-\gamma_5) u^j \right] + \mathcal{O}_1 \Big\}. \tag{2.15}
$$

where

$$
a_1 = C_1 + \frac{1}{N_c} C_2 \quad \text{and} \quad \mathcal{O}_1 \propto \bar{c} \gamma^\sigma (1-\gamma_5) \left(\frac{\lambda^a}{2} \right) b \bar{d} \gamma_\sigma (1-\gamma_5) \left(\frac{\lambda_a}{2} \right) u \tag{2.16}
$$

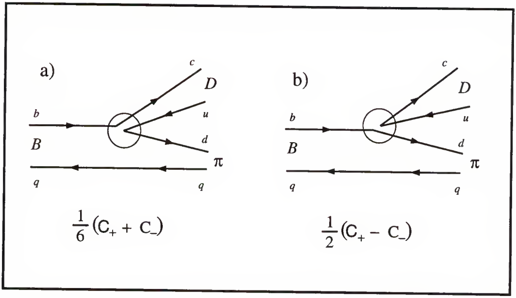

Figure 2.8 Valence quark diagram for the decay of a typical class II decay.

The preceding discussion involved class I decay channels were the external spectator diagram dominates. In a similar way, the amplitude for class II decays can be obtained by relabeling the valence quarks in Figure 2.7 (see Figure 2.8) to reflect the flavor combinations of an internal spectator process. Rearrangement of the quark fields gives

$$H_{eff} = \frac{G_F}{\sqrt{2}} V_{cb} V_{ud}^* \left\{ a_2 \left[\bar{c}_i \gamma^\sigma (1-\gamma_5) u^i \bar{d}_j \gamma_\sigma (1-\gamma_5) b^j \right] + \mathcal{O}_2 \right\}. \qquad (2.17)$$

which now a represents the quark flavor and color structure in class II decays. The new coefficient a_2 and operator $\mathcal{O}_2$ are analogous to those derived for class I decays. They are defined as

$$a_2 = C_2 + \frac{1}{N_c} C_1 \quad \text{and} \quad \mathcal{O}_2 \propto \bar{c}\gamma^\sigma (1-\gamma_5) \left(\frac{\lambda^a}{2}\right) u \bar{d} \gamma_\sigma (1-\gamma_5) \left(\frac{\lambda_a}{2}\right) b. \quad (2.18)$$

In Equations (2.15) and (2.17) the effective Hamiltonians are expressed as functions of two operators, a color-singlet and an color-octet. Since we ultimately want to evaluate amplitudes of decay processes which involve transitions between real hadronic states the effective Hamiltonian expressed in this way lends itself to this task if we find some way to deal with the octet term. If the hadrons where indeed pure singlets then the octet term vanishes by color conservation. However, hadrons are not pure singlets, they are instead complicated objects which consist of many gluon and $q\bar{q}$ pairs which can interact with the octet term and thus affect the overall amplitude. In the usual treatment, the hadron is assumed to be a color-singlet and thus the octet term can be ignored. While this procedure is somewhat ambiguous and perhaps unjustified [19,23,18], it leads to simplifications which allow the calculations of the matrix elements from the effective Hamiltonian described above.

<u>The factorization hypothesis.</u> Most current models of non-leptonic decays employ the factorization assumption in which the overall amplitude is written as the product of two matrix elements. Each matrix element describes separately the transition between the initial heavy meson and one of the daughters and the creation, from the vacuum, of its decay partner. In this way the amplitude can be evaluated by writing the matrix elements in terms of *form factors* and decay constants. These can be either determined by direct comparison to semi-leptonic decays or by theoretical model calculations.

There are heuristic arguments that attempt a justification of the factorization hypothesis in certain kinematic regimes. At large momentum transfer the expectation is that the $(u\bar{d})$ quark-pair produced at the W vertex, which at this stage is a point-like color-singlet, leaves the interaction region before its dipole moment becomes sufficiently large to interact with the color field surrounding the spectator quark system. One can estimate the hadronization scale by finding the time it takes the $(u\bar{d})$ to be 1 fm apart, the typical strong interaction range. While the u and $\bar{d}$ are flying apart they are also moving away from the spectator quark system. If by the time the u and $\bar{d}$ are approximately 1 fm apart the pair is more than 1 fm away from the spectator system, the $u\bar{d}$ pair is thought to have escaped the effects of the color field surrounding the spectator system. For decay modes where the B meson decays to $D^{(*)+}$ (class I) the hadronization scale is reached when the quark-pair is about 20 fm away from the spectator system [19]. For class II decays the hadronization scale is reached sooner, about 1-2 fm, so it is not clear if factorization holds in this class of decays. Recently Dugan and Grinstein [24] have argued that some basis exists in QCD for factorization in appropriate kinematic regimes.

Amplitudes in the factorization approximation. We may now proceed to evaluate the amplitude of a particular reaction in the factorization approximation. To clarify the discussion we consider class I modes where the B meson decays to $D^{(*)+}$ plus a "light" partner. These decays correspond to the H_{eff} described by Equation (2.15). Their amplitudes are given by

$$A^0 = \langle D^{(*)+} h^- | H_{eff} | \bar{B}^0 \rangle.$$

where $h = \pi, \rho, a_1$.

Under the factorization hypothesis this can written in terms of the two independent matrix elements

$$A^0 = \frac{G_F}{\sqrt{2}} V_{cb} V_{ud}^* a_1 \langle h^- | \bar{d} \gamma_\mu (1-\gamma_5) u | 0 \rangle \langle D^{(*)+} | \bar{c} \gamma^\mu (1-\gamma_5) b | \bar{B}^0 \rangle \qquad (2.19)$$

The matrix element which takes the initial B meson to a charmed meson can be expressed in a covariant way by taking all possible combinations of the available Lorentz 4-vectors. In decay to a pseudoscalar charmed meson two terms are required since only two linearly independent Lorentz 4-vectors can be formed. The hadronic matrix element can be parameterized by

$$\begin{aligned}\langle D^+(p')|\bar{c}\gamma^\mu b|\bar{B}^0(p)\rangle = &\left\{(p+p')^\mu - \frac{m_B^2 - m_D^2}{q^2}(p-p')^\mu\right\}F_1(q^2) \\ &+ \frac{m_B^2 - m_D^2}{q^2}(p-p')^\mu F_0(q^2)\end{aligned} \tag{2.20}$$

where $q = p' - p$. For transitions to a vector charmed meson the Lorentz decomposition takes on a more complicated form due to the addition of the D^* polarization vector. This gives four possible combinations, each of which must be linear in the polarization vector [23]

$$\begin{aligned}\langle D^{*+}(\epsilon,p')|\bar{c}\gamma^\mu b|\bar{B}^0(p)\rangle &= \frac{2V(q^2)}{m_B + m_D^*}\epsilon^{\mu\nu\rho\sigma}\epsilon^*_\nu p_\rho p'_\sigma \\ \langle D^{*+}(\epsilon,p')|\bar{c}\gamma^\mu\gamma_5 b|\bar{B}^0(p)\rangle &= +i(m_B+m_{D^*})\left[\epsilon^*_\mu - \frac{\epsilon^*\cdot q}{q^2}q_\mu\right]A_1(q^2) \\ &\quad -i\frac{\epsilon^*\cdot q}{(m_B+m_{D^*})}\left[(p+p')_\mu - \frac{(m_B^2 - m_{D^*}^2)}{q^2}q_\mu\right]A_2(q^2) \\ &\quad - i\epsilon^*\cdot q\frac{2m_V}{q^2}q_\mu A_0(q^2).\end{aligned} \tag{2.20}$$

The coefficients $F_0(q^2), F_1(q^2), V(q^2), A_0(q^2), A_1(q^2)$ and $A_2(q^2)$ are known as *form factors* and their q^2 evolution are somewhat model dependent but usually taken to be a simple pole formula [20]

$$F(q^2) = \frac{F(0)}{(1-\frac{q^2}{M^2})^n}. \tag{2.21}$$

The pole mass is given by the lowest lying meson with appropriate quantum numbers ($J^P = 0^+$ for F_0, 1^- for F_1 and V, 1^+ for A_1 and A_2 and 0^- for A_0) [23].

The form factors at $q^2 = 0$ are also model dependent and various methods have been used to calculate them. In the BSW model a relativistic harmonic oscillator potential is used to expand the wavefunction of the initial and final state mesons. The weak hadronic currents are then written in terms of creation and annihilation operators and matrix elements are formed. The results are then compared with the parameterization above and the form factors at $q^2 = 0$ are obtained [25]. Recently Neubert, Rieckert, Stech and Xu have calculated the form factors by using HQET and a slightly modified version of the BSW model [19].

The creation from the vacuum of the pseudoscalar follows from the Lorentz structure of the current acting on the vacuum.

$$\langle \pi^- | \bar{d}\gamma_\mu\gamma_5 u | 0 \rangle = -if_\pi p_\mu.$$

The only Lorentz 4-vector here is the 4-momentum of the pion and the matrix element is expressed as a the product of this 4-vector and the decay constant f_π. The creation of a vector from the vacuum is given similarly by

$$\langle v^- | \bar{d}\gamma_\mu u | 0 \rangle = f_v \epsilon^*_\mu m_v.$$

The decay constants are determined experimentally by measurements in e^+e^- annihilation, leptonic decays or by extracting them from other process such as $\tau \to h\nu_\tau$ decays.

The Bauer Stech and Wirbel approach. In the discussion above factorization was assumed to hold strictly as in semileptonic decays where the leptons produced at the W vertex do not interact with the color field. This assumption allowed us to drop the color-octet term which is as already described thought to be not completely justifiable. There are, in addition, other ambiguities inherent in the procedure above. These involve the exact scale at which to evaluate the QCD coefficients [19]. Also the extent to which non-perturbative effects are ignored is another source of concern in the usual treatments of heavy quark decay. These ambiguities lead Bauer, Stech and Wirbel [25,26] to propose that the coefficients a_1 and a_2 should instead be treated as free parameters which can be determined from experiment. In this way processes that occur at similar energy scales can be compared to one another and decay rates which would otherwise be difficult to predict can be obtained. Usually the parameters a_1 and a_2 are written as

$$\begin{aligned} a_1 =& C_1(\mu) + \xi C_2(\mu) \\ a_2 =& C_2(\mu) + \xi C_1(\mu) \end{aligned} \tag{2.22}$$

where $\xi = 1/N_c$ is the variable instead. By allowing these coefficients to vary non-factorizable contributions are given a means by which to enter the calculation without the need to know how to evaluate terms which contain color-octet currents, the energy scale to use and how to include non-perturbative effects.

CHAPTER 3
EXPERIMENTAL APPARATUS: THE CLEO II EXPERIMENT

Introduction

The data used in this analysis were collected at the CESR e^+e^- storage ring with the CLEO II detector. The CLEO collaboration consists of over 200 members associated with 20 institutions in both Canada and the United States. These scientists are primarily responsible for maintenance of the CLEO II detector, data taking and data analysis. The accelerator physicists at CESR are primarily involved in the development, maintenance and construction of the accelerator machinery. In this chapter we will briefly describe the machinery involved in providing the data used in the analysis. For a more complete description refer to the various published technical papers referred to in the text.

3.1 CESR: The Accelerator Complex

Figure 3.1 shows a schematic of the Cornell Electron Storage Ring (CESR) accelerator complex [27]. CESR is an electron-positron collider with a circumference of 758 meters. Currently, only the Southern interaction region is in use. It houses both the CLEO II experiment the detector complex for the Cornell High Energy Synchrotron Source (CHESS). The ring is operated in the neigh-

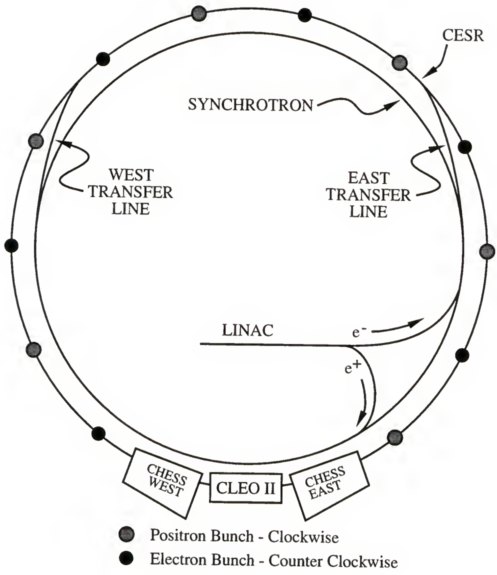

Figure 3.1 A schematic of the CESR accelerator facility.

Table 3.1

CESR operating parameters

Revolution Frequency	390 kHz
RF Frequency	500 MHz
Beam Energy Range	4.5-6.0 GeV
Fractional Beam Energy Spread	0.062 %
Energy Loss/turn at 5.3 GeV	1.14 MeV
Collision Frequency	2.7 MHz
Bunch Length	1.7 cm
Peak Luminosity	$2.5 \times 10^{32}\mathrm{cm}^{-2}\mathrm{s}^{-1}$

borhood of 5.3 GeV with a peak luminosity of $2.9 \times 10^{32}\mathrm{cm}^{-2}\mathrm{s}^{-2}$. These and other CESR parameters are listed in Table 3.1.

The positron beam fill procedure is divided into a series of steps. First electrons are boiled off a filament wire and accelerated in the linear accelerator (LINAC). To create the positrons, the electrons are directed towards a tungsten target half way down the LINAC. The collision between the electrons and the tungsten target induce pair production from which the positrons are electromagnetically separated from the debris and accelerated to 150 MeV by the LINAC. The positrons are subsequently introduced in to the synchrotron where their energy is increased to the operating energy, about 5.3 GeV. Finally, the particles are injected into the storage ring where they are prepared for collisions with the electron and will remain until the beams degradation warrants another fill. The electrons are accelerated in the same sequence of steps but the conversion process is omitted. CESR is operated with seven counter-rotating bunches of electrons and positrons. The bunch size is needle shaped, 0.16 by 0.011 mm and 17 cm long. Each bunch contains approximately 1.4×10^{11} particles.

During injection the bunches are kept apart by electrostatic separators. The separators shepherd the electrons and positrons into separate "pretzel" like circular orbits which are not allowed to intersect at any point. After the injection procedure is complete, the separators are powered down and the bunched orbits are allowed to intersect at the South interaction region.

The curved path of the electrons and positrons can then radiate energy, a phenomena known as synchrotron radiation. For highly relativist electrons, the energy radiated per particle per turn is given by

$$\Delta E = \frac{4\pi}{3}\frac{e^2}{\rho}\left(\frac{E}{m_e c^2}\right)^4$$

where e is the charge of the electron, ρ is the radius of the ring and E is the energy of the electron. At typical CESR energies, the losses due to synchrotron radiation amount to about 0.5 MeV per turn. To compensate for the losses, the storage ring uses two 500 MHz radio-frequency (rf) cavities which provide a "kick" to the electrons and positrons, replenishing their lost energy.

3.2 The CLEO II Detector Hardware

The CLEO II detector is a solenoidal detector that combines excellent charged particle detection with a high resolution electromagnetic calorimeter. It was installed in the fall of 1988 and superseded the existing CLEO detector with improved time-of-flight detectors, muon detectors and added the cesium iodide (CsI) crystal calorimeter. The concentric detector design consists of three drift chambers, a time-of-flight system, the crystal calorimeter and the

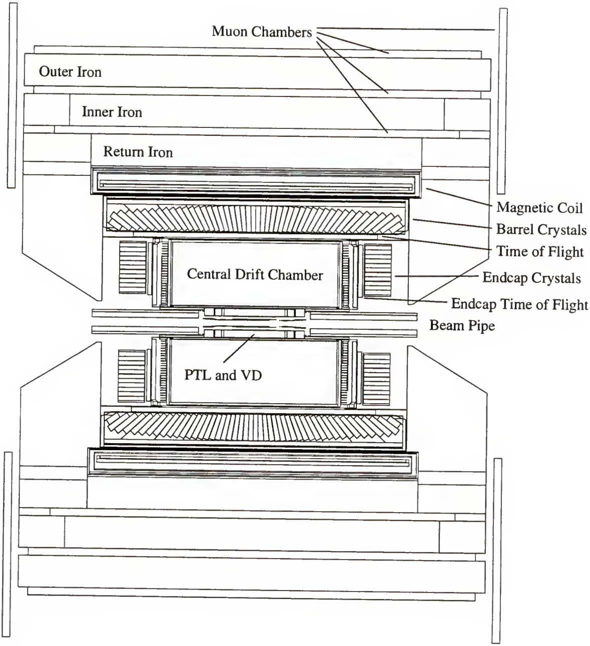

Figure 3.2 A cross-sectional view of the CLEO II detector.

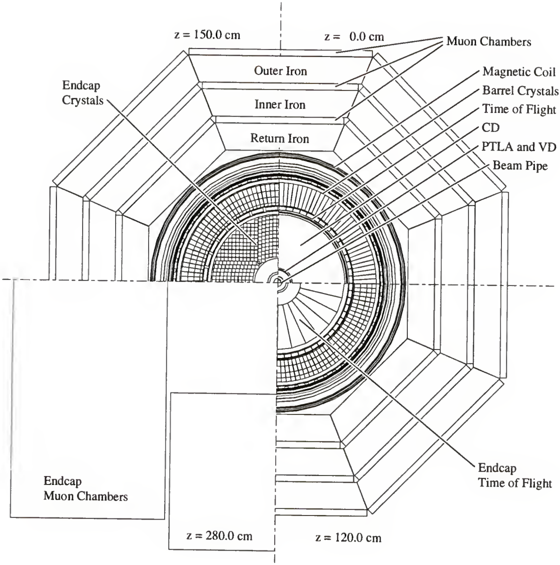

Figure 3.3 Endcap view with several different position along the z direction.

muon detector. All but the muon detector element are immersed in a 1.5 tesla superconducting coil 1.5 meters in radius.

The complete detector is throughly described in Ref. [28]. In this chapter we will briefly sketch the various components. The elements will be described in order of radial distance. A schematic drawing of the whole detector, in cross-section and in end view is shown in Figures 3.2 and 3.3.

3.2.1 The Beam Pipe

To separate the detector volume from the vacuum system of CESR a thin-walled beryllium beam pipe surrounds the interaction region. The beam pipe is 33 cm long and has a radius of 3.5 cm. To reduce the incidence of synchrotron radiation on the detector volume, the inner wall of the beam pipe is coated with a thin layer of sliver, 25 microns thick and an even thinner layer of nickel, less than 1 micron thick. The thickness of the beam pipe is is 500 μm and presents a total of 0.4% radiation length of material in the radial direction.

3.2.2 Charged Particle Tracking System

Charge particle trajectories are measured in CLEO II by a series of three concentric wire drift chambers. The common axis is aligned along the beam direction. The three drift chamber achieve different goals which would otherwise be difficult to achieve by a single detector element. Each drift chamber provides precise track position measurements by recording the drift-time of electrons which arrive at the sense anode wire. As a charged particle travels through the drift chamber, it ionizes the atoms in the gas filled volume. The electrons released in the ionization process drift in the electric field produced by the field wires and are collected by the sense wire. Knowledge of the electron drift-time to distance allows for a precise determination of the particle's path. The curvature of the path and knowledge of the axial magnetic field are used to find the momentum of the particle. The two outer drift chambers also provide information on the z position of the track. Specific ionization energy loss measurements, from the outer drift chamber are used for particle identification.

All three tracking chambers and the muon detector are fed a constant supply of argon-ethane gas. The 50% argon 50% ethane (C_2H_6) mixture is delivered by a complicated gas circulation system design to maintain a stable flow and operating pressure to the various detector subsystems while providing continuous monitoring of flow rates and gas compositions. In the Spring of 1992, the argon-ethane gas mixture in the precision tracking layer was replaced by di-methyl ethane (DME) gas to improve tracking resolution. The change occured between the first and second half of the data sample used in this analysis.

<u>The precision tracking layers (PTL).</u> The layer closest to the beam pipe is the precision tracking (PTL). It provides precise measurements of transverse particle position near the interaction region to determine particle directions and to separate primary from secondary vertices.

The PTL is a six-layer straw tube chamber with 64 axial wires per layer. Each layer is staggered by a half cell from the adjacent layer. The field cage for each tube is defined by an aluminized Mylar tube instead of cathode wires utilized by the two outer drift chambers. Within each Mylar tube lies a gold-plated tungsten sense wire, 15 μm in diameter. The single hit resolution of

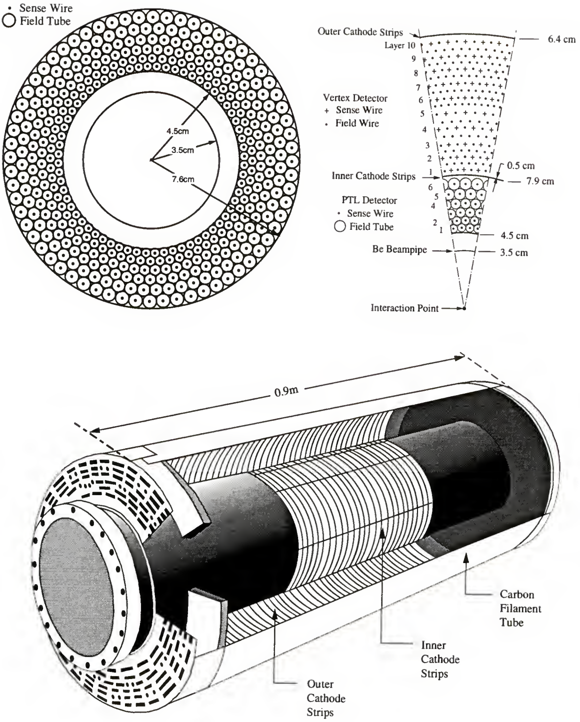

Figure 3.4 Schematic views of the PTL and the VD.

The top left figure shows a cross-sectional view of the PTL straw tube assembly. The top right figure shows the sense and field wire configuration of both the PTL and the VD. The bottom figure shows the segmented cathode array of the VD.

wires is 50 μm rms with di-methyl gas. The diameter of each tube is determined by its distance from the interaction point such that each tube makes contact with all neighboring tubes in adjacent layers. The tubes are glued together for mechanical stability and internal alignment. The detector assembly, including the inner and outer walls, is 33 cm long and extends radially from 4.5 cm, just outside the beam pipe, to 8.1 cm. A schematic of the PTL is show in figure 3.4. Neither polar angle nor track z position measurements are provided by this detector element.

The vertex detector (VD). The intermediate drift chamber, originally installed as a the vertex detector in the CLEO I experiment, provides for both azimuthal position measurements and position measurements along the z direction. The spacing and cell widths in this detector element are 70% smaller than the outer drift chamber providing better granularity for track separation. The detector also provides for position measurements along the z direction with two layers of segmented cathodes readouts and charge division on all sense wires.

Transverse particle momenta are determined by measurements of track azimuthal position collected with a total of 800 sense wires. The sense wires are interspersed with 2272 field wires which define hexagonal cell boundaries around each field wire. The cells are arranged into 10 axial layers of various sizes to completely fill the volume. The layers are divided into two groups. The inner group, layers 1 through 5, have 64 cells per layer while the outer, layers 6 through 10, have 96 cells per layer. All cells between layers are staggered by half a cell within each group. The wire configuration of the VD is shown schematically in Figure 3.4. The single hit resolution is 90 μm in the $(r - \phi)$ plane, and has a single hit efficiency of 95%.

The inner and outer surfaces consist of segmented cathodes which define the inner and outer field cage. The segmentation is 5.85 (6.85) mm along the beam direction on the inner and (outer) cathode surface. The sense wires are made of a nickel-chromium alloy with about three times the resistivity of gold plated tungsten and are instrumented for charge division measurements. The segmented cathodes and charge division provide for polar track measurements. The resolution of the cathodes is 750 μm.

The drift chamber (DR). The outer drift chamber (DR) provides track position measurements in both the azimuth and z directions [29]. These measurements, together with measurements obtained with both the VD and PTL, are used to determine the particle's transverse momentum (p_t), the radial distance of closest approach of the track projected back to the interaction point and the azimuthal (ϕ) direction. The outer drift chamber alone is used to measure the specific ionization energy loss (dE/dx) for particle identification.

The outer drift chamber consists of small rectangular cells, all of nearly equal size, that fill the entire volume. A total of 12240 sense wires are interspersed with 36240 field wires. The cells are arranged in a pattern of 51 layers with three field wires for each sense wire. The layers are grouped in fives or threes, with equal number of wires per layer within each group. To resolve left-right track sign ambiguity, the cells are staggered by half a cell with respect to its nearest neighbor in the radial direction within each group. The groups of five or three layers are separated by a single layer of stereo sense wires. Eleven of the 51 wire layers are stereo layers.

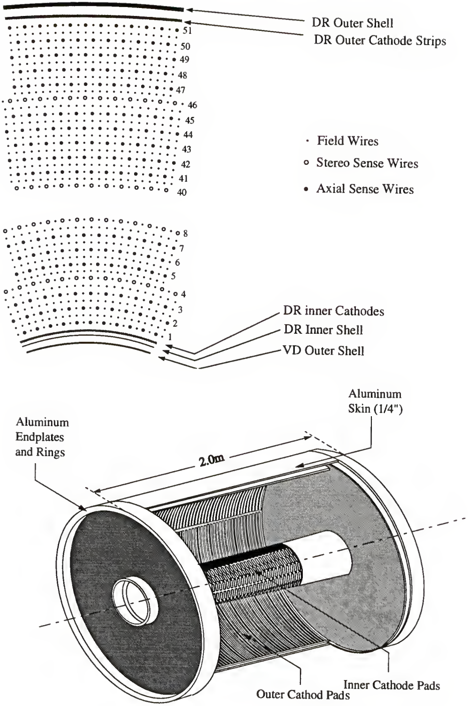

Figure 3.5 Schematic views of the drift chamber.

The top figure shows the field, sense and stereo sense wire configuration for the drift chamber. The bottom figure shows the inner and outer cathode arrays, the endplates and support structure of the drift chamber.

Table 3.2

Material contribution of the various detector elements

Detector Element	Amount of Material (% R.L.)
Beam Pipe	0.40
B.P./PTL interface	0.06
PTL	0.29
PTL/VD interface	0.63
VD	0.04
VD/DR interface	1.09
DR	0.42

The stereo wires are positioned at various small angles relative to the axial direction. The sign and magnitude of the angle vary as a function of radii. The wires in the first stereo layer are positioned at 3.77°, the second is at −4.22° the last two at −6.45° and 6.89°, respectively [30]. All sense wires are 20 μm diameter gold-plated tungsten, the field wires are made of gold-plated aluminum (layers 1-40) and gold-plated copper-beryllium layers (41-51).

The outer and inner volume are defined by segment cathodes surfaces. These, as in the VD, form the field cage for the inner and outer surface wire layers. The segmented anodes, together with the stereo sense wires provide for polar angle measurements. A schematic of the DR is shown in Figure 3.5.

Momentum and angular resolution. The momentum resolution can be parameterized by two components. One component, due to distortion of the track's true helix, is caused by multiple scattering as the particles traverses

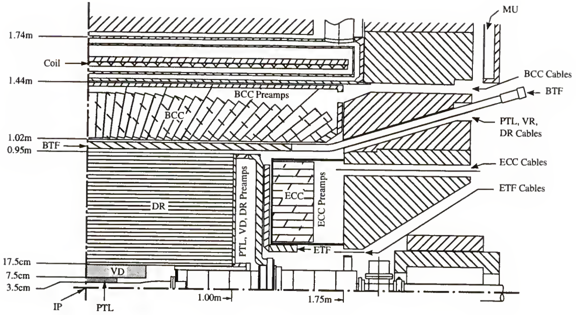

Figure 3.6 A view of a quadrant of the CLEO II detector.

the various detector elements. A substantial portion of the scattering material, 1.08% radiation lengths, lies at the interface between the intermediate and outer drift chambers. To minimize the effect of the concentration of material, a kink is allowed in track fitting at the radius of this interface. A second component is due to the error in measuring the track curvature due to individual measurement errors in the drift distance. Both of these components contribute to the transverse momentum resolution as [30]

$$\left(\frac{\delta p_t}{p_t}\right)^2 = \left(\frac{53 s p_t}{BL^2\sqrt{n}}\right)^2 + \left(\frac{0.054\sqrt{t}}{BL}\right)^2$$

where s (in meters) is the accuracy of the individual position measurements, p_t (in GeV) is the transverse momentum, B is the magnetic field in tesla, L is the length (in meters over which measurements are made), n is number of position measurements and t is the thickness of material in radiation lengths.

The expected momentum resolution for a particle with sufficient momentum to traverse the entire tracking chamber is

$$\left(\frac{\delta p_t}{p_t}\right)^2 = (0.0011 p_t)^2 + (0.0067)^2$$

with $B = 1.5$ T, $s = 150$ μm, $n = 49$, $L = 0.85$ m, and $t = 0.025$ r.l.. The scattering material, in radiation lengths, of the detector elements are listed in Table 3.2. An expanded side view of the CLEO II detector is illustrated in figure 3.6showing the relative positions of the various detector elements.

The angular resolution of the combined detector elements is obtained by studying a sample of $e^+e^- \to \mu^+\mu^-$ events. These events provide an estimate for the resolution at high momentum. The rms measured resolutions are

$$\delta\phi = 1 \text{ mrad}; \;\; \delta\theta = 4 \text{ mrad}$$

where $\delta\phi$ and $\delta\theta$ are the resolutions in azimuth and polar angles, respectively. The larger resolution in polar angle is due to the smaller number, a maximum of 15 measurements, and diminished accuracy of polar measurements made.

Particle identification. The identity of charged tracks are obtained through specific energy loss measurements performed by the 51 layer outer drift chamber. The energy loss at each hit point is determined by measuring the charge collected on the sense wire. The raw measurements are then corrected for dip angle, drift distance, entrance angle and proximity to the stereo layers. A five-dimensional 1600 bin mapping is calibrated and then used to correct the charge associated with each hit. For tracks associated with 40 or more good hits, resolutions of 6.2% for Bhabhas and 7.1% for minimum ionizing pions

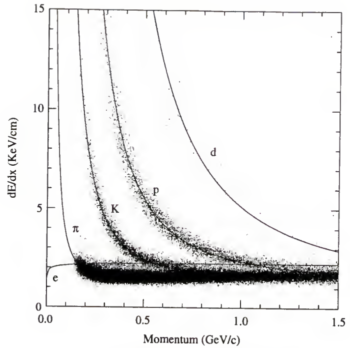

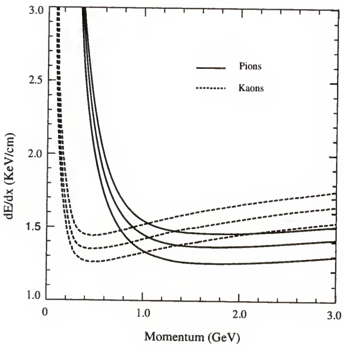

Figure 3.7 Energy loss (dE/dx) as a function of particle momenta.

The top figure shows the two dimensional scatter plot of real data. For clarity, the bottom figure depicts the centroid and 1σ bands for charged pions and kaons.

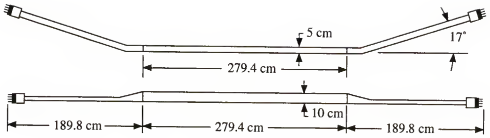

Figure 3.8 Barrel time-of-flight counter.

are obtained. The dE/dx system provides $K\pi$ separation, at the 2σ level, for tracks of momentum up to 700 MeV.

The specific ionization energy losses are a function of the velocity of the particle. By plotting the dE/dx as function of momentum the particles separate into distinct bands. Figure 3.7 shows the particle identification capabilities of the CLEO II detector. Present in the plot are the bands formed by electrons, charged pions and kaons, protons and deuterons. The latter are formed predominantly by beam wall collisions.

3.2.3 Time of Flight System

The time-of-flight (TOF) system is used primarily as a fast primary trigger in data recording and as a tool for particle identification. Particle identification is obtained by measuring the time it takes a particle to reach the TOF scintillation counter referenced to CESR timing. The TOF system consists of two major components, the barrel and endcap time-of-flight systems. The barrel counters cover the polar angle region from 36° to 144°. The endcap counters cover the region from 15° to 36° and 144° to 165°. The solid angle subtended by the combination of barrel and endcap counters is 97% of 4π.

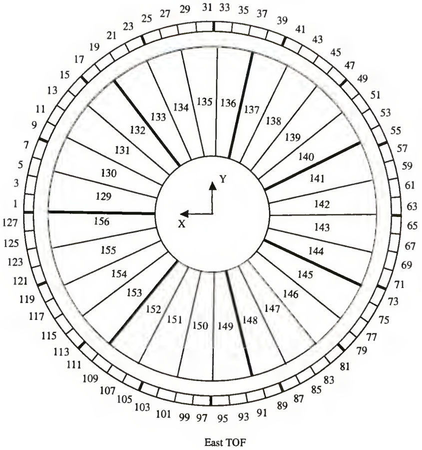

Figure 3.9 Endcap time-of-flight counters.

<u>Barrel time-of-flight counters.</u> Figure 3.8 is a drawing of a single barrel time-of-flight counter. There are a total of 64 barrel counters strapped to the inside surface of the crystal calorimeter. The counter assembly consist of a organic scintillation material (Bicron BC-408) optically connected to a UVT lucite light pipe. The scintillation material is 5 cm thick. The size is chosen to maximize the thickness without degrading the performance of the CsI calorimeter. The scintillation signals are collected by photomultipliers glued to both ends of the light pipe; each barrel TOF counter is thus readout by two photomultipliers.

Endcap time-of-flight counters. A drawing of the endcap time-of-flight counters is shown in Figure 3.9. The figure shows the endcap TOF counter configuration and the relative location of the barrel counters. The numbers on the barrel counters represent the phototube addresses for the east-end phototubes. Since each barrel counters is readout out by two phototubes, the west-end phototube addresses are even numbered.

There are 28 wedge-shaped counters mounted in a circle on each endcap calorimeter. The thickness and scintillation material are identical to the barrel counters but the geometrical design differs since the endcap counters are designed to record particle as they travel through the ends of the detector. The narrow end of the scintillators are shaped into a 45° prism upon which is attached a photomultiplier tube. This configuration reduces the need for long light guides and additional glue joint which would degrade the endcap TOF performance.

Particle identification and timing resolution. To obtain timing resolutions in the time-of-flight system, a sample of Bhabhas events was used in the calibration procedure. The measured time-of-flights are calculated from events for which there is only one hit per counter and the momentum and trajectory of the electron are known. The timing measurement is then calculated from phototube TDC counts and electronic calibration constants. The phototube measurement T_{mij} is then compared to the expected time, T_{ij}. The expected time is parameterizes by various quantities which relate the physical properties of the counters and detector system. They include the time require for an electron to move from the interaction point (IP) to the scintillator, the distance

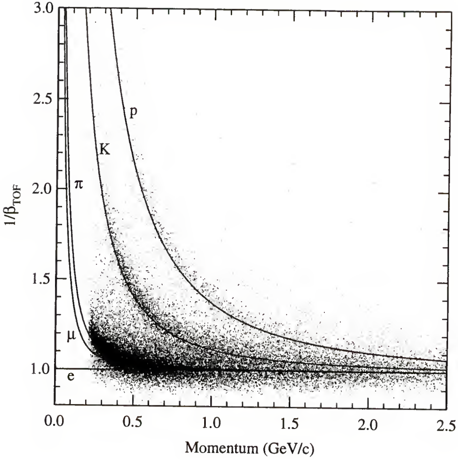

Figure 3.10 Barrel time-of-flight $1/\beta$ versus track momenta.

between the point where electron crosses the scintillator to the end of the scintillator, the pulse height and shape of the signal, the offset constant for each channel and the velocity of the signal propagation. Three parameters, the time of flight from the IP, the velocity of signal propagation and the pulse shapes are determined by minimizing the difference between the measured and expected time-of-flight with the Bhabha data. Allowing each phototube to have independent velocity parameters results in a resolution of 139 ps for Bhabhas in the barrel TOF. For pions from hadronic events, with momentum greater than 700 MeV, the resolution obtained was 154 ps rms. The timing resolution provides a 2σ separation for pions and kaons at a momenta of 1.1 GeV. The separation of hadrons as a function of momenta is shown in Figure 3.10. The plot derives from hadronic events at the $\Upsilon(4S)$.

With a similar calibration procedure, the resolution of the endcap time-of-flight counters are also determined from Bhabhas events. The timing resolution in the endcaps is 272 ps. Calibrating the endcaps counters proves to be a more difficult task since advantage of the position dependent correlations cannot be taken in counters readout by only one phototube. Also, the use of Bhabhas complicates the calibrations procedure due to the spread in timing from the conversion of secondary electrons in the drift chamber endplates.

3.2.4 Electromagnetic Calorimeter

The electromagnetic calorimeter consists of 7,800 thallium-doped cesium iodide (CsI) crystals, and like the TOF system, is divided into barrel and endcap portions. The large number of crystals provides for an angular segmentation finer, by an order of magnitude, than previous generations of of crystal detectors at e^+e^- facilities [30].

The barrel crystal calorimeter. The barrel and two endcaps together cover 95% of the solid angle. The barrel coverage starts at a polar angle of 32°, overlapping with the endcap which ends at 36°. Each barrel crystal is shaped into a tapered rectangular block approximately 5 cm square by 30 cm (16 r.l.) long. There are 6144 crystals in the barrel portion of the calorimeter. These are arranged into a nearly vertex-pointing geometry of 48 rows along the z direction with each row segment containing 128 blocks along the azimuth. The z-rows are located symmetrically

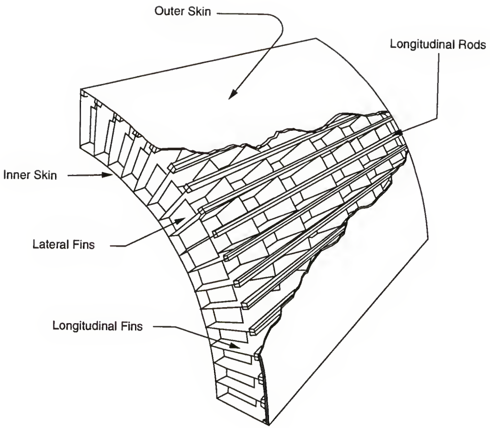

Figure 3.11 Barrel crystal calorimeter holder.

about the axial direction and have identical tapered shapes. The shapes and gaps between blocks were selected such that photons originating at the interaction region strike the barrel at nearly normal incidence. The crystals are held in place by the crystal holder shown in Figure 3.11. This structure not only bears the considerable weight of the entire crystal calorimeter assembly, approximately 27×10^3 kg, but also provides a clean and dust free environment for each individual crystal block.

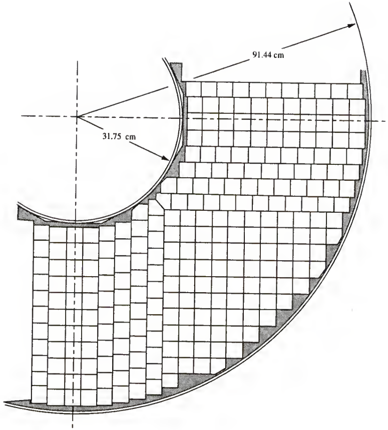

Figure 3.12 Single quadrant endcap crystal geometry.

The endcap crystal calorimeter. Each endcap portion of the crystal calorimeter consists of 828 CsI rectangular blocks 5 cm square by 30 cm long. These are arranged as shown in Figure 3.12. The pattern of 207 blocks is repeated every 90° forming a four-fold symmetric pattern. The aluminum holder has an inner radius of 0.321 and 0.914 meters, respectively, and is capped by circular cover plates. Each front plate is located 1.248 m from the interaction point.

The scintillation light from the CsI crystals is converted into electrical signals by four silicon photodiodes mounted on 6 mm thick UVT lucite window on the back of each crystal block. Each photodiode is connected to an independent nearby preamplifier. The four preamplifiers are connected to the mixer/shaper card, which sums the shapes and signals from each crystal for input to the ADC circuits.

Shower reconstruction. To reconstruct showers, crystals must be grouped together to form clusters of hits which define a single shower. The cluster finding algorithm first locates the most energetic crystal in a cluster that exceeds 10 MeV and has an energy higher than any of its immediate neighbors. Members of the same cluster can not be more than two blocks away from each other.

The energy and position of each cluster is then computed by taking the N most energetic crystals in the cluster. The value of N varies logarithmically as a function of energy from 4, at 25 MeV, to 17, at 4 GeV. These values of N are chosen to minimize the energy resolution. This algorithm proves to be the most effective possible [30]. If the crystal belongs to two separate cluster, its energy is apportioned between the two.

The position vector of each cluster is computed by first finding the centroid of the shower. The centroid is calculated as the energy-weighted sum of the coordinates of each crystal's geometric center. The vector is then corrected for shower location in the plane perpendicular to the incident particle's direction and depth within the cesium iodide where the an electromagnetic shower would have deposited its mean energy. The location of the shower within the crystal is important when matching showers to charged tracks and in assigning correct angular positions when showers fall in the endcap.

Performance of crystal calorimeter. Absolute crystal-to-crystal calibrations are calculated using Bhabha events. The constants are computed by minimizing the rms widths of the Bhabha electron shower energy distribution and constraining it to peak at the beam energy. To cover the entire photon energy range, various techniques are used to calibrate the absolute energy normalization for photon clusters. They include $\pi^0 \to \gamma\gamma$, radiative Bhabhas and two photon events. Photon pairs from π^0 decays, mass constraint imposed, yield a calibration accurate to about $\pm 0.5\%$ below 2 GeV. To sample higher energy photons, radiative Bhabhas are used, again resulting in calibration accuracies of $\pm 0.5\%$.

With these calibrations, the photon energy resolution in the barrel region is 1.5% at 5.0 GeV. In the endcap region the energy resolution degrades to 2.6%. At 5.0 GeV the angular resolution, in the azimuthal direction, is 3 mrad in the barrel and 9 mrad in the endcap regions. The angular and energy resolutions can parameterized in the barrel region by the expression

$$\frac{\sigma_E}{E}(\%) = \frac{0.35}{E^{0.75}} + 1.9 - 0.1E$$

$$\sigma_\phi(\mathrm{mrad}) = \frac{2.8}{\sqrt{E}} + 2.5 \qquad \sigma_\theta(\mathrm{mrad}) = 0.8\sigma_\phi \sin\theta$$

where the photon energy E is in GeV. In the endcap region the parameterization is

$$\frac{\sigma_E}{E}(\%) = \frac{0.26}{E} + 2.5$$

$$\sigma_\phi(\mathrm{mrad}) = \frac{3.7}{\sqrt{E}} + 7.3 \qquad \sigma_\theta(\mathrm{mrad}) = \frac{1.4}{\sqrt{E}} + 5.6.$$

These parameterizations come from Monte Carlo simulations of showers in the CLEO II detector. Not included in the simulation are effects due to other tracks in the event. The effects vary depending on the event topology and tend to slightly degrade the resolution.

3.2.5 The CLEO II Magnet

The CLEO II magnet consists of a 3.5 m long superconducting cylindrical coil with a bore of 2.9 meters and a large steel return yoke. The coil is cooled by liquid helium contained in a 700 l dewar mounted on top of the detector. The helium is delivered through natural flow circulation know as a thermosyphon system. The system is self regulating and avoids the need for liquid helium pumps which insures that refrigeration malfunctions will not result in a magnet quench.

The return yoke has three layers of steel interspersed with muon detection equipment and thus serves not only as a medium for the magnetic flux return but as a hadronic absorber. The entire assembly weighs about 8×10^5 kg, most of it in the slabs of steel arranged in an octagonal geometry around the coil.

The conductors used in the coil windings are flat high purity aluminum coextruded over Cu-NbTi wires. The flat wires measure 5×16 mm and were wound in two layers, one above the other. Both layers are mounted to the inner surface of the coil shell with insulation material and a radiation screen separating the coil assembly from the vacuum vessel surfaces. The wires carry a current of 3300 A which provide the 1.5 tesla field used to bend the paths of charged particles. The magnetic field is uniform to 0-.2% throughout the drift chamber volume. During data taking the magnetic field is monitored by NMR probes located a few centimeters beyond the end of drift chamber. The effective average magnetic field is calibrated by using event reconstruction involving μ pairs and known masses of particles such as D^0s, ϕs and K^0s. This

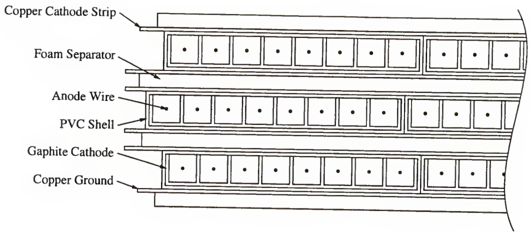

Figure 3.13 Schematic of muon detector superlayer.

yields a correction of 0.11% at the center of the magnet comparable to the overall accuracy of field measurements.

3.2.6 The Muon Chambers

The muon detector [31] is the last of the detectors component which will be described. It covers the polar angle range from 30° to 150°, about 85% of the solid angle. The barrel muon chambers are embedded in the iron yoke of the magnet at depths of 36, 72 and 108 cm (see Figures 3.2 and 3.3). The two ends of the detector are also covered by muon chambers. Depending of the direction of the track, the total equivalent thickness of iron absorber a particle sees varies from 7.2 to 10 radiation lengths.

The muon chambers are streamer counters operating in the proportional mode, at 2500 V. Within each iron gap there are three layers of counters, the middle layer staggered with respect to the other two. A schematic of the three layers (known as a superlayer) is shown in Figure 3.13. Each counter is about 5 m long by 8.3 cm wide and is divided into eight cells by graphite coated plastic walls which define the electric field cage. Within each cell lies 50 μm diameter sliver-plated Cu-Be anode wire. The eight anodes are ganged together giving a spatial resolution of 2.4 cm, better than the spatial uncertainty due to multiple scattering for particles reaching the muon chambers. Measurements along the z direction are provided by external copper strips positioned along the counter and by charge division readout of the anodes.

3.3 The Trigger Decision Levels

Over the data-taking period relevant to this analysis the beam-bunch configuration of CESR consisted of seven electrons positrons beams each consisting of seven bunches per beam. The collision rate between bunches in this configuration was 364 nsec for all but the first and last bunch where the interval was increased to 378 nsec. The beam crossing rate thus averages about 2.73 MHz. Considering the large number of channels involved and the non-negligible amount of time required to decide whether an particular event warrants a write to tape, reading-out the detector at this rate would prove to be extremely difficult. Also, interesting physics does not occur at every beam crossing. In fact, given the current CESR luminosity and the value of the hadronic cross-section suggests a more reasonable rate of a few tens of Hz. The CLEO II trigger system [32] was thus designed to take the 2.73 MHz bunch crossing time and read out the detector only at the occurrence of "interesting events".

3.3.1 Trigger Logic

To accomplish these goals a three tiered trigger system was devised. The different decision levels are referred to as L0, L1 and L2. Each successive trigger level requires that the previous level be satisfied. In the absence of

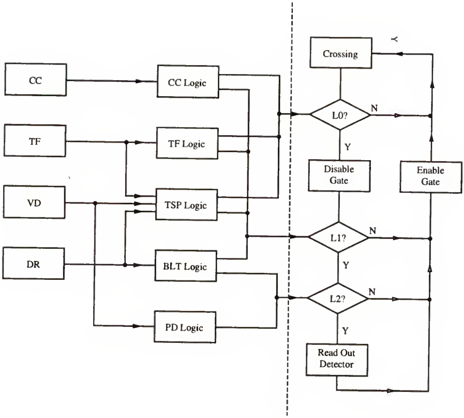

Figure 3.14 Flow of the tiered trigger in CLEO II.

triggers, the detector is actively collecting time and pulse height information and gated every beam crossing. Satisfying the L0 trigger disables the gate and a search for all L1 combinations defined is initiated. If all triggers are satisfied the detector is read out and the gate is enabled. The trigger logic is sketched in Figure 3.14. The various elements which feed information into the trigger logic circuits are depicted on the left-hand side, included are the TSP, BLT and PD logic algorithms which combine various detector element to do rudimentary track finding.

The level 0 (L0) trigger is very fast, very simple and quite discriminatory. It reduces the rate from the 2.73 MHz crossing frequency to 20 kHz. It receives input from the time-of-flight scintillators, from the vertex detector and from the CsI crystal calorimeter. The experimenter can define a set of criteria for L0, all of which are logically OR'd. The number of crossings "lost" when a valid L0 combination fails to find a valid L1 combination is currently six.

The L1 level trigger takes the 20 kHz rate from L0 and reduces it to 25 Hz. It takes its input from scintillators, vertex detector, central drift chamber and electromagnetic calorimeter. The time it takes for all of these devices to be ready for L1 integration is 1.0 μsec. With an L0 rate of 20 kHz this implies a dead-time of 2%. Each set of L1 criteria has its own set of L2 requirements which are examined once the particular L1 trigger is met. Currently the L2 trigger only takes input from the vertex detector and drift chamber. Additional readiness time from L2 only adds about 0.25% to the overall detector dead-time.

3.3.2 Trigger Inputs

Briefly outlined in the following section are the logic elements that contribute to the trigger system. A more detailed description of the various inputs can be found in Ref. [32].

Time-of-flight trigger logic. The time-of-flight system lends itself well to the trigger system due to its fast response time. Inputs to the trigger system from the TOF scintillators consists of ganging four adjacent counters into sectors which reduces the granularity of the detector. This coarsening effectively reduces both the time and number of bits required to readout the data.

Six flags are set involving various combination of endcap and barrel sector hits. These can be modified by the experimenter to select for different physics events.

Crystal calorimeter trigger logic. The inputs from the crystal calorimeter (CC) follows a similar pattern as with the TOF system. The barrel segmentation consists of 384 segments of 16 crystals per segment. The 828 crystals in the endcap are also grouped to form segments but here the number of crystal per segment vary from 6 to 16. The signals from the grouped segments are summed and the result is discriminated by both a high and low level comparator. The high being approximately twice the minimum ionizing while the low is half minimum ionizing. While all segments are readout for potential software triggers the L0 and L1 hardware triggers group these segments into larger sectors. In the barrel region the entire detector is divided into 16 sectors, eight along the azimuth and two along polar direction. The endcap segments are grouped into eight sectors each. All segments within a sector are logically OR'd. The choice of 16-sector topology is made to match the address space of commercially available fast static random access memory (RAM).

Drift chamber trigger logic. The drift chamber and vertex detector are used as input devices to the trigger system. Signals from these devices are incorporated into the trigger logic by using several algorithms. These perform crude track finding and also allow the experimenter to specify the charge particle multiplicities and momenta necessary for the acceptance of events. The Track Segment Processor (TSP) uses analog signals generated by charge collected on the anode wires in all layers of the vertex detector and 12 layers of the drift chamber at various radii from 0.21 to 0.87 meters. The TSP algorithm groups the anodes from the 10 VD and 12 DR layers into a total 200 bits of information. These serve as inputs to 32 PROMs (programmable read-only memory); each memory has as its address 10 bits, one from each layer aligned in azimuth. To find a track, each PROM compares the bit pattern of the event with the radial pattern expected from charged particles. Using a pattern recognition scheme, the TSP searches for and counts the number of short, medium and long tracks in the event. The definition of what constitutes a long, medium or short track defined at run-time. For long tracks, nominally defined as tracks that reach a radius of 0.21 meters, time-of-flight information is also added. Only the VD contributes to the L0 decisions. The drift chamber and time-of-flight counters are used in L1.

A second processor used in the L1 and L2 trigger decision level is the Binary Link Tracker (BLT) [33]. This processor groups the wires in the DR into gangs of wires to form segments consisting of 17 layers at various radii. The algorithm uses correlations between the bit pattern set by the various segments to find track momenta and multiplicity of the event. Combining the TSP and BLT processors increases the L1 efficiency by 5-10% over using the TSP alone. The BLT is also employed in the L2 decision level where more time is allowed for calculations. At this stage the BLT may be used to establish the sign of a track thus enabling the rejection of beam wall events which give a preponderance of positive tracks.

A third processor, the Precision Tracking Device (PD), uses the hit information exclusively from the vertex detector. By examining hit patterns which are consistent with tracks originating at the vertex, it helps in rejecting cosmic ray and beam related events. The algorithm also discriminates against a large number of hits clustered in a given azimuth, thus further biasing against beam-wall and beam-gas events. The PD is used in the level 2 decision.

3.4 Data Acquisition

A new data acquisition systems was installed in the Fall of 1991 to readout the CLEO II detector. The change was required to take advantage of the steadily increasing CESR luminosity and also to allow for the broadening of the search for interesting physics. Since the previous data acquisition system was used for less than a quarter of the data sample and has been described elsewhere [34] we will only present a brief description of the new data acquisition system, known as the DAQ90 system.

The DAQ90 system [35] is responsible for digitizing and collecting data from the 40 front-end detector creates reading out the various detector elements. It also sparsifies the data to remove unwanted information, formats the fragments into complete events and distributes them to the online workstation. The performance goals of the system is to handle a 50 Hz trigger rate with a dead time of no more than 10%. This corresponds to a bandwidth of 250 kBytes/s, for an average sparsified event size of 5 kBytes.

The DAQ90 system hardware is illustrated in Figure 3.15. The process of writing data to tape begins at the front-end crates where the pulse heights, timing information and position bits are readout and digitized from the various detector elements. As they are digitized, the data from each front-end crate is sent via a point to point connection to a remote dual-port RAM, link board, where they are buffered for subsequent transfer. After the transfer of data is

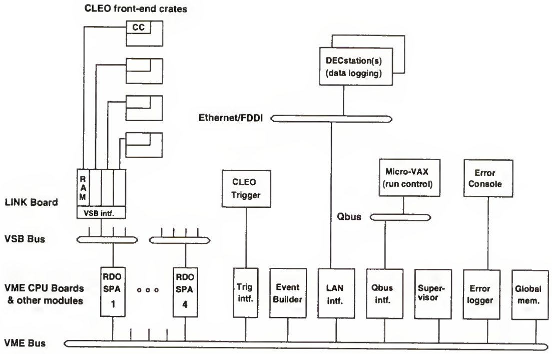

Figure 3.15 A block diagram of the DAQ90 hardware.

complete, each crate controller sends a "done" signal to its dedicated link. The data are then transfered from the link-board memory to VME memory once all link-board "done" signals have been received from its respective branch. The four VME CPU boards further process and sparsify the event, in parallel, while communicating with the task supervisor which sends signals to the trigger system and examines error logs. Once the sparcification of all event fragments is complete the sparsifier task (SPA) signals the event builder task (EVBD) that all event fragments are available. The EVBD then gets the data from buffers on the sparsifier nodes and merges the fragments into a ZEBRA-formatted event. The event consumer requests events from the event distributor and allows for the application of software filters. In the currently configuration a single event

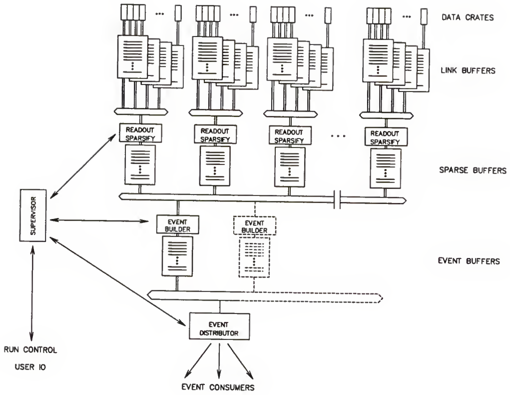

Figure 3.16 An illustration of the information flow in the DAQ90 system.

builder feeds a single event distributor, a DECstation 5000/240, which also runs the LVL3 software filter and delivers the data to another DECstation 5000 for on-line processing. The data flow, described above, is illustrated in Figure 3.16. The illustration shows how event fragments propagate through the series of buffers to arrive at the event distributor as a whole formatted, sparsified event.

3.5 The CLEO II Software

As with any High Energy experiment, the CLEO II software is comprised of many layers of utility programs, online and offline analysis routines and a multitude of user applications. It would require at least an additional 200 pages just to begin to describe all of the software components used to complete an analysis. Instead, in the concluding sections we will concentrate on describing the two main track fitting processors used in the online and offline reconstruction programs, sketch the procedure used to generate the Monte Carlo simulations of events and finally, outline the high level script language (CABS) used to fully reconstruct the decay modes considered in this analysis.

3.5.1 PASS1: The Online Analysis Program

The on-line analysis program, PASS1, runs on a DECstation 5000 connected through FDDI to the DAQ90 data acquisition system. It is the first pass at transforming the raw hit information, recorded at runtime, to fully reconstructed events. It is also used to monitor the operation of the experiment and to create the first set of calibration constants later used in the off-line analysis program, PASS2. PASS1 also provides event filtering, rejecting beam-wall, beam-gas and cosmic ray events and classifies the remaining events before storage onto 4 mm DAT tapes.

3.5.2 PASS2: The Offline Analysis Program

PASS2 is the off-line analysis program it also transforming raw hit information into fully reconstructed events consisting of charged and neutral tracks. The algorithms used are more sophisticated than those used in PASS1 and thus require more time. The main tracking algorithms used in PASS2 are TRIO and DUET [36]. These use the raw hit information and find tracks which fit a series of wire hits in a given event. TRIO is a fast system which takes advantage of the triplet geometry of the grouping of layers and the staggering of the tracking chamber cells to find tracks. The second program uses a tree finding algorithm that provides for more accurate track fitting and higher efficiency in find tracks. The TRIO algorithm, being much faster, is used in PASS1. Both DUET and TRIO are used in PASS2.

TRIO. The TRIO program searches for groups of three hits in consecutive layers forming units called tracklets. TRIO then forms combinations of inner and outer tracklets to create candidate tracks. Additional tracklets are included if they fall within a given distance and lie between the initial two tracklets. The average number of tracklets in a candidate track is four. The candidate track is then fit, and if of sufficient quality, added to the track list.

DUET. The DUET program starts off with seed tracks from TRIO. It looks for two hits segments within a narrow region of the candidate TRIO track. The segments, known as links, are then combined into larger and larger segments called chains. Candidate chains are fit to a circle and a straight line in the $r - \phi$ plane. Chains which satisfy the χ^2 requirement are refit, in three dimensions, to a helix. Once DUET exhausts all TRIO seed tracks, it begins its own search for tracks from hits unused in the initial search.

Other processor in PASS2. Both PASS1 and PASS2 run under the CLEVER [37] (CLEO EVEnt Reconstruction) program. It provides a fully interactive user interface to manipulate ZEBRA-formatted data. The user can select from among a series of analysis routines called PROCESSORS. In addition to TRIO and DUET, other processors are included in the PASS2 executable. These include the three processors, CCFC, CDCC and XBAL, which provide information on the raw crystal hits that allows for the formation of shower candidates. The CCFC routines find the position and angles of individual crystals (see Section 3.2.4) and the CDCC provides the routines to match showers to charged tracks. The XBAL routines provide an alternative way to access the crystal information. They are based on the clustering algorithms developed for the Crystal Ball experiment. Other processors do vertex finding (VFND), event filtering (LVL3 and BMWL), particle identification (TFAN and DEDR), and calculation of global event properties (GLOB). In addition, a processor called MAKR is used to compress the large, .fzx, ZEBRA-formatted files produced by CLEVER. It makes a DST (Data Summary "Tape") in ROAR format achieving lager compression factors by minimizing the storage by excluding raw hit information. The ROAR data format can then be unpacked by the analysis programs into FORTRAN common blocks.

3.5.3 Event Simulations

To understand the reconstruction efficiencies of the CLEO II detector and the effects of the various selection requirements imposed in the reconstruction algorithm, we use Monte Carlo simulations. The Monte Carlo is calibrated against world averages of previously well measured results. In this analysis the Monte Carlo simulations are used to find the detector acceptance necessary in determining absolute branching fractions. However, Using the Monte Carlo simulations to find these acceptances introduces systematic tracking errors which depends on the multiplicity and hadronic content of the event. The tracking error introduces a 2% (5%) error per charged track above (below) 250 MeV and 5.0% error per neutral pion. The tracking errors are also determined by calibrating the Monte Carlo to well measured processes.

The generation of Monte Carlo events begins with the event generator QQ, [38]. The program generates the initial four-vectors, event vertices and the general topology of the event. It was originally written to generate $q\bar{q}$, $B\bar{B}$ and ggg jets and has evolved into a shell structure which can call a variety of other event generators such KORALB to generate tau pairs and LUND/JETSET applied in hadronizing $q\bar{q}$ and ggg events. Once the events are created a lookup table with information on all known decay modes and branching fractions is used to decay the generated particles. A user can change the decay information of any particle. The angular distributions of all decays are also included in the lookup tables. These can also be specified or changed by the user.

The second step in the Monte Carlo chain is the detector simulation. The event history from QQ are saved in ZEBRA format and used as input to the CLEOG [39] program. CLEOG is the CLEO II interface to the GEANT [40] detector simulation routines. The job of CLEOG is to propagate each generated particle through the various detector element keeping track of multiple scattering, interactions with detector material, electron conversions and properly decaying long lived particles such the pions and kaons when needed. The response of each detector element is recored just as in a real event, digitized and written to banks in the same manner as the data. These data are then fed to the PASS2 routines used in track finding and fitting.

For this analysis millions of simulated events were used. These include two million events employed in the study of $B\bar{B}$ backgrounds and hundreds of thousands of events used in the study of detector acceptances and angular distributions of the various B decay modes investigated.

3.5.4 CABS

The large number of modes considered in this analysis, 60 in all, would traditionally require the user to write many thousands of lines of FORTRAN code to implement fully all the reconstructed events. Nobu Katayama has written a simple scripting language for CLEO II called CABS [41]. The language reduces the number of lines a programmer writes to a few lines of easily readable code. The small number of lines also make it possible to quickly and reliably implement changes in reconstructing and analyzing data.

CABS takes advantage of an object oriented approach to programming. All particle definitions are considered as objects which are endowed with quantities, classes, tagged to the particular instance of the particle-decay definition. The tagged quantities are internally defined kinematic variables or can defined by the user. Furthermore, objects can be used to construct other objects while retaining all previously defined properties. Another feature of CABS is the elimination of user written DO loops since this is handled automatically by the high-level design philosophy. Al that is required of the user is to define the properties of the charged tracks and showers and combines the objects with other objects to form composite particles.

CHAPTER 4
ANALYSIS PROCEDURE

Introduction

The objective of this analysis is to measure various properties of B mesons by exclusive reconstruction of their decays. To do so, we first defined the selection criteria for each of the final decay products, kaons, pions and photons, combined these into candidates, selected from among these by imposing additional requirements, defined further candidates until we obtained a fully reconstructed B meson candidate. Further selection criteria are then imposed on the B candidate and their properties are examined by measuring event yields in distributions of particular interest. In this chapter, we will describe the data sample used, the set of global event requirements imposed and the selection criteria and methods used in reconstructing the B mesons. Also, the performance of the selection criteria will be discussed in some detail, with emphasis on the efficiency and amount of background removed by imposing the various selection requirements.

4.1 Data Sample

The data used in this analysis were collected by the CLEO II detector at the CESR e^+e^- storage ring beginning in November of 1990 and ending in January of 1993. During this period various changes were made to the CESR accelerator and CLEO II detector. These included improvements to data acquisition by the installation of the DAQ90 system and LVL3 software triggers during the Summer of 1991, replacing the gas in the PT with di-methyl ether in April of 1992 and replacing the synchrotron RF cavities with new MARK III cavities in the Fall of 1992. These changes affected detector acceptance and resulted in an increase to the total number of events in our data sample. The changes did not significantly affect the quality of the data and did not require separate analysis procedure for different data sets.

The data sample used consisted of a total integrated luminosity of 2.04 fb^{-1} on the $\Upsilon(4s)$ resonance and 0.97 fb^{-1} off resonance. The entire sample was divide into seven data sets, labeled the 4s2 through 4s8, each corresponds to several months of data-taking. The luminosity times $B\bar{B}$ cross-section for this sample gives a total of 2.2×10^6 $B\bar{B}$ events. The off resonance sample was taken approximately 26 MeV below the $\Upsilon(4S)$ and was used for continuum background studies.

The data processed by the off-line event reconstruction programs were divided into various data type classifications. These included: QED (Bhabhas, μ pairs and radiative Bhabhas), $e^+e^- \to \tau^+\tau^-$, two photon, hadronic and various classes of junk events, *i.e.,* beam-wall and beam-gas interactions. The QED sample was used primarily for detector calibration since these processes are well understood theoretically. The hadronic sample used was extracted from the full data set by imposing a set of selection criteria designed to retain hadronic events while eliminating QED, junk and other non $B\bar{B}$ events.

4.2 Global Event Requirements

The hadronic sample was defined by events which passed the following requirements: the number of charged tracks in the event greater than or equal to four, the total energy deposited in the calorimeter less than 65% of the center of mass energy (E_{cm}) or the highest energy shower must have an energy less than 60% of E_{cm} , the visible energy (computed from showers and charged tracks) greater than 20% of E_{cm} and the vertex position of the event was required to be within 2 cm (5 cm) in the direction perpendicular (parallel) to the beam with respect to the nominal run averaged collision point. These requirements eliminated more than 99% of all Bhabhas while retaining more than 99% of the $B\bar{B}$ and 95% of generic $udsc$ and $c\bar{c}$ hadronic continuum events.

The topological characteristic or shape of the event was also used in the selection criteria. We imposed two global event shape cuts to help separate continuum from $B\bar{B}$ events, the variable R_2, or the ratio of the 2^{nd} to 0^{th} Fox-Wolfram moments, and the event sphericity angle. These two cuts are correlated and together eliminated about 35% of the continuum while retaining 96% of the $B\bar{B}$ events.

The R_2 [42] variable is defined as the ratio $R_2 = H_2/H_0$ where

$$H_l \equiv \sum_{i,j} \frac{|\vec{p}_i||\vec{p}_j|}{E^2} P_l(\cos\phi_{ij}). \tag{4.1}$$

The indices ij run over all tracks in the event, ϕ_{ij} is the angle between the tracks i and j, P_l is the l^{th} Legendre polynomial and E is the total energy of the event. The numerator in the ratio H_2/H_0 is proportional to $\frac{1}{2}(3\cos^2(\phi_{ij}) - 1)$ while the denominator is used to normalize H_l. A value close to 1 is obtained when the event is jet-like. For events that are distributed isotropically the value tends to 0. Since we were interested in $B\bar{B}$ decays, which decay isotropically, we placed a cut on R_2 which accepted events with a value of 0.5 or less. In Figure

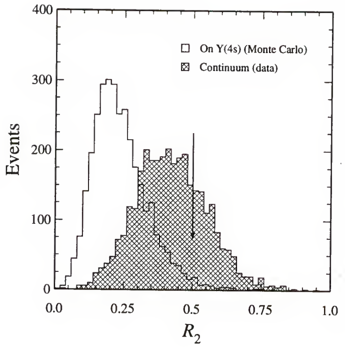

Figure 4.1 R_2 plotted for continuum and $B\bar{B}$ Monte Carlo.

4.1 a plot of R_2 for continuum and $B\bar{B}$ events is shown. The requirement on R_2 alone is seen to eliminates a substantial amount of continuum while retaining most of the $B\bar{B}$ events.

A second global event shape requirement made was on the cosine of the sphericity angle. The sphericity angle (Θ_f) is defined as the angle between the major sphericity axis calculated using all tracks consistent with a B candidate and the major sphericity axis calculated using the remaining tracks in the event. The major sphericity axis, or jet axis, is calculated by diagonalizing the momentum tensor T_{ij} defined as

$$T_{ij,\ i \neq j} = -\sum_{n=1}^{N} p_i(n) p_j(n)$$

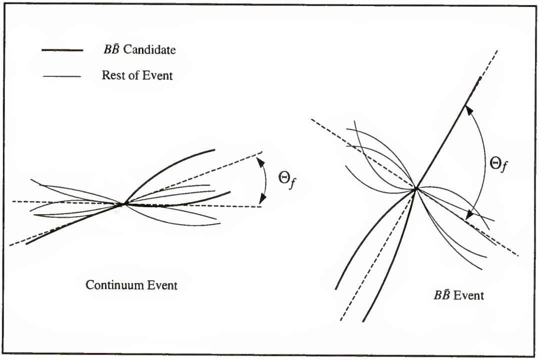

Figure 4.2 Diagram of the sphericity axis superimposed on typical events.

$$T_{ii} = \sum_{n=1}^{N} \sum_{j \neq i} p_j^2(n) \tag{4.2}$$

where $p_i(n)$ and $p_j(n)$ are the i^{th} and j^{th} component of the momentum vector and the sum runs over all applicable tracks. The major axis corresponds to the smallest eigenvalue.

A pictorial description of the sphericity angle is shown in Figure 4.2 with the major sphericity axis superimposed on a typical continuum and a low multiplicity $B\bar{B}$ event. The figure illustrates the tendency of continuum events to cluster near $\cos(\Theta_f) = \pm 1$, while all values of $\cos(\Theta_f)$ are equally likely for $B\bar{B}$ events since the angle Θ_f can assume any value from 0 to 2π. The major

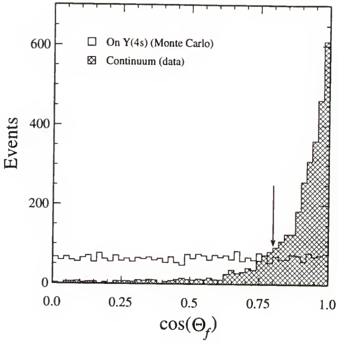

Figure 4.3 The $\cos(\Theta_f)$ distribution in a continuum and a $B\bar{B}$ sample.

sphericity axes are indicated by dashed lines, the heavy solid lines are the charged tracks which combine to form a B meson and the light solid lines are the tracks that make up the rest of the event.

In this analysis a cut on the $|\cos(\Theta_f)|$ was imposed on each event after it passed all B candidate requirements. In modes with a prominent signal the cut was determined by maximizing the signal to noise. In modes where a signal was not evident the value of the cut used was taken from a mode with similar kinematics and multiplicity. The cut thus varied mode by mode with the tightest restriction, $|\cos(\Theta_f)| \leq 0.7$, imposed on B decays to a a_1 plus a charmed meson and the loosest cut, $|\cos(\Theta_f)| \leq 0.9$, on B decays to a D^* plus a single pion. In Figure 4.3 a plot of the $\cos(\Theta_f)$ distribution for

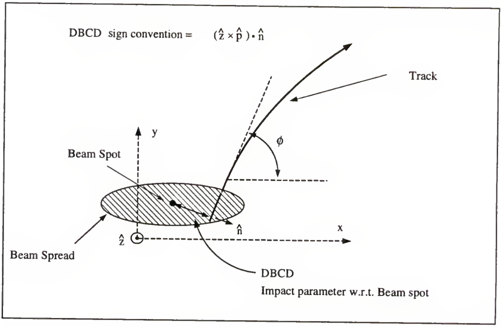

Figure 4.4 Diagram of signed impact parameter with respect to beam-spot.

continuum and $B\bar{B}$ Monte Carlo events illustrates the discrimination power of this variable. The plot shows that a cut of $|\cos(\Theta_f)| \leq 0.8$ eliminates 80% of continuum events and retains 80% of the $B\bar{B}$ events.

4.3 Charged Track Selection

The various requirements imposed on charged track candidates not only provided good quality tracks originating at the primary vertex but also helped in determining whether the particular track was a kaon or a pion. The latter was accomplished by using the dE/dx particle ID system described in Chapter 3.

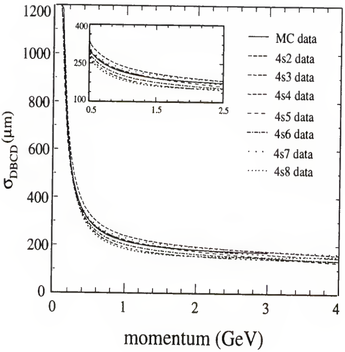

Figure 4.5 DBCD plotted vs. momenta for 4s2-4s8 and Monte Carlo data.

To insure that tracks originated from the primary vertex a cut on the momentum dependent impact parameter with respect to beam-spot (DBCD) was imposed (The diagram in Figure 4.4 defines the variable DBCD). The cut used accepted tracks with an impact parameter less than $4\sigma_{\mathrm{DBCD}}$ for tracks with momentum above 250 MeV. For tracks with momentum less than 250 MeV the requirement was changed to $7\sigma_{\mathrm{DBCD}}$. The quantity σ_{DBCD} is the spread in the measured impact parameter with respect to beam spot measured for a large sample of charged tracks. The spread depends on the momentum of the tracks as well as the angle ϕ they make with the x axis. The momentum dependence of the spread, for each of the data sets and a Monte Carlo sample, is shown in Figure 4.5. A detailed analysis is presented in Appendix A.

The dE/dx particle identification system was used to establish whether a particular track was a kaon or a pion. First, tracks were required to have more than ten central drift chamber hits to insure that energy loss information was available. The K/π candidate was then selected if its energy loss measurement differed from that expected for a K/π hypothesis by less than 3σ.† Since low momentum tracks do not travel far into the central drift chamber all particle ID requirements were suspended if the track's momentum was less than 250 MeV. These tracks were only used as slow pion candidates in $D^{*\pm}$ reconstruction.

4.4 Photon Selection

Photons were selected from clusters of cells in the barrel region of the crystal calorimeter with an energy greater than 30 MeV. Because of the degradation in energy resolution in other regions of the detector, the energy requirement for the cluster in the endcaps was increased to 50 MeV and clusters which fell in the endcap-barrel overlap region, between 32° and 36°, were rejected altogether. If the cluster matched a charged track's projection into the calorimeter the cluster was rejected as a photon candidate. To form a match, the track's projection was required to be within 8 cm of at least one cell in the cluster.

To distinguish electromagnetic showers from hadronic showers we used the shower's lateral shape distribution. Electromagnetic showers deposit their energy in an narrow region around the central crystal and tend not to spread as hadronic showers do. A quantity E_9/E_{25} is defined, for each candidate cluster,

† σ is the rms resolution of the expected dE/dx energy loss for the K/π hypothesis.

as the sum of energy of the block of 9 crystals divided by the block of 25 crystals both centered on the central crystal. The quantity depends on the energy and polar angle of the cluster and is close to one for electromagnetic showers. This quantity was evaluated for each candidate shower and compared with the value expected for 99% of all electromagnetic showers. Since candidate shower were used only to reconstruct neutral pions or etas, we used a slightly modified version of E_9/E_{25}, referred to as E_9/E_{25} unfolded. This quantity allows for the possibility of merged showers in high momentum two photon candidate by using not only the crystals assigned to the shower but also a fraction of the shared crystals.

4.5 Particle Reconstruction

We now turn to describing the criteria used to reconstruct the rest of the particles which will ultimately be used in reconstructing the B meson candidates. The reconstruction method used is rather simple: a chosen particle candidate is made by combining the 4-momenta of its decay products. A set of quantities are then calculated for the composite particle, constraints are imposed, and the selected particle candidate is stored for use in reconstructing the B or other particles.

4.5.1 Light Neutral and Charged Mesons

Neutral pion candidates were first formed by combining two photons and requiring that the invariant mass of the combination be within 2.5σ of the fitted neutral pion mass. The neutral pion mass distributions are asymmetric and the asymmetry, the resolution of the asymmetric Gaussian and the fitted

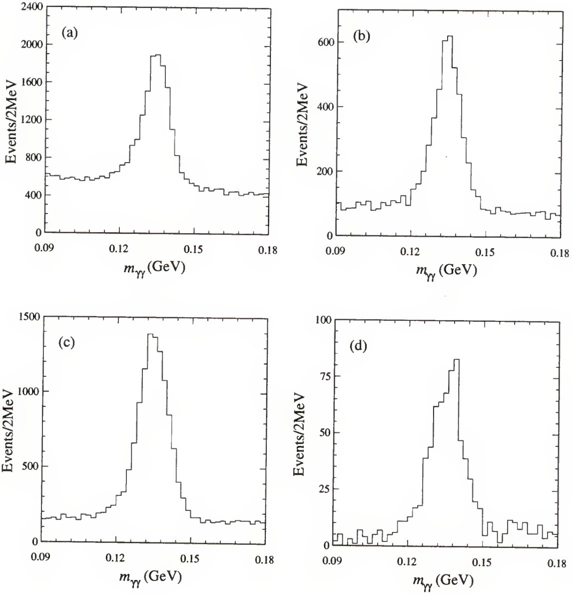

Figure 4.6 Two photon invariant mass distributions at different momenta.

The invariant mass for the π^0 candidates with momenta between (a) 500 and 600 MeV, (b) between 900 and 1000 MeV, (c) between 1.0 and 1.5 and (d) between 2.0 and 2.5 GeV.

Table 4.1

Neutral pion fitted mass, σ_L, σ_R vs. π^0 momenta

p_{π^0} (GeV)	m_{π^0} (MeV)	σ_L (MeV)	σ_R (MeV)
$0.0-0.4$	134.4	6.22	3.96
$0.4-0.8$	134.1	6.13	4.29
$0.8-1.2$	133.8	6.09	4.87
$1.2-1.6$	133.7	6.03	5.66
$1.6-2.0$	134.0	7.25	6.61
$2.0-2.4$	133.5	10.14	8.00

central value vary slightly as a function of momenta, (the momentum dependence of these quantities are shown in Figure 4.6 where the invariant mass is plotted in four different momentum bins). To compensate for this we varied the mean, σ_L and σ_R as a function of momenta as shown in Table 4.1. Candidates with momentum less than 250 MeV were rejected if one or both of their photons came from the endcap or overlap region. Finally, the neutral pions were kinematically fit with their masses constrained to the known pion mass and a χ^2 cut of 12.0 was imposed.

Etas decay to two photons about 39% of the time. The two remaining channels with relatively large branching fraction, the $3\pi^0$ and $\pi^+\pi^-\pi^0$, modes were not used. The $3\pi^0$ mode contained too many possible 2γ combinations to be useful, while the $\pi^+\pi^-\pi^0$ mode provided little additional information in determining $\bar{B}^0 \to D^0\eta$ or $\bar{B}^0 \to D^{*0}\eta$ branching fractions due to large background levels.

The $\eta \to \gamma\gamma$ candidates were selected from two photon combinations that had at least one of the photons in the barrel region. The candidates were

Table 4.2

Decay modes and resolutions for the D and D^* candidates

Decay Mode	Resoultion (MeV)
$D^0 \to K^-\pi^+$	$\sigma_{m_{D^0}} = 9.0$
$D^0 \to K^-\pi^+\pi^0$	$\sigma_{m_{D^0}} = 13.0$
$D^0 \to K^-\pi^+\pi^-\pi^+$	$\sigma_{m_{D^0}} = 8.1$
$D^+ \to K^-\pi^+\pi^+$	$\sigma_{m_{D^+}} = 8.3$
$D^{*0} \to D^0\pi^0$	$\sigma_{(m_{D^{*0}}-m_{D^0})} = 0.8$
$D^{*+} \to D^0\pi^+$	$\sigma_{(m_{D^{*+}}-m_{D^0})} = 1.1$

required to have an invariant mass within 30 MeV of the PDG value [2]. Candidates with asymmetric decay, *i.e.*, $|\cos\theta_d| > 0.85$ were rejected. The decay angle θ_d is defined as the angle between the direction of one of the photons and the direction of the eta in the lab frame as measured in the rest frame of the eta. Real etas have a flat $\cos\theta_d$ distribution while random 2γ combinations, that happen to fall within the eta mass cut, are strongly peaked in the region near $\cos\theta_d = 1$. This cut eliminates background from fake etas but only reduces the sample of true etas by 15%. Once candidates passed all requirements they were kinematically fit with their masses constrained to the PDG η mass value and a $\chi^2 \leq 12$ was imposed.

The rest of the light mesons were reconstructed in the following decay modes

$\rho \to \pi\pi$

The mass was constrained to be within one full decay width (150 MeV) of the nominal ρ mass.

$\omega \to \pi^+\pi^-\pi^0$

The mass was required to be within 30 MeV of the nominal ω mass.

$\eta' \to \eta\pi^+\pi^-$

The mass of each candidate η' was required to be within 30 MeV of the nominal η' mass. The $\eta' \to \rho^0\gamma$ mode was examined but yielded no additional information in determining B branching fractions was obtained due to increase in backgrounds without providing a signal in the event yield. Only the $\eta' \to \eta\pi^+\pi^-$ mode with $\eta \to \gamma\gamma$ was used.

$a_1 \to \rho\pi$

The a_1 meson has a very large and poorly determined decay width. Its mass was constrained to lie between 1.0 GeV and 1.6 GeV. The mass of the ρ was constrained in all a_1 candidates as described.

4.5.2 Charmed Meson Selection

Unlike the light mesons, pseudoscalar charmed mesons can decay through a large number of channels each with a relatively small branching fractions. A large number of these modes have multiple neutral pions and or neutral kaons, which have low reconstruction efficiencies. The losses incurred when fully reconstructing a D makes most of these modes unavailable hence only three modes were used in reconstructing D^0s and one mode for the D^+s.† The relevant modes used are listed in Table 4.2 together with their measured rms

† Charge conjugate states are implied if not indicated explicitly.

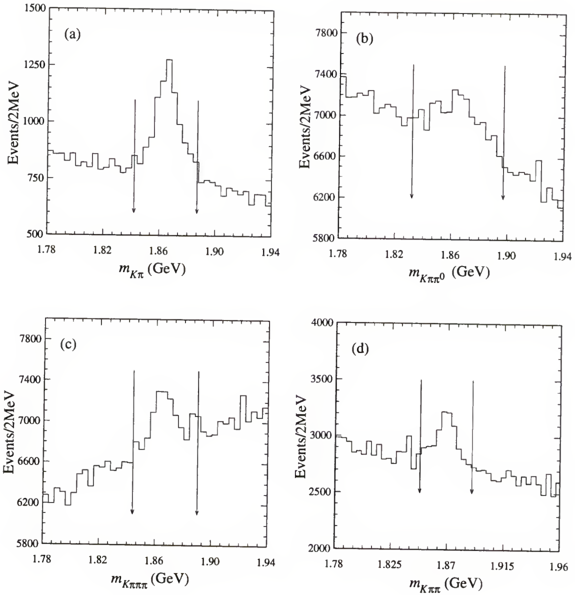

Figure 4.7 Invariant mass distributions of $Kn\pi$ combinations.

In (a) the invariant mass distribution of the $K^-\pi+$ combination, in (b) the $K^-\pi^+\pi^0$ combination, in (c) the $K^-\pi^+\pi^-\pi^+$ combination and in (d) the $K^+\pi^-\pi^-$ combination.

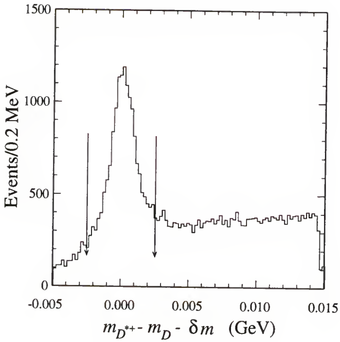

Figure 4.8 D^{*+}, D^0 mass difference plot.

mass resolutions, σ_{m_D} [43]. The invariant mass distributions for the four decay modes used are shown in Figure 4.7. Each plot consist of a subsample of the dataset, the 4s6, and is plotted for candidates whose momenta lie between 2.0 GeV and 2.5 GeV. The arrows in the figure show the bounds of the $2.5\sigma_{m_D}$ mass requirement imposed on all candidates.

For B modes which decay to a D^*, we took advantage of the excellent resolution on the $m_{D^*} - m_D$ mass difference. In D^* decays the small amount of available phase space leads to a sharp, narrow peak in the $m_{D^*} - m_D$ distribution. The sharp peak was exploited in reconstructing the $B \to D^*$ modes by eliminating non D^* combinations that were outside the $m_{D^*} - m_D$ mass region. An example of the $m_{D^*} - m_D$ mass resolution is shown in Figure 4.8

with the 2.5σ cut indicated by the arrows. The D^0 was reconstructed in the $D^0 \to K^-\pi^+$ decay mode.

For D^* candidates we first required the mass of the D^0 to be within 2.5σ of its measured resolution and then imposed the $m_{D^*} - m_D$ requirement. As with pseudoscalar decays we only considered charmed vector meson decay modes which had both large branching fractions and low backgrounds. The decay modes and their measured rms resolutions are also listed in Table 4.2 [43].

4.6 B Mesons Selection

All the necessary ingredients are now in place to fully reconstruct the B mesons. The non color-suppressed decay modes used were

$$\begin{array}{lll} \bar{B}^0 \to D^+\pi^- & \bar{B}^0 \to D^+\rho^- & \bar{B}^0 \to D^+a_1^- \\ \bar{B}^0 \to D^{*+}\pi^- & \bar{B}^0 \to D^{*+}\rho^- & \bar{B}^0 \to D^{*+}a_1^- \\ B^- \to D^0\pi^- & B^- \to D^0\rho^- & B^- \to D^0 a_1^- \\ B^- \to D^{*0}\pi^- & B^- \to D^{*0}\rho^- & B^- \to D^{*0}a_1^- \end{array} \tag{4.3}$$

the color-suppressed modes were

$$\begin{array}{lllll} \bar{B}^0 \to D^0\pi^0 & \bar{B}^0 \to D^0\eta & \bar{B}^0 \to D^0\eta' & \bar{B}^0 \to D^0\rho^0 & \bar{B}^0 \to D^0\omega \\ \bar{B}^0 \to D^{*0}\pi^0 & \bar{B}^0 \to D^{*0}\eta & \bar{B}^0 \to D^{*0}\eta' & \bar{B}^0 \to D^{*0}\rho^0 & \bar{B}^0 \to D^{*0}\omega. \end{array} \tag{4.4}$$

For each mode various physical properties of the fully reconstructed B mesons were analyzed to determine branching fractions and polarization states. The results and conclusions will be discussed in Chapter 6.

To calculate the branching fraction we need to determine the number of fully reconstructed B mesons in our sample. To do so we used the beam constrained mass ($\mathrm{M_{BC}}$) defined as

$$\mathrm{M_{BC}} = \sqrt{E_{beam} - \left(\sum_i p_i\right)^2}, \tag{4.5}$$

where p_i are the reconstructed momenta of the decay products of the B and E_{beam} is the energy of the e^+ e^- beam. The $\mathrm{M_{BC}}$ distribution has a resolution an order of magnitude better than the invariant B mass distribution and was used to determine event yields. The resolution of this variable is dominated by the spread in the beam energy which is approximately 3 MeV at the $\Upsilon(4S)$. The small width gives a sharply peaked $\mathrm{M_{BC}}$ distribution, at the B mass and was thus easy to fit with a signal plus background shape.

The criteria used to select the B meson candidates varied with the decay mode used. Two quantities, however, were used in selecting all candidates, the B meson's polar angle θ_B and the difference between its reconstructed energy and the energy of the beam,

$$\Delta\mathrm{E} = E_{beam} - E_{reconstructed}. \tag{4.6}$$

Since other selection criteria are mode dependent we defer their discussion to later sections.

The cut imposed on the polar angle was $|\cos(\theta_B)| \leq 0.95$. It takes advantage of the spatial distribution resulting from angular momenta conservation in the decay of $\Upsilon(4S)$. The $\Upsilon(4S)$ is produced in e^+ e^- collisions through a virtual photon with $J = 1, M = \pm 1$. Its decay to two spin zero objects is determined by angular momentum conservation forcing the orbital distribution to follows a $\sin^2(\theta_B)$ form.

The ΔE distribution is centered on zero with a width ($\sigma_{\Delta\mathrm{E}}$) determined by the energy resolution of the individual particles in the final state. The ΔE widths were measured for each exclusive mode and found to vary from 14 to 44 MeV. These measurements were performed on tagged Monte Carlo data

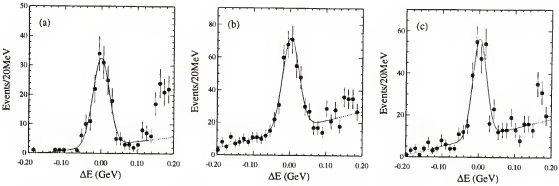

Figure 4.9 ΔE distributions of the $B^- \to D^0\pi^-$ modes.

In (a) the $D^0 \to K^-\pi^+$ mode, in (b) the $D^0 \to K^-\pi^+\pi^0$ mode and in (c) the $D^0 \to K^-\pi^+\pi^-\pi^+$ mode.

which was found to be consistent with measurements performed on the data sample. In Figure 4.9 the ΔE distributions for all three $B^- \to D^0\pi^-$ modes are shown. Each ΔE distribution was fit to a Gaussian plus a straight line. These measured ΔE resolutions were then compared with fits to Monte Carlo data and were found to differ by no more than $1\sigma_{\Delta \mathrm{E}}$, where $\sigma_{\Delta \mathrm{E}}$ is the statistical error of the resolution measurements.

A mode dependent ΔE cut of $2.5\sigma_{\Delta \mathrm{E}}$ was imposed on each candidate to discriminate against background events resulting from poorly reconstructed B and or other B decays which differ by one or more pion.† In B decays where a ρ^- is produced the resolution of ΔE is affected by the momentum of the neutral pion produced from the decay of the ρ. This dependence is parameterized by the helicity angle Θ_h (defined below) and the cut on ΔE varied as a function of Θ_h for these modes.

The large number of particles in each event sometimes leads to multiple B candidates per mode that pass all the selection criteria. In these instances, the

† This is discussed in greater detail in Chapter 5.

Table 4.3

Selection criteria for non color-suppressed $B \to D^{(*)}\pi$ decays

B Channel	D Sub-channel	$\lvert\cos(\Theta_f)\rvert$	$\lvert\Delta E\rvert$ (GeV)
$D^0\pi^-$	$K^-\pi^+$	≤ 0.8	≤ 0.055
	$K^-\pi^+\pi^0$		≤ 0.065
	$K^-\pi^+\pi^-\pi^+$		≤ 0.051
$D^+\pi^-$	$K^-\pi^+\pi^+$	≤ 0.8	≤ 0.051
$D^{*0}\pi^-$	$K^-\pi^+$	≤ 0.9	≤ 0.050
	$K^-\pi^+\pi^0$		≤ 0.068
	$K^-\pi^+\pi^-\pi^+$		≤ 0.047
$D^{*+}\pi^-$	$K^-\pi^+$	≤ 0.9	≤ 0.050
	$K^-\pi^+\pi^0$		≤ 0.062
	$K^-\pi^+\pi^-\pi^+$		≤ 0.045

Table 4.4

Selection criteria for non color-suppressed $B \to D^{(*)}\rho$ decays

B Channel	D Sub-channel	$\lvert\cos(\Theta_f)\rvert$	$\lvert\Delta E\rvert$ (GeV)
$D^0\rho^-$	$K^-\pi^+$	≤ 0.8	$\leq (0.025 \cdot \cos(\Theta_h) + 0.070)$
	$K^-\pi^+\pi^0$		$\leq (0.025 \cdot \cos(\Theta_h) + 0.079)$
	$K^-\pi^+\pi^-\pi^+$		$\leq (0.025 \cdot \cos(\Theta_h) + 0.067)$
$D^+\rho^-$	$K^-\pi^+\pi^+$	≤ 0.8	$\leq (0.025 \cdot \cos(\Theta_h) + 0.070)$
$D^{*0}\rho^-$	$K^-\pi^+$	≤ 0.8	$\leq (0.025 \cdot \cos(\Theta_h) + 0.078)$
	$K^-\pi^+\pi^0$		$\leq (0.025 \cdot \cos(\Theta_h) + 0.089)$
	$K^-\pi^+\pi^-\pi^+$		$\leq (0.025 \cdot \cos(\Theta_h) + 0.072)$
$D^{*+}\rho^-$	$K^-\pi^+$	≤ 0.8	$\leq (0.025 \cdot \cos(\Theta_h) + 0.079)$
	$K^-\pi^+\pi^0$		$\leq (0.025 \cdot \cos(\Theta_h) + 0.083)$
	$K^-\pi^+\pi^-\pi^+$		$\leq (0.025 \cdot \cos(\Theta_h) + 0.076)$

candidate with the "best" (*i.e.*, smallest) ΔE value was chosen. This procedure of picking the candidate with the best ΔE picks the correct candidate 86.2% of the time. The success rate was determined by comparing tagged and untagged Monte Carlo yields in the $\bar{B}^0 \to D^0\pi^0$ with $D^0 \to K^-\pi^+$. This procedure also tends to bias the sample of selected B to those with ΔE values close to zero. However, the results are unaffected since the Monte Carlo simulations correctly predict the loss in efficiency for this choice of the "best" B candidate.

The cuts used vary depending not only on the B decay channel but also the D subchannel considered. In order to list the differences in a systematic way we divide the modes into color-suppressed and non color-suppressed modes and then further divide the non color-suppressed modes into modes containing one, two and three pion light mesons. The various ΔE and global sphericity angle cuts are discussed in the following subsections.

4.6.1 Non Color-Suppressed Modes

$B \to D^{(*)}\pi$ modes. In B modes that decay to a charmed meson plus a single pion we used the cuts described above with no additional requirements imposed. The values of the sphericity angle and ΔE cuts are listed in Table 4.3. The values listed in the table correspond to 2.5 times the measured $\sigma_{\Delta \mathrm{E}}$ resolutions.

$B \to D^{(*)}\rho$ modes. In these modes, we employed a cut designed to take advantage of the spatial distribution of the ρ's decay products. The spatial distribution is best parameterized by a variable which we refer to as the helicity angle Θ_h. In $\rho^- \to \pi^0\pi^-$ decays, it is defined as the angle between the direction

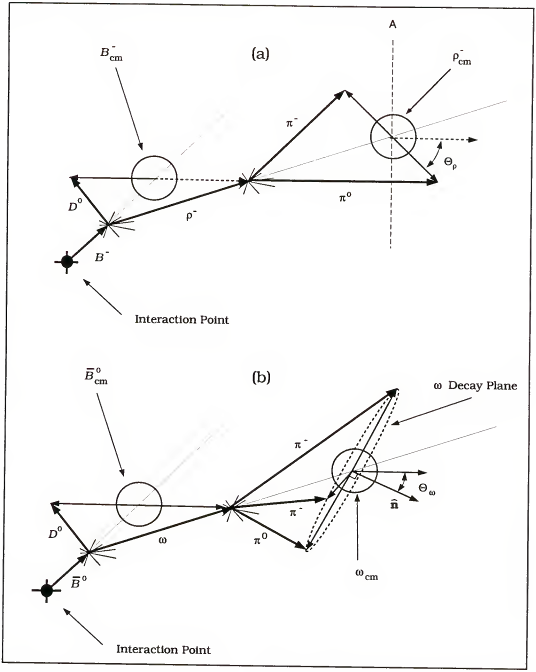

Figure 4.10 Diagram of helicity angle definitions.

The helicity angle Θ_h ($h = \rho, \omega$) is shown for the decay modes (a) $B^- \to D^0\rho^-$ and (b) $\bar{B}^0 \to D^0\omega$.

of the π^0, in the ρ^-'s rest frame, and the direction of the ρ^- in the B candidate's rest frame (see Figure 4.10). As an example, we take the decay $B^- \to D^0\rho^-$. The ρ^- is produced longitudinally polarized along its direction of motion in the B 's rest frame. Simple angular momentum conservation shows that the decay of a $|1,0\rangle$ object to two spinless pions is governed by a $\cos^2(\Theta_h)$ distribution. For B decays to a ρ plus another vector particle, a D^*, the effectiveness of a cut based on these arguments is somewhat compromised since now the initial total angular momentum state of the ρ^- is undetermined. We could require that both the D^* and the ρ have identical helicity distributions, but this reduces the acceptance without much improvement in the signal to noise in the already clean modes where the $D^* - D$ mass difference cut can be used.

The helicity angle cuts used depended not only on the B decay channel but also on the D subchannel considered. In the decay $B^- \to D^0\rho^-$, a cut of $|\cos(\Theta_h)| \geq 0.4$ was used for all three D^0 subchannels. For the $D^0 \to K^-\pi^+\pi^0$ mode a large amount of background was eliminated by discarding B candidates with a soft π^0 produced in the ρ^- decay. This was accomplished by excluding candidates with neutral pions in the backward region of the ρ decay plane (plane A in Figure 4.10 (a)) thus a cut $\cos(\Theta_h) \geq 0.4$ was imposed as a consistency check. For the $\bar{B}^0 \to D^+\rho^-$ channel a $|\cos(\Theta_h)| \geq 0.4$ cut was also employed.

The ΔE and Θ_f angle cuts used for the $B \to D^{(*)}\rho^-$ modes are listed in Table 4.4. The helicity angle dependence of the ΔE resolution discussed earlier is included in the ΔE cut column. The helicity angle dependence of the ΔE resolution was found by measuring the ΔE resolutions at different $\cos(\Theta_h)$ values in Monte Carlo. The plots where then fit to straight lines. The

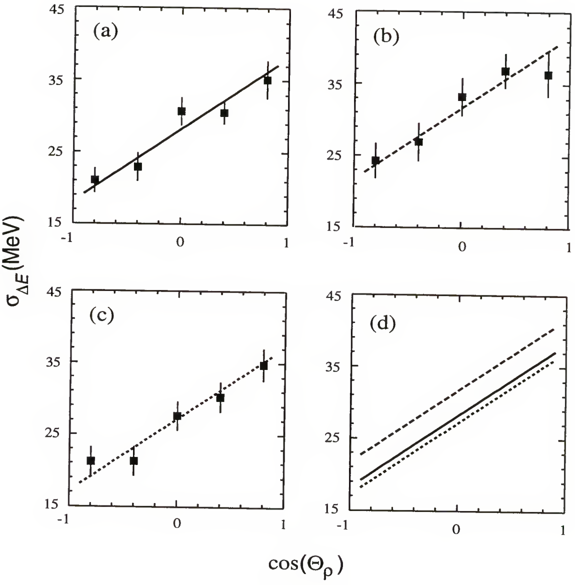

Figure 4.11 Plots of helicity as a function of ΔE.

ΔE resolution as a function of the ρ^- $\cos(\Theta_h)$ for the decay mode $B^- \to D^0\rho^-$ with (a) $D^0 \to K^-\pi^+$, (b) $D^0 \to K^-\pi^+\pi^0$ and (c) $D^0 \to K^-\pi^+\pi^-\pi^+$. The fits for all three modes are shown in Figure (d).

Table 4.5

Selection criteria for non color-suppressed $B \to D^{(*)}a_1$ decays

B Channel	D Sub-channel	$\lvert\cos(\Theta_f)\rvert$	$\sigma_{\Delta E}$ (GeV)
$D^0a_1^-$	$K^-\pi^+$	≤ 0.7	0.042
	$K^-\pi^+\pi^0$		0.056
	$K^-\pi^+\pi^-\pi^+$		0.043
$D^+a_1^-$	$K^-\pi^+\pi^+$	≤ 0.7	0.037
$D^{*0}a_1^-$	$K^-\pi^+$	≤ 0.7	0.044
	$K^-\pi^+\pi^0$		0.067
	$K^-\pi^+\pi^-\pi^+$		0.036
$D^{*+}a_1^-$	$K^-\pi^+$	≤ 0.7	0.040
	$K^-\pi^+\pi^0$		0.055
	$K^-\pi^+\pi^-\pi^+$		0.036

fitted $\cos(\Theta_h)$ vs. $\sigma_{\Delta E}$ distributions are shown in Figure 4.11 for the three D^0 subchannels in $B^- \to D^0\rho^-$ decays.

<u>$B \to D^{(*)}a_1$ modes.</u> As in B decays to D plus a single pion, no additional cuts were imposed on modes with a a_1 in the final state. The dominant decay modes of the a_1, the $\rho\pi$ mode, does not allow the use of a helicity type cut since the initial angular momentum state of the ρ is indeterminate and thus no useful spatial angular distribution is available. The broad a_1 resonance together with the large number of particles in the final also results in particularly large combinatoric background which hampered the extraction of signal events yields in the $B^- \to D^0a_1^-$ and $\bar{B}^0 \to D^+a_1^-$ channels.

4.6.2 Color-Suppressed Modes

The color-suppressed modes were treated in a similar way to the modes discussed above. The difference mainly lay in our inability to verify that the Monte Carlo predicted values used to select and refine the cuts matched the data. For example, we used the ΔE resolutions obtained from Monte Carlo only for the $D^0 \to K^-\pi^+$ mode in all color-suppressed modes. For the two remaining D^0 decay modes, we took the values obtained for $D^0 \to K^-\pi^+$ mode and scaled that by a factor obtained from a similar non color-suppressed mode where the ΔE resolution could be checked in data. This is done for all but the $\bar{B}^0 \to D^0\pi^0$ mode since the resolution of the $D^0 \to K^-\pi^+$ mode is already 44 MeV.

Pseudoscalar light mesons. As with the non color-suppressed light pseudoscalar modes, the candidates in these modes were selected without additional cuts. Only the standard ΔE and sphericity cuts were applied. The values used for each mode are listed in Table 4.6. The |ΔE| cut entries in the table reflects the 2.5 times the ΔE resolution.

Vector light mesons. Four color-suppressed modes contain a light vector meson in the B decay product. Two of these, the $\bar{B}^0 \to D^{*0}\rho^0$ and $\bar{B}^0 \to D^{*0}\omega$ are vector-vector decays in which complementary helicity requirements on both the D^{*0} and its vector partner were imposed. The helicity angle requirements, however, did not lead to any improvement in obtaining a signal in the event yield and were thus not used in the final analysis. The remaining two, the $\bar{B}^0 \to D^0\rho^0$ and $\bar{B}^0 \to D^0\omega$, have a spin 0 plus a spin one object in the final state so advantage was taken of the helicity requirement described earlier. In

Table 4.6

Selection criteria for color suppressed $B \to D^{(*)}P$ decays

B Channel	D Sub-channel	$\lvert\cos(\Theta_f)\rvert$	$\lvert\Delta E\rvert$ (GeV)
$D^0\pi^0$	$K^-\pi^+$	≤ 0.8	≤ 0.090
	$K^-\pi^+\pi^0$		≤ 0.090
	$K^-\pi^+\pi^-\pi^+$		≤ 0.090
$D^0\eta$	$K^-\pi^+$	≤ 0.8	≤ 0.074
	$K^-\pi^+\pi^0$		≤ 0.084
	$K^-\pi^+\pi^-\pi^+$		≤ 0.074
$D^0\eta'$	$K^-\pi^+$	≤ 0.8	≤ 0.049
	$K^-\pi^+\pi^0$		≤ 0.059
	$K^-\pi^+\pi^-\pi^+$		≤ 0.049
$D^{*0}\pi^0$	$K^-\pi^+$	≤ 0.9	≤ 0.090
	$K^-\pi^+\pi^0$		≤ 0.090
	$K^-\pi^+\pi^-\pi^+$		≤ 0.090
$D^{*0}\eta$	$K^-\pi^+$	≤ 0.9	≤ 0.060
	$K^-\pi^+\pi^0$		≤ 0.070
	$K^-\pi^+\pi^-\pi^+$		≤ 0.060
$D^{*0}\eta'$	$K^-\pi^+$	≤ 0.9	≤ 0.045
	$K^-\pi^+\pi^0$		≤ 0.055
	$K^-\pi^+\pi^-\pi^+$		≤ 0.045

Table 4.7

Selection criteria for color suppressed $B \to D^{(*)}V$ decays

B Channel	D Sub-channel	$\|\cos(\Theta_f)\|$	$\|\Delta E\|$ (GeV)
$D^0\rho^0$	$K^-\pi^+$	≤ 0.8	≤ 0.044
	$K^-\pi^+\pi^0$		≤ 0.054
	$K^-\pi^+\pi^-\pi^+$		≤ 0.044
$D^0\omega$	$K^-\pi^+$	≤ 0.8	≤ 0.050
	$K^-\pi^+\pi^0$		≤ 0.060
	$K^-\pi^+\pi^-\pi^+$		≤ 0.050
$D^{*0}\rho^0$	$K^-\pi^+$	≤ 0.9	≤ 0.041
	$K^-\pi^+\pi^0$		≤ 0.051
	$K^-\pi^+\pi^-\pi^+$		≤ 0.041
$D^{*0}\omega$	$K^-\pi^+$	≤ 0.9	≤ 0.054
	$K^-\pi^+\pi^0$		≤ 0.064
	$K^-\pi^+\pi^-\pi^+$		≤ 0.054

$\bar{B}^0 \to D^0\rho^0$, a cut on $|\cos(\Theta_h)| \geq 0.4$ was imposed. In $\bar{B}^0 \to D^0\omega$, the helicity angle definition is complicated because the ω decays to three spinless pions. The Θ_h angle is now defined as the angle between the normal to the ω decay plane and the ω direction in the B meson's rest frame (see Figure 4.10 (b)). Angular momentum conservation of the ω decaying to three spinless particles requires that the normal to the plane be distributed as a $\sin^2(\Theta_h)$. A cut on $|\sin(\Theta_h)| \leq 0.6$ was imposed on all candidates. The $\cos(\Theta_f)$ and ΔE cuts used are listed in Table 4.7.

CHAPTER 5
BACKGROUND STUDIES

Introduction

In this chapter we investigate the backgrounds which contribute to the $\mathrm{M_{BC}}$ spectra for the decay modes considered in the previous chapter. The $\mathrm{M_{BC}}$ background contributions can be separated into two components: continuum component and $B\bar{B}$ component. The continuum background is due to the large non-resonant fraction of the hadronic cross-section, approximately 75%, from direct $e^+e^- \to q\bar{q}$ production underneath the $\Upsilon(4S)$. The $B\bar{B}$ background component is a result of misreconstructing other $B\bar{B}$ decays. The relative contributions and the overall amount of background varies decay mode by decay mode depending primarily on the multiplicity of the B decay.

The background contributions to each $\mathrm{M_{BC}}$ distribution were not subtracted when establishing the event yield. Instead the backgrounds were parameterized by a function that fit the general characteristics of the overall background shape. Determination of the yield by fitting $\mathrm{M_{BC}}$ the spectrum to a background function plus a signal Gaussian assumes that the background does not peak significantly in the signal region and that the background function used adequately models the true background. To insure that these assumptions are valid we performed a detailed and careful study of the backgrounds, as discussed below.

5.1 Backgrounds in Non Color-Suppressed Modes

To simplify the analysis and the discussion that follows we divided the study into a study on the non-color suppressed modes and a study on the color-suppressed modes. The non color-suppressed mode were examined in greater detail since signals were obtained in all mode investigated. Determining the event yield in modes with prominent signals requires an accurate measure of the amount of background so that the systematic errors associated with the background shape could be established accurately. In the modes where signals are not observed, sensitivity to background systematics do not significantly affect the results since the errors here are dominated by uncertainties in statistics.

5.1.1 $B\bar{B}$ Backgrounds

Background contributions from other $B\bar{B}$ decays are impossible to completely isolate in real data since they are products of the same physical processes which produce signal events. To estimate this component we used Monte Carlo simulations, where complete control can be maintained over the production and decay mechanism. The Monte Carlo data set consisted of a sample of 1.95×10^6 $B\bar{B}$ events in which each B meson in the event was allowed to decay generically. The data set was separated into sub-samples where a particular B meson decay chain was removed. The removal of the decay chain here implies the removal of the complete B decay chain. This included all possible resonant substructure of the D meson. For example, in removing the $B^- \to D^0\pi^-$ with the $D^0 \to K^-\pi^+\pi^0$ decay, the $D^0 \to K^{*0}\pi^0$, the $K^{*-}\pi^+$ and the $K^-\rho^+$ substructure decays were removed as well. Each subsample, referred to as the "antiskim" sample, thus contained all known B meson decays except the decay chain of the particular mode whose background we investigated.

The B reconstruction algorithm described in Chapter 4 was then applied to each antiskim sample and the M_{BC} plots were made. Figures 5.1, 5.2 and 5.3 show the results for non color-suppressed modes with one, two and three pion light meson states respectively. Most of these plots show no significant enhancement in the signal region which cannot be accommodated by the background shape used.

For $B\bar{B}$ backgrounds to peak in the signal region two conditions must be met: the number and types of final state particles must match that of the B decay mode considered and the total reconstructed energy must satisfy the ΔE requirement. In Figure 5.2 (b-d) an excess is found in the signal region of the M_{BC} spectra. The background candidate B decay which meets these criteria is the $B^- \to D^{*0}\pi^-$ decay mode where the $D^{*0} \to D^0\gamma$. This mode can easily fake a $B^- \to D^0\rho^-$ if the ρ^- is misreconstructed by combining the fast π^- from the B decay with a low momentum π^0 picked randomly from the large number of two photon combinations possible in the event. The requirement that the energy be that of the B is met from the loss of the photon in the D^{*0} decay. This scenario was investigated by taking a sample of $B^- \to D^{*0}\pi^-$ Monte Carlo decays with the $D^{*0} \to D^0\gamma$ and reconstructing it as $D^0\rho^-$. The M_{BC} distributions are shown in Figure 5.4. The loose constraint on the ρ^- invariant mass can also conspire with $D^{*0} \to D^0\gamma$ decay to produce the broad enhancement in the $B^- \to D^0\rho^-$ signal region.

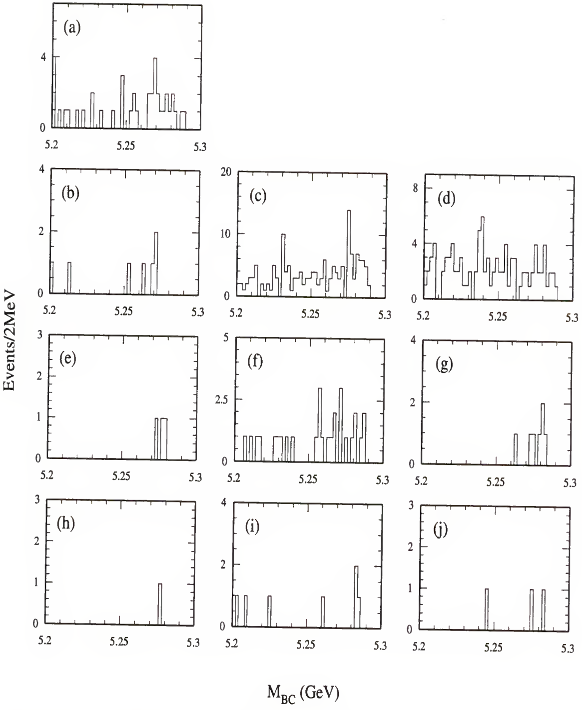

Figure 5.1 $B\bar{B}$ Monte Carlo M_{BC} spectrum, $B \to D^{(*)}\pi$.

In (a) the $B^0 \to D^+\pi^-$ in the D^+ decay mode $D^+ \to K^-\pi^+\pi^+$. In (b) through (d) the $B^- \to D^0\pi^-$ in the D^0 decay modes $K^-\pi^+$, $K^-\pi^+\pi^0$ and $K^-\pi^+\pi^-\pi^+$, respectively. In (e) through (g) the $B^- \to D^{*0}\pi^-$ in the D^0 decay modes $K^-\pi^+$, $K^-\pi^+\pi^0$ and $K^-\pi^+\pi^-\pi^+$. In (h) through (j) the $B^0 \to D^{*+}\pi^-$ in the D^0 decay modes $K^-\pi^+$, $K^-\pi^+\pi^0$ and $K^-\pi^+\pi^-\pi^+$.

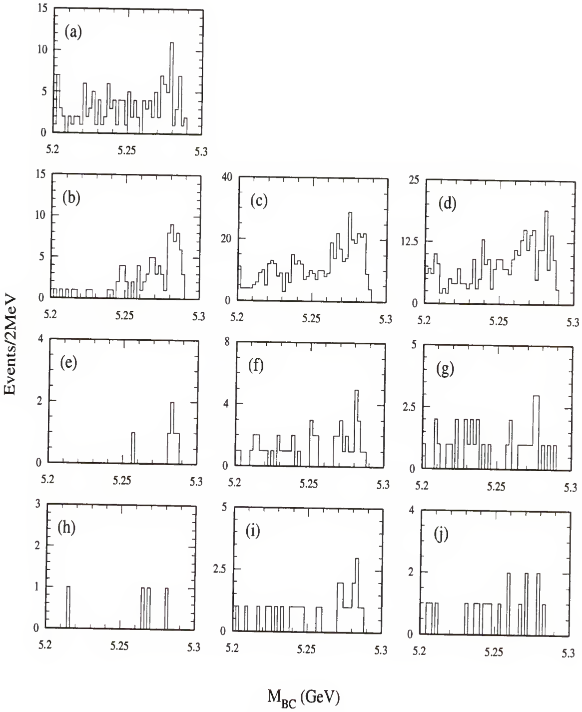

Figure 5.2 $B\bar{B}$ Monte Carlo M_{BC} spectrum, $B \to D^{(*)}\rho$.

In (a) the $B^0 \to D^+\rho^-$ in the D^+ decay mode $D^+ \to K^-\pi^+\pi^+$. In (b) through (d) the $B^- \to D^0\rho^-$ in the D^0 decay modes $K^-\pi^+$, $K^-\pi^+\pi^0$ and $K^-\pi^+\pi^-\pi^+$, respectively. In (e) through (g) the $B^- \to D^{*0}\rho^-$ in the D^0 decay modes $K^-\pi^+$, $K^-\pi^+\pi^0$ and $K^-\pi^+\pi^-\pi^+$. In (h) through (j) the $B^0 \to D^{*+}\rho^-$ in the D^0 decay modes $K^-\pi^+$, $K^-\pi^+\pi^0$ and $K^-\pi^+\pi^-\pi^+$.

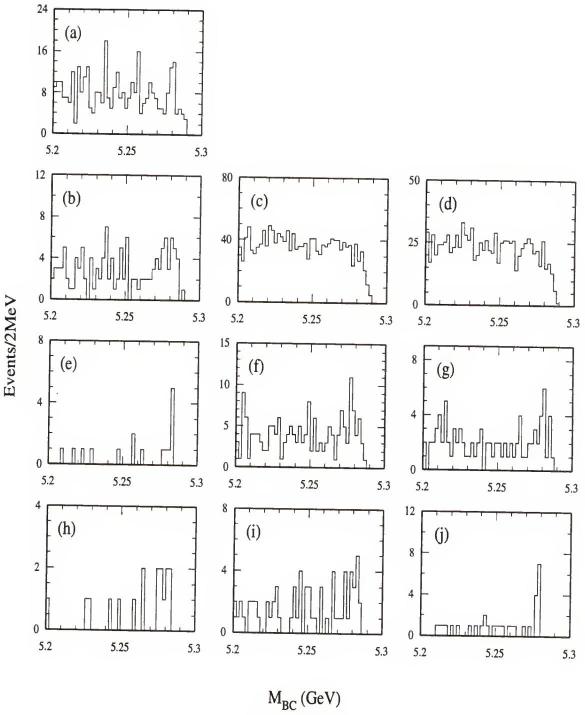

Figure 5.3 $B\bar{B}$ Monte Carlo $\mathrm{M_{BC}}$ spectrum, $B \to D^{(*)}a_1$.

In (a) the $B^0 \to D^+a_1^-$ in the D^+ decay mode $D^+ \to K^-\pi^+\pi^+$. In (b) through (d) the $B^- \to D^0a_1^-$ in the D^0 decay modes $K^-\pi^+$, $K^-\pi^+\pi^0$ and $K^-\pi^+\pi^-\pi^+$, respectively. In (e) through (g) the $B^- \to D^{*0}a_1^-$ in the D^0 decay modes $K^-\pi^+$, $K^-\pi^+\pi^0$ and $K^-\pi^+\pi^-\pi^+$. In (h) through (j) the $B^0 \to D^{*+}a_1^-$ in the D^0 decay modes $K^-\pi^+$, $K^-\pi^+\pi^0$ and $K^-\pi^+\pi^-\pi^+$.

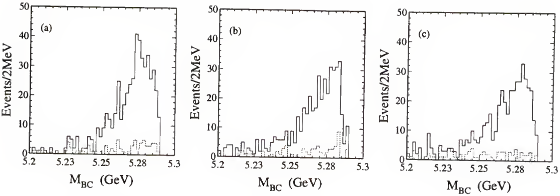

Figure 5.4 Background contribution from $D^{*0} \to D^0\gamma$.
In (a) the $D^0 \to K^-\pi^+$ in (b) the $D^0 \to K^-\pi^+\pi^0$ and in (c) the $D^0 \to K^-\pi^+\pi^-\pi^+$ D^0 subdecay modes.

To remove this background from the $B^- \to D^0\rho^-$ M_{BC} distribution a cut on $\cos(\Theta_h) \geq 0.4$ was on imposed on all B candidates.† This requirement effectively vetos events where the neutral pion produced in the decay of the ρ^- is directed in the backwards direction with respect to the direction of the ρ^-. Eliminating decays which contain a slow neutral pion significantly reduces the background contributions from $D^{*0} \to D^0\gamma$ decays. Figure 5.4 illustrates the dramatic drop in the backgrounds achived by vetoing slow π^0s. The plots were made by taking a Monte Carlo sample of 2000 $B^- \to D^{*0}\pi^-, D^{*0} \to D^0\gamma$ events and reconstructing them as $D^0\rho^-$. The solid (dashed) histograms in (a)-(c) show the background levels before and (after) the application of the veto. A reduction of approximately 90% was obtained in all three modes.

While this background contributes significantly in the signal region, the background shape used to fit the distribution accommodates the broad peaks

† The cosine of the helicity angle describes the polarization of the ρ^- and forms a $\cos^2$ distribution (see Section 4.6.1).

from the $D^{*0} \to D^0\gamma$ background when the large continuum component is included in the overall background shape. As a consistency check, the branching fractions for these B decay mode were recomputed using the yields and acceptances corresponding to the slow π^0 vetoed sample. The results agreed by better than one standard deviation (see Chapter 6).

In Figure 5.3 (e and j) some excess in the signal region is also found for the two $B \to D^* a_1$ modes. By looking at the details of the generated events in this region of the $\mathrm{M_{BC}}$ spectrum ($5.270 \leq \mathrm{M_{BC}} \leq 5.286$) we find that most of the events, about 70%, are due to $B \to D^* \rho^0 \pi^-$ or $B \to D^* \pi^- \pi^+ \pi^-$ decays. This background is consistent with the upper limits on the amount of non-resonant contribution to the event yield in $B^- \to D^{*0} a_1^-$ and $\bar{B}^0 \to D^{*+} a_1^-$ discussed in Section 5.2.

5.1.2 Background Contribution from Continuum Events

The continuum background contributions is the largest single component of the overall background in the $\mathrm{M_{BC}}$ spectra. The fractional contribution of continuum backgrounds ranges from 58% in the $B^- \to D^{*0} \rho^-$ decay mode to 91% in the $B^- \to D^0 \pi^-$ mode. The fraction also varies as a function of the D^0 subchannel, typically larger in the cleaner $D^0 \to K^- \pi^+$ modes where the contribution from $B\bar{B}$ backgrounds combinatorics is small.

The $\mathrm{M_{BC}}$ spectra for off resonance data are shown in Figure 5.5 through 5.7. The off resonance data was taken at a center of mass energy 30 MeV below the $\Upsilon(4S)$. Also, the integrated luminosity is a factor off two smaller than the on-resonance sample. To compensate for these differences, the distributions

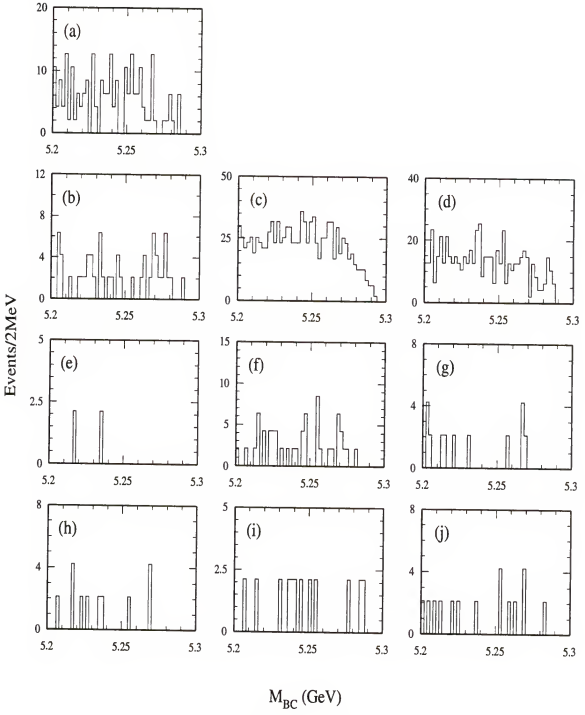

Figure 5.5 Scaled continuum M_{BC} spectrum, $B \to D^{(*)}\pi$.

In (a) the $B^0 \to D^+\pi^-$ in the D^+ decay mode $D^+ \to K^-\pi^+\pi^+$. In (b) through (d) the $B^- \to D^0\pi^-$ in the D^0 decay modes $K^-\pi^+$, $K^-\pi^+\pi^0$ and $K^-\pi^+\pi^-\pi^+$, respectively. In (e) through (g) the $B^- \to D^{*0}\pi^-$ in the D^0 decay modes $K^-\pi^+$, $K^-\pi^+\pi^0$ and $K^-\pi^+\pi^-\pi^+$. In (h) through (j) the $B^0 \to D^{*+}\pi^-$ in the D^0 decay modes $K^-\pi^+$, $K^-\pi^+\pi^0$ and $K^-\pi^+\pi^-\pi^+$.

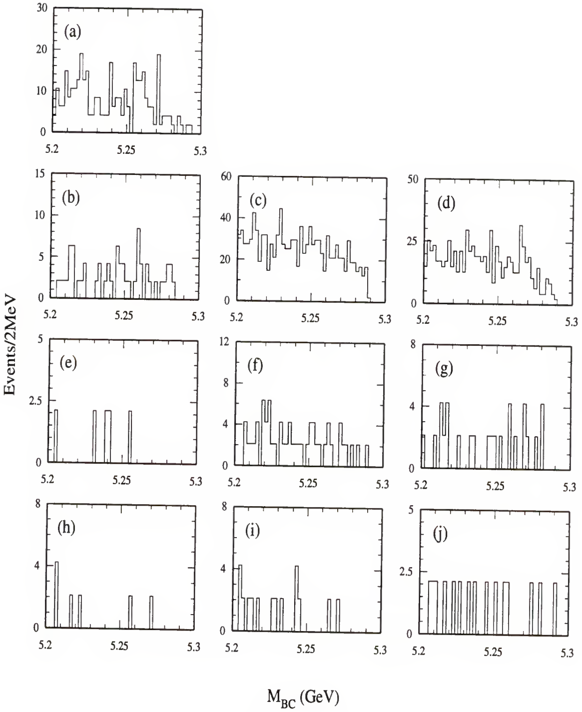

Figure 5.6 Scaled continuum $\mathrm{M_{BC}}$ spectrum, $B \to D^{(*)}\rho$.

In (a) the $B^0 \to D^+\rho^-$ in the D^+ decay mode $D^+ \to K^-\pi^+\pi^+$. In (b) through (d) the $B^- \to D^0\rho^-$ in the D^0 decay modes $K^-\pi^+$, $K^-\pi^+\pi^0$ and $K^-\pi^+\pi^-\pi^+$, respectively. In (e) through (g) the $B^- \to D^{*0}\rho^-$ in the D^0 decay modes $K^-\pi^+$, $K^-\pi^+\pi^0$ and $K^-\pi^+\pi^-\pi^+$. In (h) through (j) the $B^0 \to D^{*+}\rho^-$ in the D^0 decay modes $K^-\pi^+$, $K^-\pi^+\pi^0$ and $K^-\pi^+\pi^-\pi^+$.

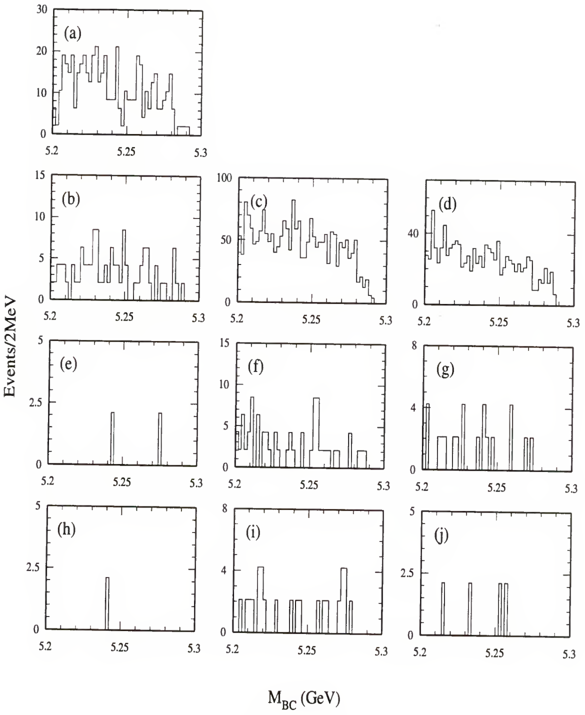

Figure 5.7 Scaled continuum M_{BC} spectrum, $B \to D^{(*)}a_1$.

In (a) the $B^0 \to D^+ a_1^-$ in the D^+ decay mode $D^+ \to K^-\pi^+\pi^+$. In (b) through (d) the $B^- \to D^0 a_1^-$ in the D^0 decay modes $K^-\pi^+$, $K^-\pi^+\pi^0$ and $K^-\pi^+\pi^-\pi^+$, respectively. In (e) through (g) the $B^- \to D^{*0} a_1^-$ in the D^0 decay modes $K^-\pi^+$, $K^-\pi^+\pi^0$ and $K^-\pi^+\pi^-\pi^+$. In (h) through (j) the $B^0 \to D^{*+} a_1^-$ in the D^0 decay modes $K^-\pi^+$, $K^-\pi^+\pi^0$ and $K^-\pi^+\pi^-\pi^+$.

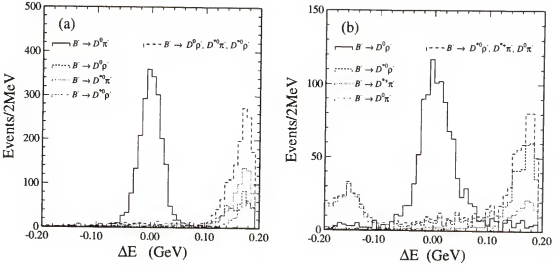

Figure 5.8 ΔE distributions in Monte Carlo.

The Monte Carlo ΔE spectra for (a) $B^- \to D^0\pi^-$ and (b) $B^- \to D^0\rho^-$ modes.

were scaled by

$$\frac{\mathcal{L}_{\text{on}}}{\mathcal{L}_{\text{off}}} \cdot \frac{s^2_{\text{off}}}{s^2_{\text{on}}} = 2.12 \tag{5.1}$$

and shifted by 30 MeV.

5.1.3 <u>M$_{\text{BC}}$ Background Spectra from ΔE Sidebands</u>

To model the M$_{\text{BC}}$ backgrounds in on-resonance data, B meson candidates were formed using the ΔE sidebands. The ΔE sidebands were taken on opposite sides of the ΔE interval centered at zero. Events selected in this way have the same number and type of final state particles, with similar kinematics, as do signal events but cannot be a product of real B decays since their reconstructed energy does not equal the energy of the beam. While the similarities indicate that we have a relatively good background model, two important facts make this method less than ideal for determining the overall background contribution. First, if we exclude the ΔE regions less than $3.0\sigma_{\Delta E}$ away from zero and the region of ΔE where contributions from other decay modes, one pion mass removed are expected, only a small range of ΔE is available for comparison. In Figure 5.8 the available ΔE regions for $B^- \to D^0\pi^-$ and $B^- \to D^0\rho^-$ that forms the ΔE sideband spectra are shown. The available range is the region between the large peaks. Secondly, the ΔE distributions are biased towards zero by the procedure of picking the candidate with the smallest ΔE as the best candidate per event per mode. Both of these conditions lead to a M_{BC} background model whose normalization does not compare well with the overall background levels in signal M_{BC} distributions.

The plots in Figure 5.8 also reveal the background contributions to the ΔE spectrum from decay modes other than the one being reconstructed. The plots were made by reconstructing Monte Carlo simulations of various B decay channels. The various decay modes are indicated within each plots and were reconstructed as either a (a) $B^- \to D^0\pi^-$ or (b) a $B^- \to D^0\rho^-$. The peaks centered at 0 are the results of reconstructing the correct Monte Carlo sample while the peaks on either side are the result of reconstructing the other $B\bar{B}$ decay modes. The number of events for each Monte Carlo samples was normalized to the number of events in either the $B^- \to D^0\pi^-$ or the $\bar{B}^0 \to D^+\rho^-$ Monte Carlo sample to insure that the combined plots represented the expected backgrounds in data without the continuum component.

In Figures 5.9, 5.10 and 5.11 the ΔE sideband M_{BC} spectra are plotted for all non color-suppressed modes. The ΔE sidebands are defined in the ΔE region greater than or equal to $3\sigma_{\Delta E}$ and less than ± 100 MeV. The 100 MeV

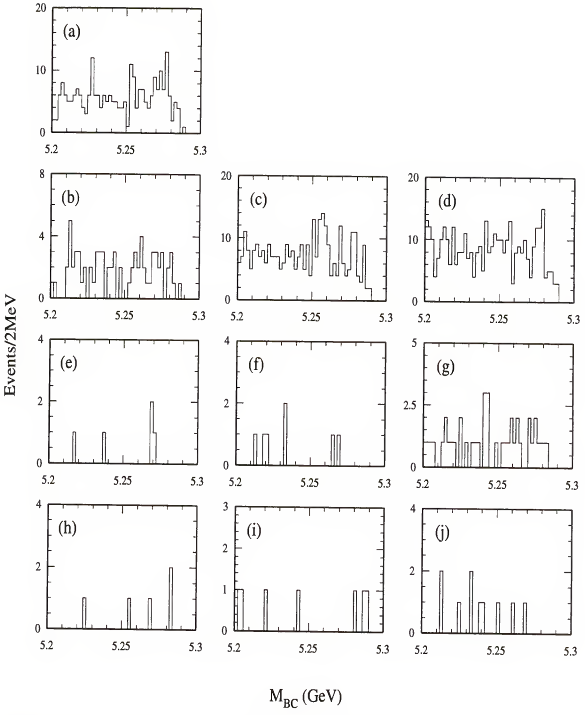

Figure 5.9 ΔE sideband M_{BC} spectrum, $B \to D^{(*)}\pi$.

In (a) the $B^0 \to D^+\pi^-$ in the D^+ decay mode $D^+ \to K^-\pi^+\pi^+$. In (b) through (d) the $B^- \to D^0\pi^-$ in the D^0 decay modes $K^-\pi^+$, $K^-\pi^+\pi^0$ and $K^-\pi^+\pi^-\pi^+$, respectively. In (e) through (g) the $B^- \to D^{*0}\pi^-$ in the D^0 decay modes $K^-\pi^+$, $K^-\pi^+\pi^0$ and $K^-\pi^+\pi^-\pi^+$. In (h) through (j) the $B^0 \to D^{*+}\pi^-$ in the D^0 decay modes $K^-\pi^+$, $K^-\pi^+\pi^0$ and $K^-\pi^+\pi^-\pi^+$.

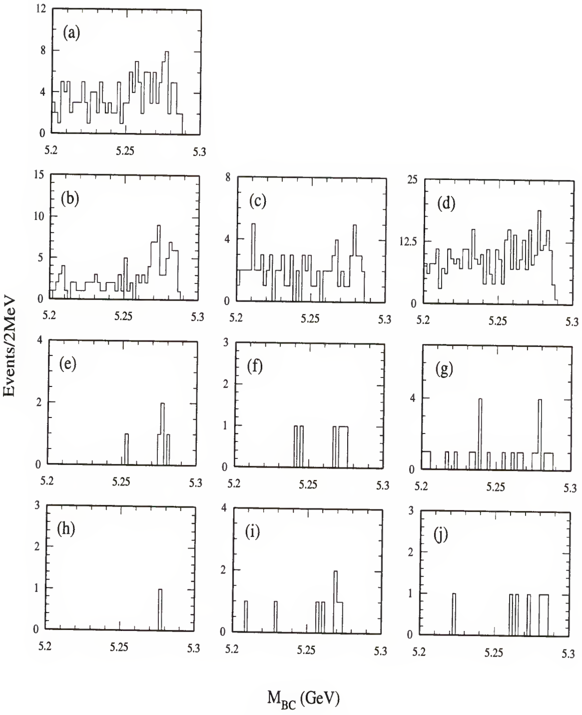

Figure 5.10 ΔE sideband M_{BC} spectrum, $B \to D^{(*)}\rho$.

In (a) the $B^0 \to D^+\rho^-$ in the D^+ decay mode $D^+ \to K^-\pi^+\pi^+$. In (b) through (d) the $B^- \to D^0\rho^-$ in the D^0 decay modes $K^-\pi^+$, $K^-\pi^+\pi^0$ and $K^-\pi^+\pi^-\pi^+$, respectively. In (e) through (g) the $B^- \to D^{*0}\rho^-$ in the D^0 decay modes $K^-\pi^+$, $K^-\pi^+\pi^0$ and $K^-\pi^+\pi^-\pi^+$. In (h) through (j) the $B^0 \to D^{*+}\rho^-$ in the D^0 decay modes $K^-\pi^+$, $K^-\pi^+\pi^0$ and $K^-\pi^+\pi^-\pi^+$.

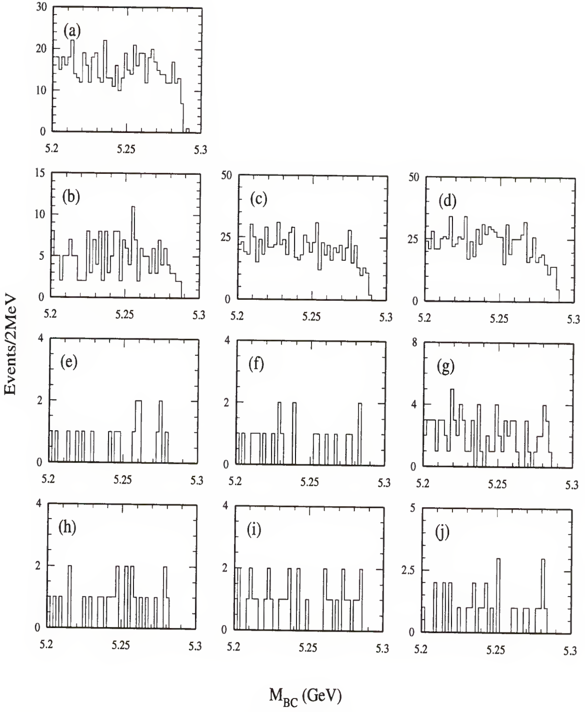

Figure 5.11 ΔE sideband M_{BC} spectrum, $B \to D^{(*)}a_1$.

In (a) the $B^0 \to D^+a_1^-$ in the D^+ decay mode $D^+ \to K^-\pi^+\pi^+$. In (b) through (d) the $B^- \to D^0a_1^-$ in the D^0 decay modes $K^-\pi^+$, $K^-\pi^+\pi^0$ and $K^-\pi^+\pi^-\pi^+$, respectively. In (e) through (g) the $B^- \to D^{*0}a_1^-$ in the D^0 decay modes $K^-\pi^+$, $K^-\pi^+\pi^0$ and $K^-\pi^+\pi^-\pi^+$. In (h) through (j) the $B^0 \to D^{*+}a_1^-$ in the D^0 decay modes $K^-\pi^+$, $K^-\pi^+\pi^0$ and $K^-\pi^+\pi^-\pi^+$.

cutoff is used to avoid contamination from B meson decays which differ by one pion. The 100 MeV value was chosen to accommodate the width of the ΔE peak in the region one pion mass removed.

5.1.4 M_{BC} Background Spectra from Wrong Sign "B" Candidates

The wrong sign combination M_{BC} spectrum was also used to model the M_{BC} backgrounds, in on-resonance data. The M_{BC} distributions of wrong sign "B "candidates were formed by applying the algorithm used in forming real B candidates but with the light meson swapped with its charge conjugate. This method reproduces the kinematics of real B meson decays but does not accurately model contributions to the background from decays of other B mesons. This technique thus models background contributions from random combinations of particle but suffers in its ability to predict contributions from real $B\bar{B}$ backgrounds.

The wrong sign M_{BC} spectra for non color-suppressed B decay modes are shown in Figures 5.12, 5.13 and 5.14. In modes where the decay chain produces a D^0 an additional veto was introduced to eliminate the possibility of contaminating the wrong sign M_{BC} spectrum with real charge-conjugate ($\bar{B}$) meson decays. This can result when a $\bar{D}^0$ is incorrectly reconstructed as a D^0 if both the K^- and π^+ from the D^0 decay are misidentified as a π^- and K^+ respectively. The double misidentification would lead to an excess in the number of events in the signal region from the misidentified (conjugate) B decay. The veto used eliminated events if the D^0 reflection mass, defined as the invariant mass calculated with the mass assignments reversed, falls within 30 MeV from the nominal D^0 mass. The D^0 reflection mass veto was used for both the $D^0 \to K^-\pi^+$ and $D^0 \to K^-\pi^+\pi^0$ modes but not the $D^0 \to K^-\pi^+\pi^-\pi^+$

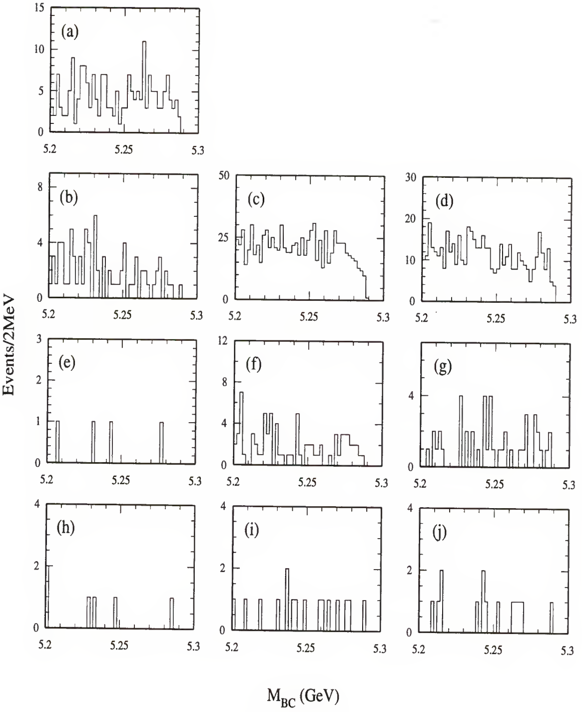

Figure 5.12 Wrong sign M_{BC} spectrum, $B \to D^{(*)}\pi$.

In (a) the $B^0 \to D^+\pi^-$ in the D^+ decay mode $D^+ \to K^-\pi^+\pi^+$. In (b) through (d) the $B^- \to D^0\pi^-$ in the D^0 decay modes $K^-\pi^+$, $K^-\pi^+\pi^0$ and $K^-\pi^+\pi^-\pi^+$, respectively. In (e) through (g) the $B^- \to D^{*0}\pi^-$ in the D^0 decay modes $K^-\pi^+$, $K^-\pi^+\pi^0$ and $K^-\pi^+\pi^-\pi^+$. In (h) through (j) the $B^0 \to D^{*+}\pi^-$ in the D^0 decay modes $K^-\pi^+$, $K^-\pi^+\pi^0$ and $K^-\pi^+\pi^-\pi^+$.

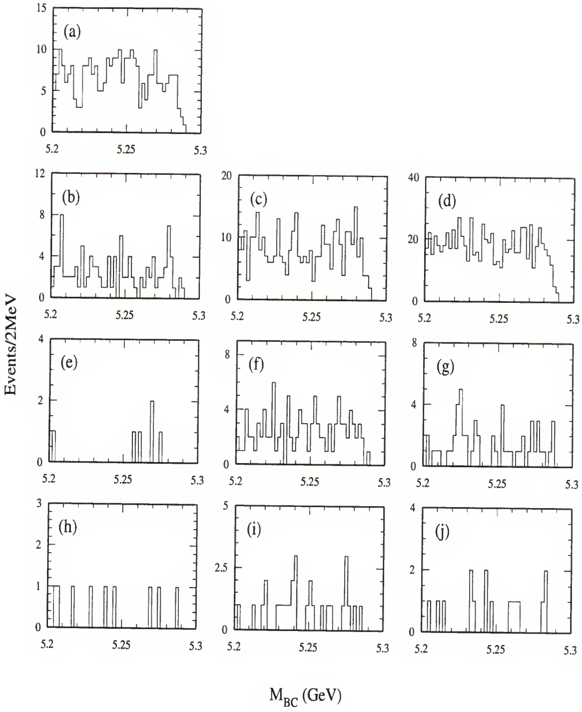

Figure 5.13 Wrong sign M_{BC} spectrum, $B \to D^{(*)}\rho$.

In (a) the $B^0 \to D^+\rho^-$ in the D^+ decay mode $D^+ \to K^-\pi^+\pi^+$. In (b) through (d) the $B^- \to D^0\rho^-$ in the D^0 decay modes $K^-\pi^+$, $K^-\pi^+\pi^0$ and $K^-\pi^+\pi^-\pi^+$, respectively. In (e) through (g) the $B^- \to D^{*0}\rho^-$ in the D^0 decay modes $K^-\pi^+$, $K^-\pi^+\pi^0$ and $K^-\pi^+\pi^-\pi^+$. In (h) through (j) the $B^0 \to D^{*+}\rho^-$ in the D^0 decay modes $K^-\pi^+$, $K^-\pi^+\pi^0$ and $K^-\pi^+\pi^-\pi^+$.

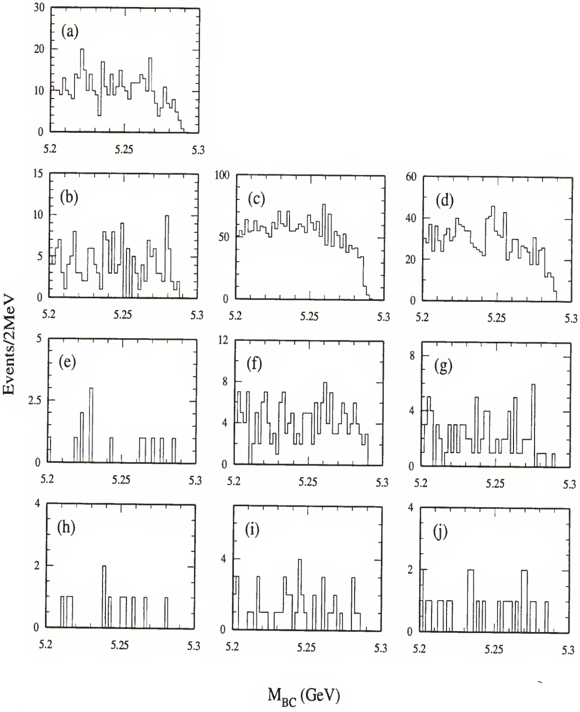

Figure 5.14 Wrong sign M_{BC} spectrum, $B \to D^{(*)}a_1$.

In (a) the $B^0 \to D^+ a_1^-$ in the D^+ decay mode $D^+ \to K^-\pi^+\pi^+$. In (b) through (d) the $B^- \to D^0 a_1^-$ in the D^0 decay modes $K^-\pi^+$, $K^-\pi^+\pi^0$ and $K^-\pi^+\pi^-\pi^+$, respectively. In (e) through (g) the $B^- \to D^{*0} a_1^-$ in the D^0 decay modes $K^-\pi^+$, $K^-\pi^+\pi^0$ and $K^-\pi^+\pi^-\pi^+$. In (h) through (j) the $B^0 \to D^{*+} a_1^-$ in the D^0 decay modes $K^-\pi^+$, $K^-\pi^+\pi^0$ and $K^-\pi^+\pi^-\pi^+$.

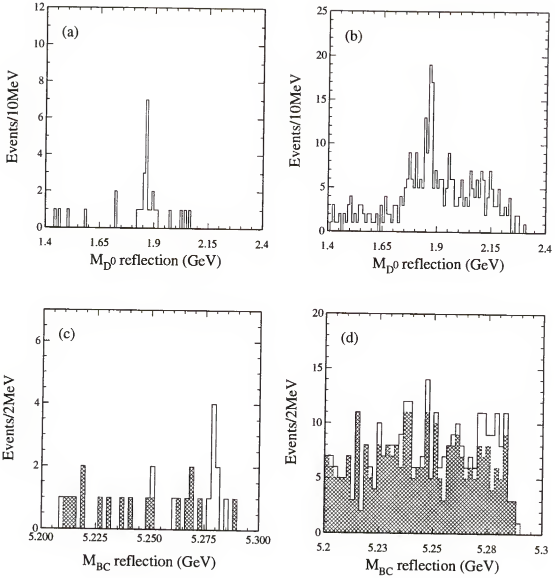

Figure 5.15 Reflection D^0 mass spectrums for wrong sign "B" candidate. Misidentified D^0 mass spectra for the (a) K^- π^+ (b) and $D^0 \to K^-\pi^+$ modes in the wrong sign $B^- \to D^0\pi^-$ decay mode.

modes. In the latter, the momentum spectrum of the kaons and pions are softer and thus particle ID is improved. The larger number of daughters also reduces the likelihood of misidentification. In Figure 5.15 (a) and (b) the peaks in the D^0 reflection mass spectrum at the D^0 mass for the $D^0 \rightarrow K^-\pi^+$ and $D^0 \rightarrow K^-\pi^+\pi^0$ wrong sign "B " candidates are shown. The plots were formed by analyzing on-resonance wrong sign data, requiring events to satisfy all B candidate requirements and to fall within 6 MeV of the $\mathrm{M_{BC}}$. In Figure 5.15 (c) and (d) the $\mathrm{M_{BC}}$ distributions for wrong sign data with (hatched) and without (unhatched) the reflection mass veto are shown.

5.1.5 Test of Background Shapes

In the preceding discussion we have presented the $\mathrm{M_{BC}}$ backgrounds spectra separated into continuum and $B\bar{B}$ components and presented two ways of modeling the background in data. In this section we discuss the conclusions which were drawn from the analysis of these background $\mathrm{M_{BC}}$ distributions.

To test the validity of the assumption that the $\mathrm{M_{BC}}$ backgrounds consist of a continuum and a $B\bar{B}$ component we compared the sum of the scaled continuum plus the $B\bar{B}$ background model to signal distributions by superimposing the plots. The continuum component is taken from the off resonance data scaled as described in Section 5.1.2. The $B\bar{B}$ component was taken from the $B\bar{B}$ Monte Carlo (antiskim) sample and was normalized to the number of on-resonance $B\bar{B}$ events. Figure 5.16 reveals that the sum accounts for all of the background present and that both the shape and the the normalization are adequate modeled by this background estimate.

To insure that the ΔE sidebands model the shape of the true background the $\mathrm{M_{BC}}$ spectrum was formed with the ΔE sideband technique on the full $B\bar{B}$

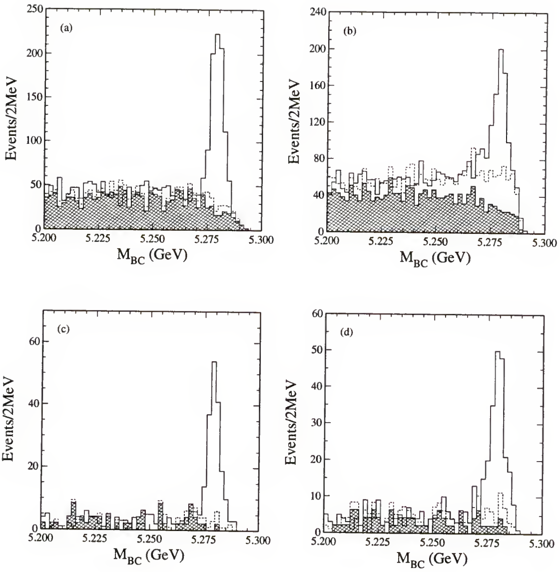

Figure 5.16 Superposition of continuum and $B\bar{B}$ background components.

The dashed histogram shows the sum of the scaled continuum plus $B\bar{B}$ background components, the hatched histogram shows the continuum component superimposed on the signal M_{BC} spectra. The B decay modes shown are the (a) $B^- \to D^0\pi^-$, (b) $B^- \to D^0\rho^-$, (c) $B^- \to D^{*0}\pi^-$ and (d) $B^- \to D^{*0}\rho^-$. All three of the D^0 decay modes are included.

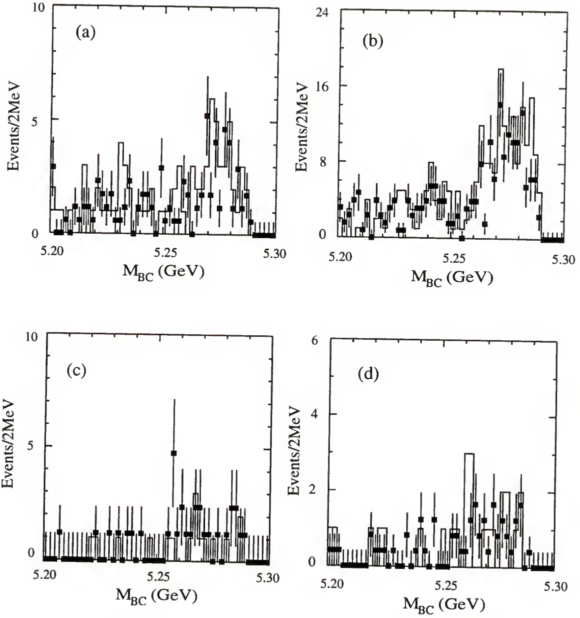

Figure 5.17 $B\bar{B}$ compared to ΔE sideband backgrounds.

A Monte Carlo simulation of the M_{BC} distributions of $B\bar{B}$ background (solid histogram), compared with the ΔE sidebands from the same Monte Carlo (points). All events in the signal modes have been removed from the $B\bar{B}$ Monte Carlo simulation. (a) $B^- \to D^0\pi^-$, (b) $B^- \to D^0\rho^-$, (c) $B^- \to D^{*0}\pi^-$, and (d) $B^- \to D^{*0}\rho^-$.

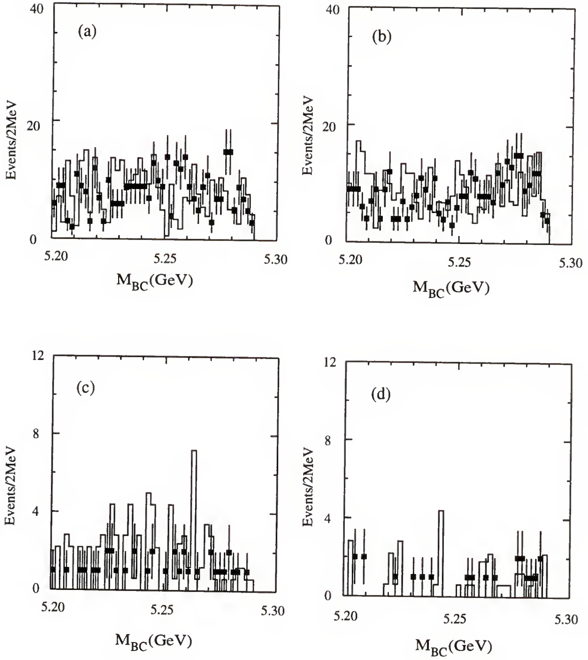

Figure 5.18 $B\bar{B}$ plus continuum compared to ΔE sideband backgrounds.

M_{BC} distributions for ΔE sidebands in on-resonance data (solid histogram) compared to the sum of continuum data and a Monte Carlo simulation of $B\bar{B}$ background (points) (a) $B^- \to D^0\pi^-$, (b) $B^- \to D^0\rho^-$, (c) $B^- \to D^{*0}\pi^-$, and (d) $B^- \to D^{*0}\rho^-$.

Monte Carlo sample. These distributions were then compared to our model of the true background, the $B\bar{B}$ antiskim M_{BC} spectra. The comparison was made by superimposing the antiskim and the ΔE sideband distributions, see Figure 5.17. The figures reveal that the shapes of the distributions match rather well and thus ΔE sideband technique accurately models the shape of the true background. As an additional check the ΔE sidebands distributions for on-resonance data were compared to the sum of the scaled continuum plus the $B\bar{B}$ Monte Carlo background M_{BC} distribution (Figure 5.18). To allow for direct comparison of the background shapes, the overall normalization of the combined $B\bar{B}$ and continuum distributions was allowed to float. The shape of the ΔE sideband spectra also matches the shape of the sum.

Several functions were used to represent the background data, including a straight line with a variable slope, a smooth function with a cut off at the beam energy used by the ARGUS [44] experiment and the CLEO background shape. The CLEO background shape was found to fit the background distribution best. The CLEO background shape is defined as a straight line with a parabolic roll-off at the M_{BC} endpoint. The functional from is described by

$$y(x) = \begin{cases} mx + b, & x \leq x_o \\ mx_o\{1 - (x - x_o)^2 + b\} & x_o \leq x \leq E_b \end{cases} \tag{5.2}$$

where E_b is the beam energy and $x_o = E_b - x_{\text{offset}}$ is the point where the parabolic roll-off begins. Figures 5.19 and 5.20 show the CLEO background shape fit to ΔE sideband and wrong sign background distributions. They show that both distributions are fit adequately by the shape. The offset was fixed at 8 MeV on all non color-suppressed modes. In color-suppressed modes the offset was varied and the value which gave the most conservative upper limit was used.

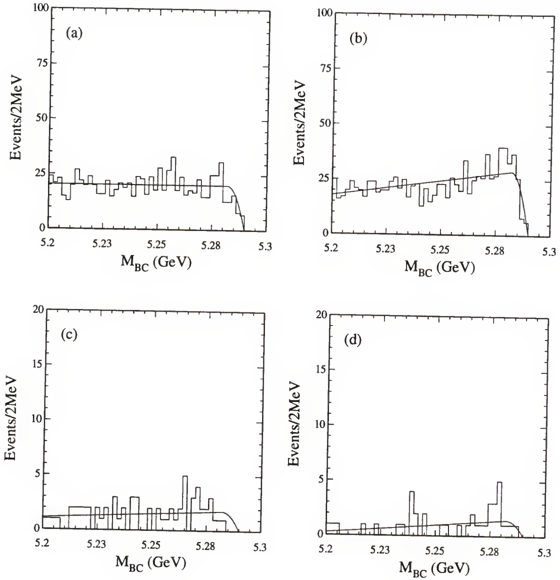

Figure 5.19 CLEO background function fit to ΔE sidebands M_{BC} spectra. In (a) the fit to the $B^- \to D^0\pi^-$, (b) $B^- \to D^0\rho^-$, (c) $B^- \to D^{*0}\pi^-$ and (d) $B^- \to D^{*0}\rho^-$ M_{BC} ΔE distributions. All three D^0 decay modes are included in each plot.

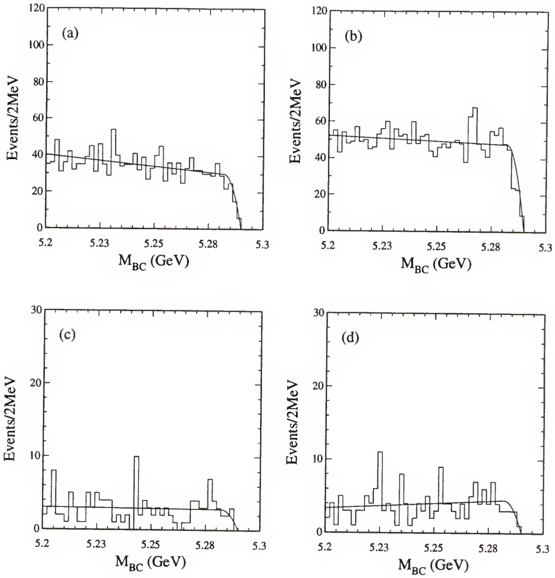

Figure 5.20 CLEO background function fit to the wrong sign M_{BC} spectra.

In (a) the fit to the $B^- \to D^0\pi^-$, (b) $B^- \to D^0\rho^-$, (c) $B^- \to D^{*0}\pi^-$ and (d) $B^- \to D^{*0}\rho^-$ M_{BC} wrong sign distributions. All three of the D^0 decay modes are included in each plot.

Table 5.1

Event yield with different background parameters

B Decay Mode	D Decay Mode	Yields				relative error from S.D.
		unfixed	$B\bar{B}$ + cont.	ΔE S.B.	Wrong sign	
$D^+\pi^-$	$K^-\pi^+\pi^+$	170.7	178.8	164.4	166.9	0.037
$D^{*+}\pi^-$	$K^-\pi^+$	51.7	51.8	51.8	51.5	0.003
	$K^-\pi^+\pi^0$	85.0	88.7	87.7	93.1	0.040
	$K^-\pi^+\pi^-\pi^+$	45.7	46.5	46.7	47.3	0.014
$D^0\pi^-$	$K^-\pi^+$	162.3	159.5	171.1	160.0	0.033
	$K^-\pi^+\pi^0$	303.7	302.6	323.8	289.0	0.047
	$K^-\pi^+\pi^-\pi^+$	194.0	197.6	194.0	191.7	0.013
$D^{*0}\pi^-$	$K^-\pi^+$	32.9	32.5	33.4	32.2	0.016
	$K^-\pi^+\pi^0$	73.2	81.1	81.1	84.6	0.066
	$K^-\pi^+\pi^-\pi^+$	50.7	50.7	48.8	51.0	0.021
$D^+\rho^-$	$K^-\pi^+\pi^+$	171.0	179.7	172.3	158.0	0.053
$D^{*+}\rho^-$	$K^-\pi^+$	51.3	60.9	59.5	51.6	0.099
	$K^-\pi^+\pi^0$	83.7	93.5	90.4	88.7	0.049
	$K^-\pi^+\pi^-\pi^+$	44.5	52.6	48.3	42.2	0.103
$D^0\rho^-$	$K^-\pi^+$	122.9	113.1	142.0	116.2	0.105
	$K^-\pi^+\pi^0$	205.9	218.0	241.7	187.4	0.110
	$K^-\pi^+\pi^-\pi^+$	126.5	131.7	147.6	115.8	0.105
$D^{*0}\rho^-$	$K^-\pi^+$	46.0	46.2	47.7	44.0	0.033
	$K^-\pi^+\pi^0$	76.4	82.9	83.9	76.2	0.054
	$K^-\pi^+\pi^-\pi^+$	34.5	35.7	36.3	32.1	0.055
$D^+a_1^-$	$K^-\pi^+\pi^+$	92.3	107.4	104.9	93.5	0.084
$D^{*+}a_1^-$	$K^-\pi^+$	37.4	34.2	37.5	34.8	0.046
	$K^-\pi^+\pi^0$	37.4	43.7	47.1	43.7	0.109
	$K^-\pi^+\pi^-\pi^+$	26.6	21.9	26.0	24.7	0.079
$D^0a_1^-$	$K^-\pi^+$	48.2	47.2	56.9	62.4	0.151
	$K^-\pi^+\pi^0$	65.3	102.9	103.8	76.2	0.296
	$K^-\pi^+\pi^-\pi^+$	44.3	61.8	51.6	40.4	0.212
$D^{*0}a_1^-$	$K^-\pi^+$	18.2	18.1	20.8	20.9	0.086
	$K^-\pi^+\pi^0$	42.0	44.0	39.5	48.9	0.095
	$K^-\pi^+\pi^-\pi^+$	22.7	20.0	23.3	21.3	0.064

5.1.6 Systematic Errors from Background Shapes

Systematic errors due to the background shape were determined by comparing the M_{BC} yields obtained with different CLEO background function parameterizations. The yields were determined four times for each mode. Each time the M_{BC} distribution was fit using different values for the background parameters. First, all variable background parameters were allowed to float. The parameters were then fixed to three different sets of values, each obtained by fitting a particular background model. The background models used were: the sum of $B\bar{B}$ Monte Carlo and scaled continuum with both normalizations fixed, the ΔE sideband and the wrong sign combination on-resonance data. The errors from the background contribution were obtained for each mode by finding the standard deviation of all four yield determinations. The standard deviation and the yields determined with all the background functions are listed in Table 5.1.

5.2 Non-Resonant Background Contributions

In decays to multiple pion final states the non-resonant contribution to the number of observed events were determined by comparing the invariant mass spectrum of the composite final state to the expected distributions for resonant and non-resonant decays in Monte Carlo simulations. The invariant mass distributions were formed by first reconstructing the events as described in Chapter 4 without the invariant mass cut on the "light" meson daughter. The invariant mass plots are then formed by taking events that fall within the M_{BC} signal and subtracting the background taken from the M_{BC} sidebands. The M_{BC} sidebands were defined to be between 5.20 GeV and 5.26 GeV. The M_{BC}

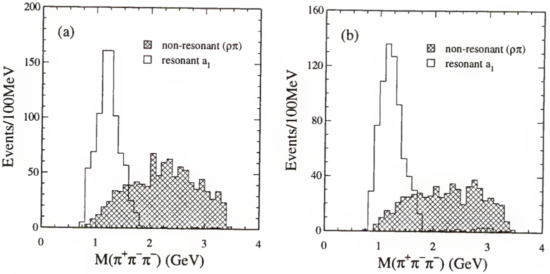

Figure 5.21 Resonant and non-resonant simulation of $B \to Da_1$ decays. The invariant $\pi\pi\pi$ mass in Monte Carlo simulations of (a) $B^- \to D^0 a_1^-$ $(\rho\pi)$ and (b) $\bar{B}^0 \to D^+ a_1^-$ $(\rho\pi)$ modes. The solid histograms shows the distribution when the $\pi\pi\pi$ are the decay products of an a_1^- resonance. The hatched histogram shows the resulting $\pi\pi\pi$ distribution when the particles are first formed into a ρ and π.

sideband invariant mass spectrum was scaled before the subtraction. The background subtracted plot was then fit to the sum of resonant and non-resonant invariant mass distributions whose shapes were determined from Monte Carlo with the normalizations taken as free parameters in the fit.

To illustrate the method we show the procedure as applied to the extraction of the relative non-resonant $(\rho^0\pi^-)$ contribution to the $B^- \to D^0 a_1^-$ and $\bar{B}^0 \to D^+ a_1^-$ decays.† The a_1^- invariant mass distributions for resonant and non-resonant Monte Carlo are shown in Figure 5.21. These histograms were used to fit the background subtracted a_1 invariant mass plots (Figure 5.22 (a) and

† The shape of the $\pm\pi^+\pi^-$ invarient mass distribution is very similar to the $\rho^0\pi^-$ distribution.

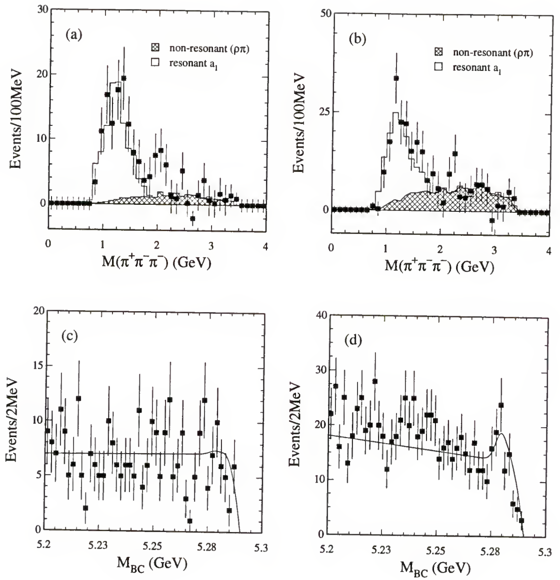

Figure 5.22 Non-resonant contribution to $B \to Da_1$ decays.

In (a) and (b) the background subtracted $\pi^-\pi^+\pi^-$ invariant mass distributions for the $B^- \to D^0 a_1^-$, $D^0 \to K^-\pi^+$ and the $\bar{B}^0 \to D^+ a_1^-$, $D^+ \to K^-\pi^+\pi^+$ modes. The black squares represent the background subtracted data, the solid and hatched histograms are the result of the fit from the Monte Carlo distributions. In (c) and (d) the M_{BC} distributions are shown for the $B^- \to D^0 a_1^-$ and $\bar{B}^0 \to D^+ a_1^-$ with a cut in the a_1 poor region of the $\pi^-\pi^+\pi^-$ spectrum.

(b)). Integrating the non-resonant shape (hatched histogram in Figure 5.21 (a-b) we find that 5.9 ± 2.6 events fall between 1.0 GeV and 1.6 GeV in the $B^- \to D^0 a_1^-$ mode and 19.6 ± 4.0 events in the $\bar{B}^0 \to D^+ a_1^-$ mode. This implies that non-resonant decays contribution to the $B^- \to D^0 a_1^-$ and $\bar{B}^0 \to D^+ a_1^-$ are less then 11.5% and 24.3% at the 90% confidence level.

As a consistency check the $\mathrm{M_{BC}}$ distributions were replotted but now the a_1 invariant mass was required to lie in the a_1 poor region defined to be between 2.0 GeV and 2.6 GeV. The $\mathrm{M_{BC}}$ distributions when selecting a_1s from the poor region are shown in Figure 5.22 (c-d) for both the $B^- \to D^0 a_1^-$ and $\bar{B}^0 \to D^+ a_1^-$ respectively. The number of events found in the $\mathrm{M_{BC}}$ signal region were 1.3 ± 6.2 for the $B^- \to D^0 a_1^-$ and 18.8 ± 10.1 for the $\bar{B}^0 \to D^+ a_1^-$. The number of non-resonant contribution using this method gives less than 18% and 36%, at the 90% confidence level for $B^- \to D^0 a_1^-$ and $\bar{B}^0 \to D^+ a_1^-$. These values are consistent with the upper limits found by fitting the three pion invariant mass distributions.

A similar analysis was performed on the other resonant B meson decay modes the $B^- \to D^{*0} a_1^-$, $D^{(*)0}\rho^-$, $\bar{B}^0 \to D^{*+} a_1^-$ and $D^{(*)+}\rho^-$ by M.S. Alam *et al.* [45]. The technique used differed only in that the background subtracted resonant mass plots were fit with a Breit-Wigner and polynomial parameterizations determined from Monte Carlo simulations. The results obtained showed that the non-resonant component to the $B \to D^* \rho$ modes are less than 9.0% and less than 2.5% for the $B \to D\rho$ modes. For the $\bar{B}^0 \to D^{*+} a_1^-$ and $B^- \to D^{*0} a_1^-$ the contributions from non-resonant $\pi^- \rho^0$ and $D^{**}\rho$ were found to be less 9.4% and 10.6% at the 90% confidence level.

5.3 Backgrounds in Color-Suppressed Modes

5.3.1 $B\bar{B}$ Backgrounds

In order to examine the $B\bar{B}$ background contributions to color suppressed modes, no signal mode subtraction scheme was employed since the Monte Carlo generator decay tables do not contain appreciable branching fraction to these modes. The generator does however, uses a branching fractions of 1×10^{-4} in some of the lower multiplicity modes, such as $\bar{B}^0 \to D^0\pi^0$ and $B^0 \to D^0\rho^0$. With a sample of 2×10^6 events and low $\epsilon_{MC} \times \mathcal{B}_{D^0}$ these small rates do not appear in the plots. However, in the $\bar{B}^0 \to D^0\pi^0$ mode the Monte Carlo efficiency is somewhat larger and a few events do appear in the signal region. We verified that these events did come from the small generator $\bar{B}^0 \to D^0\pi^0$ branching fraction by inspecting a dump of the Monte Carlo events in the signal region. In Figure 5.23 and 5.24 the $\mathrm{M_{BC}}$ distributions for each of the color-suppressed $B\bar{B}$ decay modes are shown. The figures reveal that no significant contributions, other than that already discussed, are present from other known $B\bar{B}$ decays.

5.3.2 Continuum Backgrounds

The continuum background contributions are shown in Figure 5.25 and 5.26. These plots were created as previously by using off-resonance data and scaling the $\mathrm{M_{BC}}$ distributions by the appropriate factor, Equation (5.1). As with the $B\bar{B}$ background no significant contributions in the signal region are observed.

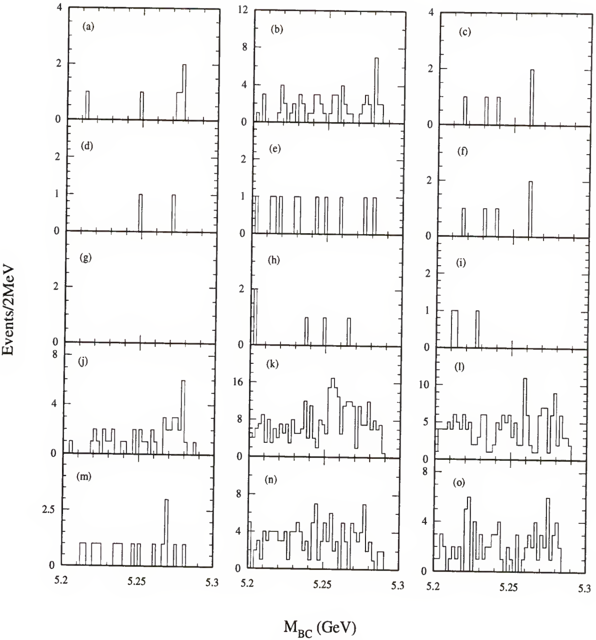

Figure 5.23 $B\bar{B}$ backgrounds in color-suppressed decays $B \to \bar{D}^0 h^0$.

Generic $B\bar{B}$ Monte Carlo data used in reconstructing the $B \to \bar{D}^0 h^0$ decay modes (a-c) $D^0\pi^0$, (d-f) $D^0\eta$, (g-i) $D^0\eta'$, (j-l) $D^0\rho^0$, and (m-o) $D^0\omega$. The first columns corresponds to the $K^-\pi^+$, $K^-\pi^+\pi^0$ and $K^-\pi^+\pi^-\pi^+$ decay modes of the D^0 respectively.

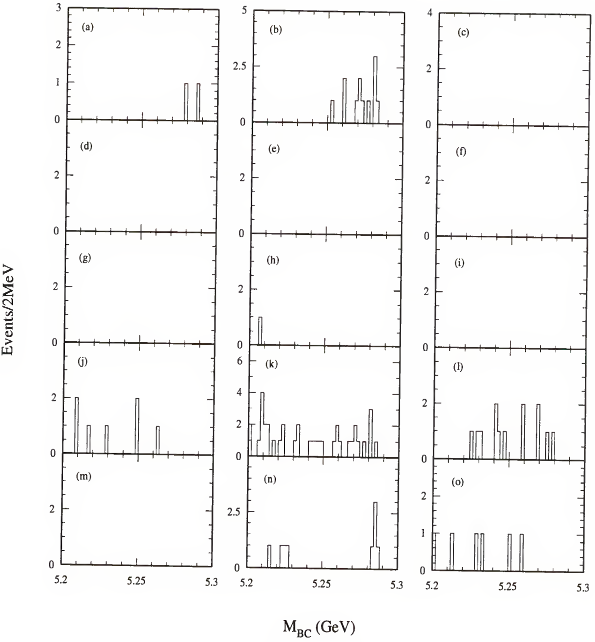

Figure 5.24 $B\bar{B}$ backgrounds in color-suppressed decays $B \to \bar{D}^{*0}h^0$.

Generic $B\bar{B}$ Monte Carlo data used in reconstructing the $B \to \bar{D}^{*0}h^0$ decay modes (a-c) $D^{*0}\pi^0$, (d-f) $D^{*0}\eta$, (g-i) $D^{*0}\eta'$, (j-l) $D^{*0}\rho^0$ and (m-o) $D^{*0}\omega$. The first columns corresponds to the $K^-\pi^+$, $K^-\pi^+\pi^0$ and $K^-\pi^+\pi^-\pi^+$ decay modes of the D^0 respectively.

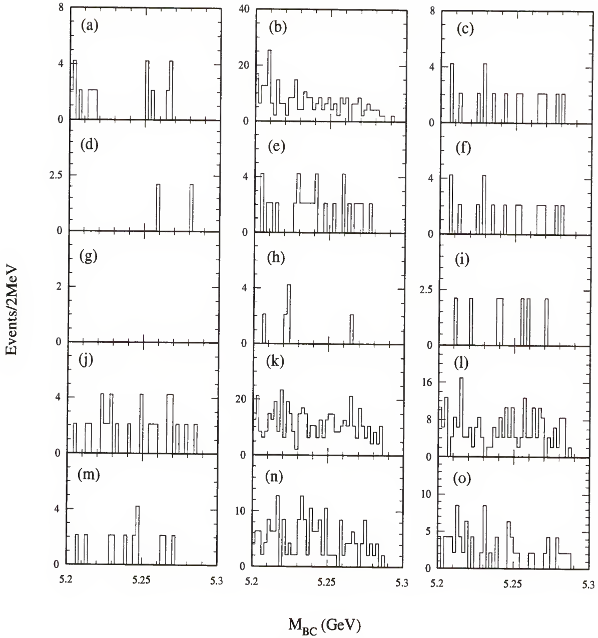

Figure 5.25 Continuum backgrounds in color-suppressed, $B \to D^0 h^0$.

Scaled and shifted continuum data reconstructed in $B^0 \to \bar{D}^0 h^0$ decay modes (a-c) $D^0\pi^0$, (d-f) $D^0\eta$, (g-i) $D^0\eta'$, (j-l) $D^0\rho^0$ and (m-o) $D^0\omega$. The first columns corresponds to the $K^-\pi^+$, $K^-\pi^+\pi^0$ and $K^-\pi^+\pi^-\pi^+$ decay modes of the D^0 respectively.

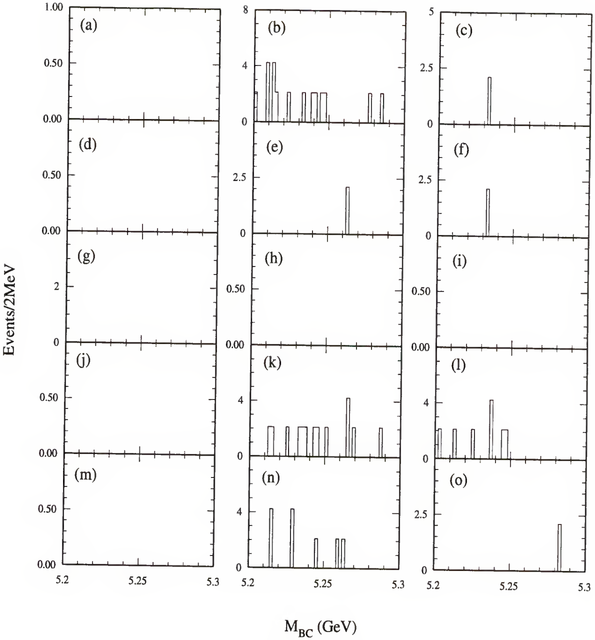

Figure 5.26 Continuum backgrounds in color-suppressed, $B \to D^{*0}h^0$.

Scaled and shifted continuum data reconstructed in $B^0 \to \bar{D}^{*0}h^0$ decay modes (a-c) $D^{*0}\pi^0$, (d-f) $D^{*0}\eta$, (g-i) $D^{*0}\eta'$, (j-l) $D^{*0}\rho^0$ and (m-o) $D^{*0}\omega$. The first columns corresponds to the $K^-\pi^+$, $K^-\pi^+\pi^0$ and $K^-\pi^+\pi^-\pi^+$ decay modes of the D^0 respectively.

CHAPTER 6
RESULTS AND DISCUSSION

Introduction

In this chapter we provide a detailed description of the experimental measurements and discuss these results in the context of the theoretical framework introduced in Chapter 2. The measurements consist of branching fraction and polarization measurements, both performed by counting the number of events found in particular distributions and correcting the yields by appropriate efficiencies and decay daughter branching fractions. The results are then used in tests of the factorization hypothesis, color suppression and to determine the values of the BSW parameters a_1, a_2 and the relative sign of a_2/a_1.

6.1 Determination of Branching Fractions

The B branching fractions were determined by using the event yields for each B decay mode, the product of the total number of $B\bar{B}$ events in the data sample, the branching fraction of the daughters and the reconstruction efficiency (ϵ_{mc_b}), determined form Monte Carlo studies. The explicit formula used to calculate the branching fractions was

$$\mathcal{B}_b = \frac{\mathrm{N_{obs}}}{\mathrm{N}_{B\bar{B}} \cdot \epsilon_{mc_b} \cdot \prod\limits_d \mathcal{B}_d} \tag{6.1}$$

The index b specifies the particular B decay mode and the index d is the product over all the relevant branching fraction of the B daughters in the particular decay chain.

The D and D^* branching fractions are taken from recent CLEO measurements. The latest CLEO results represent the most recent and accurate measurements made to date. Also by using the CLEO measurements, the total systematic error can be reduced by removing tracking errors common to this and other CLEO analyses. The branching fractions for the D^{*+} and D^{*0} modes are [46]

$$\mathcal{B}(D^{*0} \to D^0\pi^0) = 63.6 \pm 2.3 \pm 3.3\%$$

$$\mathcal{B}(D^{*+} \to D^0\pi^+) = 68.1 \pm 1.0 \pm 1.3\%$$

The branching fractions for the D^0 and D^+ decay modes are normalized to the $D^0 \to K^-\pi^+$ mode. The value of the normalization mode and the ratios are

$$\mathcal{B}(D^0 \to K^-\pi^+) = 3.91 \pm 0.08 \pm 0.17\% \text{ [47]}$$

$$\mathcal{B}(D^0 \to K^-\pi^+\pi^0)/\mathcal{B}(D^0 \to K^-\pi^+) = 3.78 \pm 0.07 \pm 0.49 \text{ [48]}$$

$$\mathcal{B}(D^0 \to K^-\pi^+\pi^-\pi^+)/\mathcal{B}(D^0 \to K^-\pi^+) = 2.05 \pm 0.11 \text{ [2]}$$

$$\mathcal{B}(D^+ \to K^-\pi^+\pi^+)/\mathcal{B}(D^0 \to K^-\pi^+) = 2.35 \pm 0.16 \pm 0.16 \text{ [49]}$$

We use the ratios of D branching fractions to determine the B branching fractions since these are known to greater accuracy than are the absolute values.

6.1.1 Decays to Non Color-Suppressed Modes

The event yields for the non color-suppressed decays were determined by fitting the M_{BC} distribution for events that passed all the B meson reconstruction requirements discussed in Chapter 4. The distributions were fit to a Gaussian of fixed width plus a background shape. The width of the Gaussian was fixed to 2.64 MeV for all modes. This value was determined from Monte

Carlo studies and found not to vary significantly from mode to mode. The background shape used was the straight line with parabolic roll-off discussed in Section 5.1.5.

In Figures 6.1, 6.2 and 6.3 the on-resonance M_{BC} distributions for B decay to one, two and three pion light meson states are shown. In each plot, the fixed width Gaussian and the background function are superimposed on the M_{BC} distributions. The amount of background observed in each mode is commensurate with the multiplicity of the events given a fixed number of cuts. As an example, the significant reduction of background levels for modes which decay to a vector charm meson is due to the $m_{D^*} - m_D$ cut which takes advantage of the small q^2 in $D^* \to D\pi$ decay.

The branching fraction results for all the non color-suppressed modes are given in Tables 6.1 through 6.3. Three values were determined for each decay mode that included a D^0 in the decay chain, one for each of the D^0 subchannels. For these modes the values were averaged, weighted by their statistical errors. Two systematic errors are quoted for the averaged results. The second error, the first systematic error, was calculated by adding in quadrature the following quantities: the background errors established as described in section 5.1.6, the error due to Monte Carlo statistics, typically less than 2%, and the uncertainty in detection efficiencies or tracking errors. Uncertainties in detection efficiencies for charged tracks with momenta greater than 225 MeV are within $\pm 2.0\%$ of the measured efficiency. For charged tracks with momenta below 225 MeV, the uncertainty increases to $\pm 5.0\%$. For neutral pions the uncertainty is $\pm 5.0\%$. These errors were assigned to all the final states particle in the decay chain. The errors for charged tracks were summed linearly and the result was added,

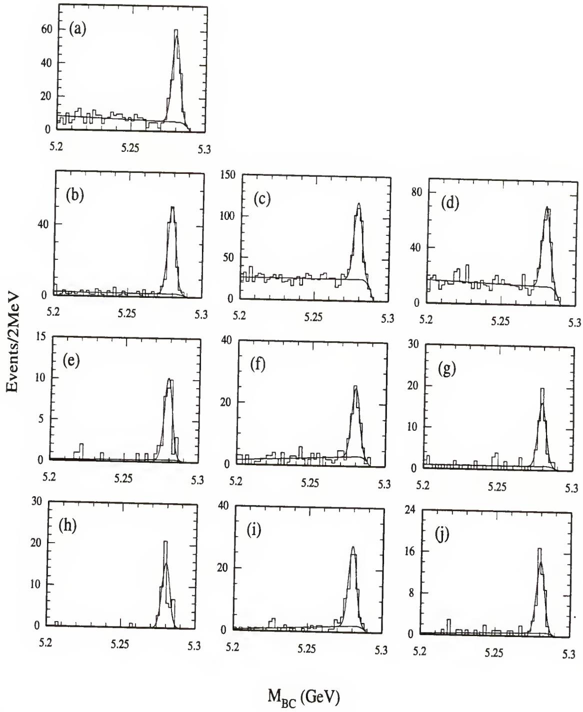

Figure 6.1 M_{BC} distributions for the $B \to D^{(*)}\pi^-$ modes.

In (a) the $B^0 \to D^+\pi^-$ in the D^+ decay mode $D^+ \to K^-\pi^+\pi^+$. In (b) through (d) the $B^- \to D^0\pi^-$ in the D^0 decay modes $K^-\pi^+$, $K^-\pi^+\pi^0$ and $K^-\pi^+\pi^-\pi^+$ respectively. In (e) through (g) the $B^- \to D^{*0}\pi^-$ in the D^0 decay modes $K^-\pi^+$, $K^-\pi^+\pi^0$ and $K^-\pi^+\pi^-\pi^+$. In (h) through (j) the $B^0 \to D^{*+}\pi^-$ in the D^0 decay modes $K^-\pi^+$, $K^-\pi^+\pi^0$ and $K^-\pi^+\pi^-\pi^+$.

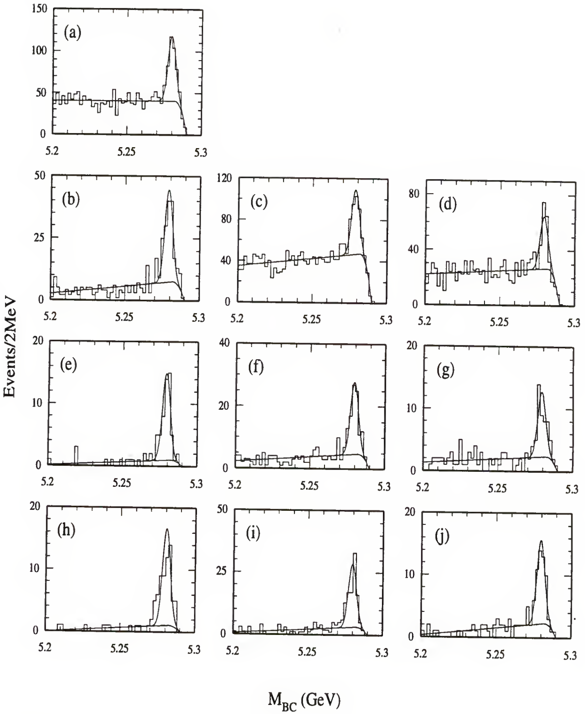

Figure 6.2 M_{BC} distributions for the $B \to D^{(*)}\rho^-$ modes.

In (a) the $B^0 \to D^+\rho^-$ in the D^+ decay mode $D^+ \to K^-\pi^+\pi^+$. In (b) through (d) the $B^- \to D^0\rho^-$ in the D^0 decay modes $K^-\pi^+$, $K^-\pi^+\pi^0$ and $K^-\pi^+\pi^-\pi^+$ respectively. In (e) through (g) the $B^- \to D^{*0}\rho^-$ in the D^0 decay modes $K^-\pi^+$, $K^-\pi^+\pi^0$ and $K^-\pi^+\pi^-\pi^+$. In (h) through (j) the $B^0 \to D^{*+}\rho^-$ in the D^0 decay modes $K^-\pi^+$, $K^-\pi^+\pi^0$ and $K^-\pi^+\pi^-\pi^+$.

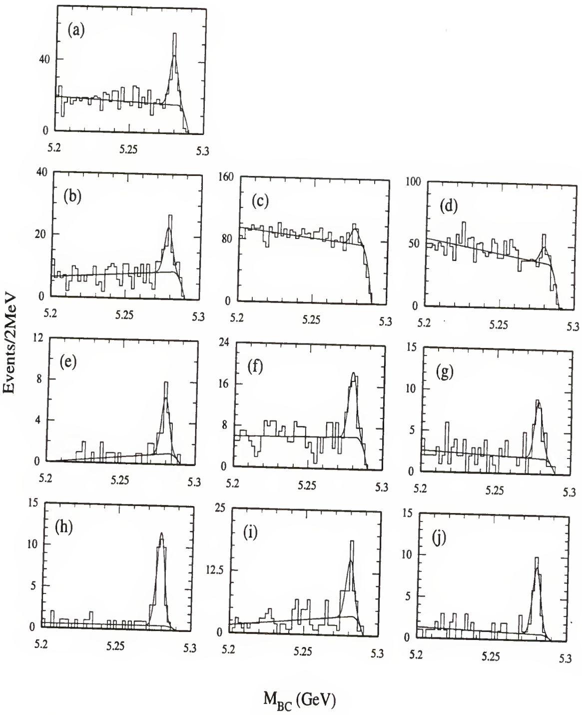

Figure 6.3 M_{BC} distributions for the $B \to D^{(*)} a_1^-$ modes.

In (a) the $B^0 \to D^+ a_1^-$ in the D^+ decay mode $D^+ \to K^-\pi^+\pi^+$. In (b) through (d) the $B^- \to D^0 a_1^-$ in the D^0 decay modes $K^-\pi^+$, $K^-\pi^+\pi^0$ and $K^-\pi^+\pi^-\pi^+$ respectively. In (e) through (g) the $B^- \to D^{*0} a_1^-$ in the D^0 decay modes $K^-\pi^+$, $K^-\pi^+\pi^0$ and $K^-\pi^+\pi^-\pi^+$. In (h) through (j) the $B^0 \to D^{*+} a_1^-$ in the D^0 decay modes $K^-\pi^+$, $K^-\pi^+\pi^0$ and $K^-\pi^+\pi^-\pi^+$.

Table 6.1

Table of branching fractions $B \to D^{(*)}\pi^-$ decays

B Mode	D Mode	Yield	$\epsilon_{mc}(\%)$	$\mathcal{B}(\%)$	$\mathcal{B}(\%)$ average
$D^+\pi^-$	$K^-\pi^+\pi^+$	170	27.6	0.308 ± 0.025	$0.308 \pm 0.026 \pm 0.028 \pm 0.031$
$D^{*+}\pi^-$	$K^-\pi^+$	52	31.0	0.287 ± 0.041	$0.304 \pm 0.024 \pm 0.025 \pm 0.027$
	$K^-\pi^+\pi^0$	85	12.3	0.314 ± 0.047	
	$K^-\pi^+\pi^-\pi^+$	46	12.2	0.313 ± 0.050	
$D^0\pi^-$	$K^-\pi^+$	162	38.3	0.496 ± 0.042	$0.534 \pm 0.025 \pm 0.033 \pm 0.047$
	$K^-\pi^+\pi^0$	306	17.4	0.544 ± 0.052	
	$K^-\pi^+\pi^-\pi^+$	194	19.1	0.580 ± 0.052	
$D^{*0}\pi^-$	$K^-\pi^+$	33	14.1	0.429 ± 0.081	$0.497 \pm 0.044 \pm 0.048 \pm 0.057$
	$K^-\pi^+\pi^0$	73	7.5	0.475 ± 0.079	
	$K^-\pi^+\pi^-\pi^+$	51	7.0	0.654 ± 0.101	

Table 6.2

Table of branching fractions $B \to D^{(*)}\rho^-$ decays

B Mode	D Mode	Yield	$\epsilon_{mc}(\%)$	$\mathcal{B}(\%)$	$\mathcal{B}(\%)$ average
$D^+\rho^-$	$K^-\pi^+\pi^+$	171	9.9	0.861 ± 0.078	$0.861 \pm 0.078 \pm 0.109 \pm 0.086$
$D^{*+}\rho^-$	$K^-\pi^+$	51	10.8	0.816 ± 0.125	$0.844 \pm 0.071 \pm 0.096 \pm 0.076$
	$K^-\pi^+\pi^0$	84	4.2	0.897 ± 0.110	
	$K^-\pi^+\pi^-\pi^+$	44	4.7	0.794 ± 0.137	
$D^0\rho^-$	$K^-\pi^+$	123	14.1	1.081 ± 0.116	$1.022 \pm 0.067 \pm 0.109 \pm 0.086$
	$K^-\pi^+\pi^0$	206	6.8	0.934 ± 0.099	
	$K^-\pi^+\pi^-\pi^+$	126	6.9	1.119 ± 0.146	
$D^{*0}\rho^-$	$K^-\pi^+$	46	5.6	1.508 ± 0.240	$1.444 \pm 0.134 \pm 0.188 \pm 0.161$
	$K^-\pi^+\pi^0$	76	2.5	1.498 ± 0.204	
	$K^-\pi^+\pi^-\pi^+$	35	2.4	1.275 ± 0.265	

Table 6.3

Table of branching fractions $B \to D^{(*)} a_1^-$ decays

B Mode	D Mode	Yield	$\epsilon_{mc}(\%)$	$\mathcal{B}(\%)$	$\mathcal{B}(\%)$ average
$D^+ a_1^-$	$K^-\pi^+\pi^+$	92	9.1	0.757 ± 0.065	$0.757 \pm 0.065 \pm 0.116 \pm 0.076$
$D^{*+} a_1^-$	$K^+\pi^-$	37	8.3	1.569 ± 0.270	$1.205 \pm 0.140 \pm 0.138 \pm 0.098$
	$K^-\pi^+\pi^0$	37	3.8	0.921 ± 0.192	
	$K^-\pi^+\pi^-\pi^+$	27	3.1	1.461 ± 0.309	
$D^0 a_1^-$	$K^+\pi^-$	47	12.9	0.812 ± 0.215	$0.812 \pm 0.215 \pm 0.151 \pm 0.022$
	$K^-\pi^+\pi^0$	66	6.0	0.641 ± 0.198	
	$K^-\pi^+\pi^-\pi^+$	44	6.4	0.740 ± 0.241	
$D^{*0} a_1^-$	$K^+\pi^-$	18	4.0	1.685 ± 0.453	$1.898 \pm 0.268 \pm 0.236 \pm 0.221$
	$K^-\pi^+\pi^0$	42	1.9	2.132 ± 0.454	
	$K^-\pi^+\pi^-\pi^+$	23	2.2	1.874 ± 0.487	

in quadrature, to the total neutral pion uncertainty. the second systematic error includes the uncertainties in the D and D^* branching fractions.

In Figure 6.4 the branching fractions are grouped to show the measurement variations within each B meson decay containing a D^0. The variations between the measurements all fall well within 2.0 standard deviations of the statistical errors

In all three $B^- \to D^0\rho^-$ modes, (Figure 6.2 b-d) the background levels in the M_{BC} distributions are considerable. To insure that the large background did not significantly affect the measurements, we recalculated the branching fractions using only the half of the ρ^- helicity range which corresponds to the fast π^0, ρ^- decay daughter. This cut removed a significant amount of background including the background associated with $B^- \to D^{*0}\pi^-$ with $D^{*0} \to D^0\gamma$ which forms a broad peak in the signal region (see Section 5.1.1). The $B^- \to D^0\rho^-$ M_{BC} distributions with the slow π^0 veto are shown in Figure 6.5. The branching fractions obtained by fitting these distributions gave values consistent with the values obtained with the full helicity range. The values were found to differ by less than 0.4σ, where σ denotes the statistical error (see Figure 6.4 (e)).

For the $B^- \to D^0 a_1^-$ decays, only the $D^0 \to K^-\pi^+$ mode is used in determining the branching fraction. The statistical significance of $D^0 \to K^-\pi^+$ submode is 4.7σ compared to less than 3.0σ for the $D^0 \to K^-\pi^+\pi^0$ and $D^0 \to K^-\pi^+\pi^-\pi^+$ channels. In addition, the large background levels found in the $D^0 \to K^-\pi^+\pi^0$ and $D^0 \to K^-\pi^+\pi^-\pi^+$ modes would lead to large uncertainties in the shape of the background function and would further reduce the significance of the signal.

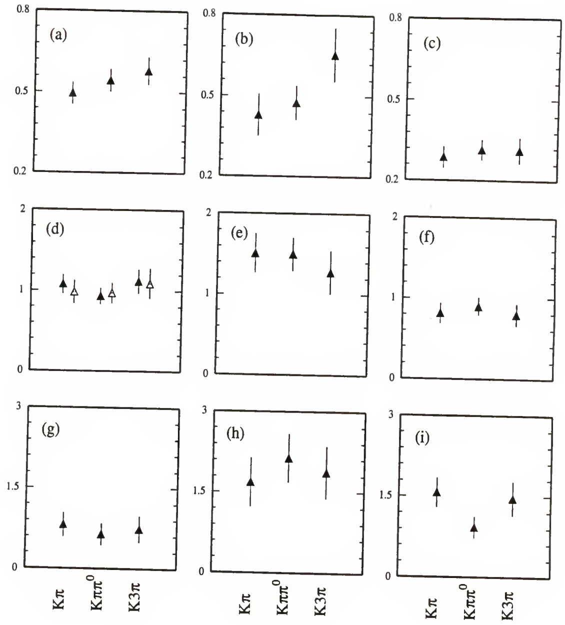

Figure 6.4 Plots of the B branching fractions with all three D^0 submodes. In (a) the $B^- \to D^0\pi^-$ modes, in (b) the $B^- \to D^{*0}\pi^-$ modes, in (c) the $\bar{B}^0 \to D^{*+}\pi^-$ modes, in (d) the $B^- \to D^0\rho^-$ modes with the full helicity (filled triangles), and half the helicity (open triangles), in (e) the $\bar{B}^0 \to D^{*+}\rho^-$ modes, in (g-i) the $B^- \to D^0 a_1^-$, the $B^- \to D^{*0}a_1^-$ and the $\bar{B}^0 \to D^{*+}a_1^-$ respectively. The error bars correspond to the 1σ statistical error

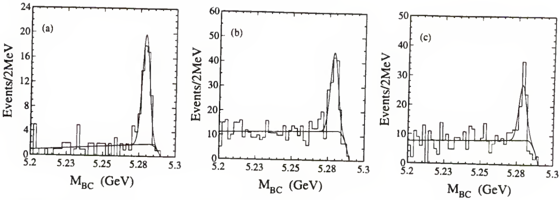

Figure 6.5 M_{BC} spectrum for $B^- \to D^0\rho^-$ after application of helicity cut. In (a) the $D^0 \to K^-\pi^+$, in (b) the $D^0 \to K^-\pi^+\pi^0$ and in (c) the $D^0 \to K^-\pi^+\pi^-\pi^+$ modes.

6.1.2 Decays to Color-Suppressed Modes

Clear signals were not observed for any of the color-suppressed M_{BC} distributions investigated. The lack of a prominent enhancement prevented us from extracting branching fractions and thus only upper limits were calculated for each color-suppressed B decay channel. To simplify the analysis and to insure that the upper limits obtained do not underestimate the branching fractions, the yields were measured for the sum of the three D^0 subdecays in each B meson decay mode.

To find the upper limit on the number of events, the M_{BC} distributions were fit to a Gaussian of fixed width plus the background function described in Section 5.1.5, but with additional requirements imposed on the function parameters. The mean of the Gaussian was fixed to 5.28 GeV and the slope of the CLEO background function was fixed to zero. Also, the offset of the background function (see Equation (5.2)) was varied to insure that the upper limit on the number of events obtained the most conservative value. The upper limits on the number of events observed together with Monte Carlo efficiencies

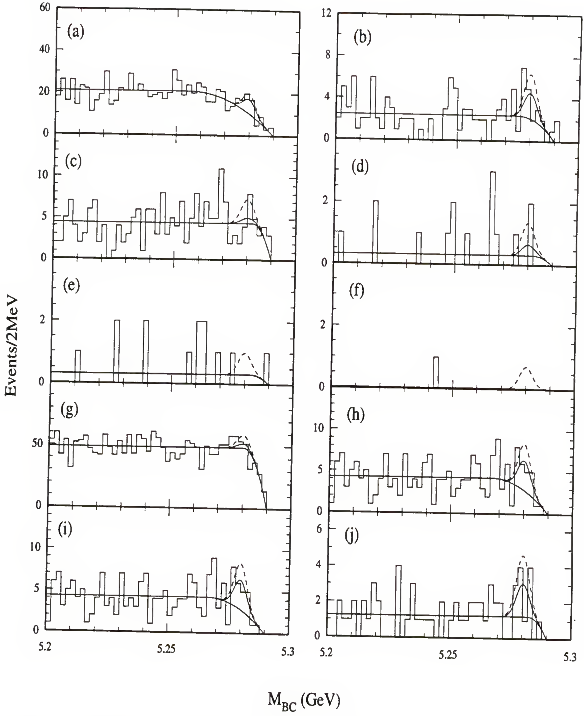

Figure 6.6 M$_{BC}$ spectra for color-suppressed B decays, D^0 modes combined.

In (a) the $\bar{B}^0 \to D^0\pi^0$ mode, in (c) the $\bar{B}^0 \to D^{*0}\pi^0$, in (c) the $\bar{B}^0 \to D^0\eta$, in (d) the $\bar{B}^0 \to D^{*0}\eta$, in (e) the $\bar{B}^0 \to D^0\eta'$, in (f) the $\bar{B}^0 \to D^{*0}\eta'$, in (g) the $\bar{B}^0 \to D^0\rho^0$, in (h) the $\bar{B}^0 \to D^{*0}\rho^0$, in (i) the $\bar{B}^0 \to D^0\omega$ and in (j) the $\bar{B}^0 \to D^{*0}\omega$.

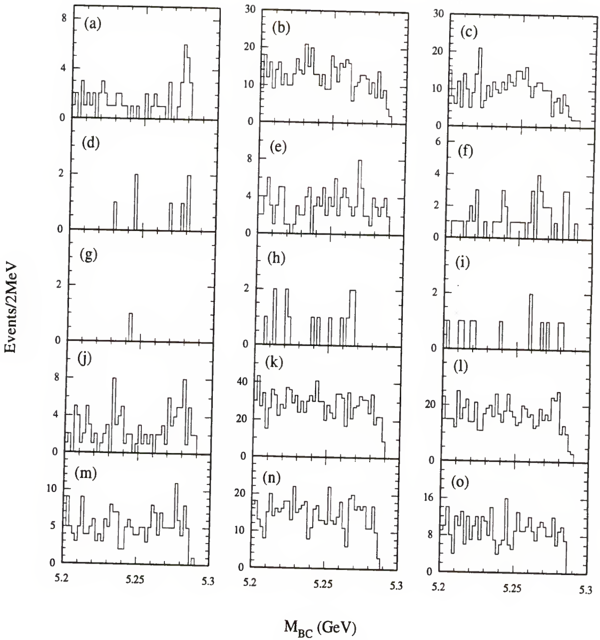

Figure 6.7 M_{BC} spectra for color-suppressed $B \to D^0 h^0$.

Each row corresponds to a different B decay mode, In (a-c) the three $\bar{B}^0 \to D^0\pi^0$ modes, in (d-f) the $\bar{B}^0 \to D^0\eta$ modes, in (g-i) the $\bar{B}^0 \to D^0\eta'$ decay modes, in (j-l) the $\bar{B}^0 \to D^0\rho^0$ and in (m-o) the $B^0 \to D^0\omega$. The columns correspond to different D^0 decay modes, from left to right the $D^0 \to K^-\pi^+$, $D^0 \to K^-\pi^+\pi^0$, and the $D^0 \to K^-\pi^+\pi^-\pi^+$.

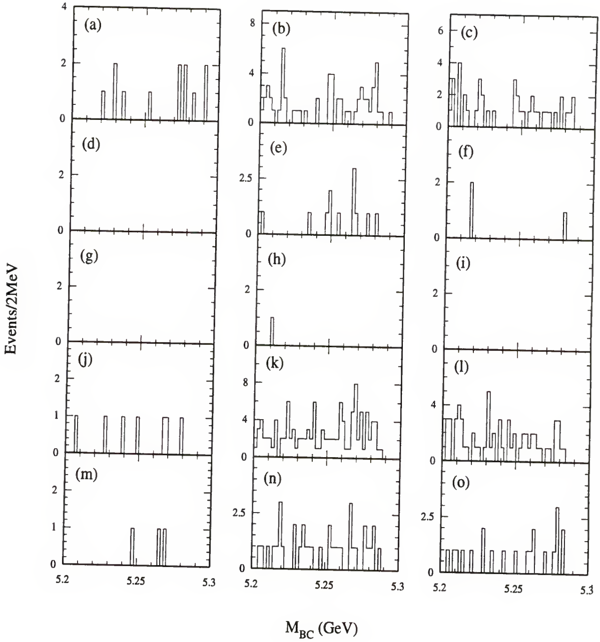

Figure 6.8 M_{BC} spectra for color-suppressed $B \to D^{*0}h^0$.

Each row corresponds to a different B decay mode, In (a-c) the three $\bar{B}^0 \to D^{*0}\pi^0$ modes, in (d-f) the $\bar{B}^0 \to D^{*0}\eta$ modes, in (g-i) the $\bar{B}^0 \to D^{*0}\eta'$ decay modes, in (j-l) the $\bar{B}^0 \to D^{*0}\rho^0$ and in (m-o) the $B^0 \to D^{*0}\omega$. The columns correspond to different D^{*0}decay modes, from left to right the $D^0 \to K^-\pi^+$, $D^0 \to K^-\pi^+\pi^0$, and the $D^0 \to K^-\pi^+\pi^-\pi^+$.

Table 6.4

Table of branching fractions for color-suppressed decays

Decay Mode	N$_{\text{obs}}$	$\epsilon_{mc}(\%)$	$\mathcal{B}$ (%) at 90% C.L.
$\bar{B}^0 \to D^0\pi^0$	< 33.3	$29.2, 15.3, 15.8$	< 0.033
$\bar{B}^0 \to D^0\eta$	< 9.4	$26.6, 9.7, 13.1$	< 0.033
$\bar{B}^0 \to D^0\eta'$	< 2.3	$13.6, 6.9, 8.4$	< 0.029
$\bar{B}^0 \to D^0\rho^0$	< 33.7	$19.0, 7.0, 10.9$	< 0.060
$\bar{B}^0 \to D^0\omega$	< 13.0	$11.0, 3.2, 3.9$	< 0.057
$\bar{B}^0 \to D^{*0}\pi^0$	< 14.6	$12.2, 6.5, 6.6$	< 0.055
$\bar{B}^0 \to D^{*0}\eta$	< 3.6	$9.6, 4.1, 4.9$	< 0.050
$\bar{B}^0 \to D^{*0}\eta'$	< 2.3	$5.6, 2.3, 2.5$	< 0.13
$\bar{B}^0 \to D^{*0}\rho^0$	< 19.1	$7.4, 4.0, 3.6$	< 0.12
$\bar{B}^0 \to D^{*0}\omega$	< 11.8	$5.1, 2.6, 2.7$	< 0.12

for each D^0 submode and the upper limits on the branching fraction are listed in Table 6.4. The M$_{\text{BC}}$ distribution for the color-suppressed modes, with all three D^0 submodes combined are shown Figure 6.6. In each plot both the fit (solid line) to the M$_{\text{BC}}$ distribution and the fit with the upper limit, at the 90% confidence level, (dashed line) are superimposed. In Figures 6.7 and 6.8 the distribution of each color-suppressed B decay mode are separated into the three D^0 subdecays.

The upper limit for the branching fractions were determined by a modified version of Equation (6.1),

$$\mathcal{B}_b = \frac{\text{N}_{\text{obs}}}{\text{N}_{B\bar{B}} \cdot (\sum_{i=1}^{3} \epsilon_{mc_{b_i}} \cdot \mathcal{B}_{D_i}) \cdot \prod_{d,d\neq i} \mathcal{B}_d}. \tag{6.2}$$

where the value of N_{obs} is now the upper limit on the number of events summed over the three D^0 subdecays and the Monte Carlo efficiency term is replaced by the sum of the efficiencies times D^0 branching fractions. The upper limits were determined by the method described in section III of the Particle Data Group [2].

While no clear signals were obtained for any of the M_{BC} distributions, Figure 6.7 (a) shows a significant enhancement in the signal region of the $D^0 \to K^-\pi^+$ submode in the $\bar{B}^0 \to D^0\pi^0$ channel. Since signals were not obtained in either the $D^0 \to K^-\pi^+$ nor the $D^0 \to K^-\pi^+\pi^-\pi^+$ modes we scrutinized the events in all three modes for possible errors in the event reconstruction procedure. No obvious errors were found, however we did find that in the $D^0 \to K^-\pi^+$ mode approximately 18% of the events in the signal region were double counted events. Double counting occurs when the daughters of the D^0, the $K^-\pi^+$, are misidentified as π^- K^+ and reconstruct to a $\bar{D}^0$. The misidentified $\bar{D}^0$ is then combined with the same π^0 used to reconstruction the B^0 and thus the event is counted twice. The double counting does not significantly alter the final answer since the Monte Carlo efficiencies are affected in exactly the same way. If the double counted events are removed from the plot there is still a significant excess in the signal region which cannot be accounted for by either the continuum background Figure 5.25 (a) nor the known $B\bar{B}$ background shown in Figure 5.23 (a). Further work on this mode is in progress.

6.2 Measurement of Polarization

Fully reconstructed B decays were used to measure the polarizations of the final states in $B^- \to D^{*0}\rho^-$ and $\bar{B}^0 \to D^{*+}\rho^-$ decays. The fractional polarization of the $D^{*+}\rho^-$ in $\bar{B}^0 \to D^{*+}\rho^-$ decays provides information in tests of factorization. The polarization of $D^{*0}\rho^-$ in $B^- \to D^{*0}\rho^-$ provides for information on the relative sign and magnitude of a_2/a_1 [50].

The longitudinal polarization measurements were obtained by fitting the cosine of the helicity distributions with a functional form derived from the differential decay widths. The helicity angle (see Section 4.6) is the angle one of the daughters of the vector parent makes with the direction of the vector particle in the B's rest-frame as measured in the vector's rest-frame. The differential decay width expressed as a function of helicity angles Θ_{D^*} and Θ_ρ, and after integrating over χ is

$$\frac{d^2\Gamma}{d\cos\Theta_{D^*}d\cos\Theta_\rho} \propto \frac{1}{4}\sin^2\Theta_{D^*}\sin^2\Theta_\rho(|H_{+1}|^2+|H_{-1}|^2)+\cos^2\Theta_{D^*}\cos^2\Theta_\rho|H_0|^2. \tag{6.3}$$

where χ is the angle between the normal to the D^* and ρ decay planes and $H_{\pm 1}$ and H_0 are the transverse and longitudinal helicity amplitudes [45].

Completely polarization, in the longitudinal direction, would result in a $\cos^2\Theta_h$ distributions for both the D^* and the ρ^-. Complete transverse polarization would result in $\sin^2\Theta_h$ distributions. To allow for both possibilities we fit the $\cos\Theta_h$ distributions to

$$N\{\cos^2\Theta_h + \frac{\Gamma_L}{2\Gamma}(1 - 3\cos^2\Theta_h)\} \tag{6.4}$$

where N and Γ_L/Γ are free parameters in the fit.

To measure the polarization states of the decay products of the B meson, the cosine of helicity distributions were formed by selecting events in the signal region of the M_{BC} spectrum defined to be between 5.272 GeV and 5.288 GeV.

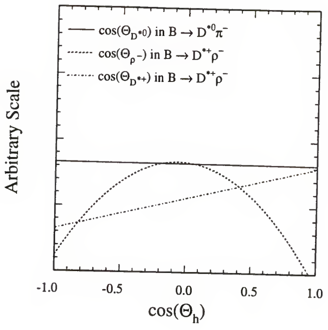

Figure 6.9 Detection efficiencies verses $\cos(\Theta_h)$.

These distributions were then background subtracted and efficiency corrected to insure that the cosine of helicity distribution was representative of true signal events. The background events were taken from the M_{BC} side band defined to be between 5.2 GeV and 5.26 GeV. The background distribution was then scaled and subtracted from the signal distribution. The efficiency correction was performed to compensate for the differences in detector acceptance for final states which occupy different regions of the allowed phase space.

To correct for the difference in detector acceptances we measured the efficiencies as a function of helicity angle in Monte Carlo generated with the final states unpolarized. Figure 6.9 shows the efficiencies as a function of $\cos\Theta_h$ for the three types of final states considered. For the D^{*+}, the efficiency drop in the region of the plot near $\cos\Theta_h = -1$ (dot-dashed line) is due to the momentum dependent detector losses for low momentum tracks. For the ρ^-, the drop in the efficiency curve (dashed line) in the region near $\cos\Theta_h = -1$ can also be ascribed to detector losses for charged tracks with low momentum. The drop in the ρ^- efficiency, in the region near $\cos\Theta_h = +1$ is due to the photon energy cut-off which reduces the acceptance for low energy π^0s. Neutral pions from D^{*0} decays, unlike those produced in ρ^- decays, are produced with a relatively small momentum spread which explains the nearly flat efficiency curve (solid line) of the D^{*0}.

The efficiency, background subtracted helicity distribution was fit to Equation (6.4). The results are shown in Figure 6.10 for both the $B^- \to D^{*0}\rho^-$ and the $\bar{B}^0 \to D^{*+}\rho^-$ modes. All three D^0 subdecays are combined in these plots. The measured fraction of longitudinally polarized ρ^- and D^{*0} in the decay $B^- \to D^{*0}\rho^-$ decay are $\Gamma_L/\Gamma = 86.7 \pm 6.7 \pm 4.4\%$ and $\Gamma_L/\Gamma = 81.2 \pm 7.4 \pm 4.1\%$ respectively. In the $\bar{B}^0 \to D^{*+}\rho^-$ mode the fraction of longitudinally polarized ρ^- and D^{*+} is $\Gamma_L/\Gamma = 91.5 \pm 4.9 \pm 4.6\%$ and $\Gamma_L/\Gamma = 88.2 \pm 5.4 \pm 4.4\%$ respectively. In order to reduced the statistical errors a binned two dimensional χ^2 fit to the joint $(\cos\Theta_{D^*}, \cos\Theta_\rho)$ distributions was performed. This methods yields $\Gamma_L/\Gamma = 84.2 \pm 5.1 \pm 4.2\%$ for the $B^- \to D^{*0}\rho^-$ mode and $\Gamma_L/\Gamma = 90.0 \pm 3.7 \pm 4.5\%$ for the $\bar{B}^0 \to D^{*+}\rho^-$ mode. The systematic error was estimated by varying the efficiency correction and background subtraction scheme.

To verify the efficiency correction and background subtraction scheme, the same method was used to extract the polarization of the D^* in $B^- \to D^{*0}\pi^-$ and $\bar{B}^0 \to D^{*+}\pi^-$ decays. If the procedure is reliable it will find 100% of the

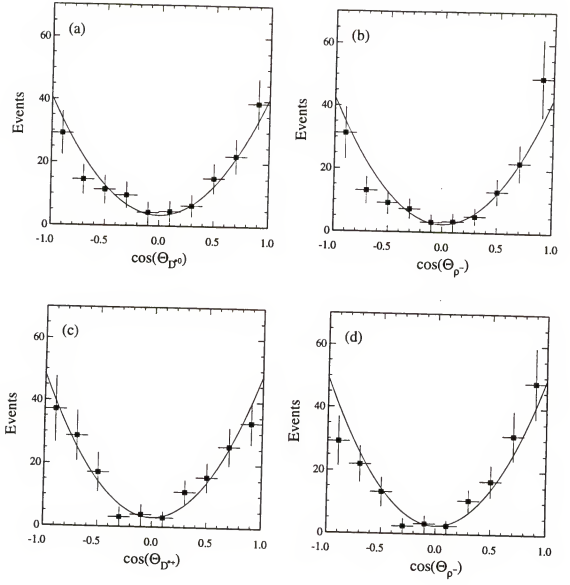

Figure 6.10 Plots of polarization in $B \to D^{*+}\rho^-$ modes.

The background subtracted efficiency corrected $\cos\Theta_h$ distributions of (a) the D^{*0} and (b) the ρ^-, in $B^- \to D^{*0}\rho^-$ decays. In (c) the D^{*+} and in (d) the ρ^- distribution in the $\bar{B}^0 \to D^{*+}\rho^-$ decays.

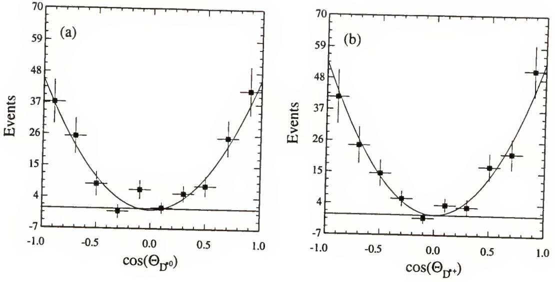

Figure 6.11 Plots of polarization in $B \to D^{*0}\rho^-$ modes.

The background subtracted efficiency corrected $\cos\Theta_h$ distributions of (a) the $D^{*0}$and (b) D^{*+}, in the $B^- \to D^{*0}\pi^-$ and $\bar{B}^0 \to D^{*+}\pi^-$ decay modes, respectively.

D^*s longitudinally polarized as required by conservation of angular momentum. The fitted distributions are shown in Figure 6.11. The fits yield $\Gamma_L/\Gamma = 102.3\pm$ 6.0% for the $B^- \to D^{*0}\pi^-$ and $\Gamma_L/\Gamma = 99.8\pm4.6\%$ for the $\bar{B}^0 \to D^{*+}\pi^-$ mode. Both results are consistent with 100% polarization.

6.3 Tests of Factorization

In Chapter 2 we introduced the factorization hypothesis which asserts that amplitudes in decays that proceed through spectator diagrams can be factorized into two independent matrix elements, each governing a separate transition. In class I decays the amplitude factorizes into a $B \to D$ transition and a transition from the vacuum to a light meson. To test the factorization hypothesis nonleptonic class I decays were compared directly to semileptonic decays,

Table 6.5

Table of constants used for test of factorization

Constants		Model	$d\Gamma(B\to D^*l\nu)/dq^2$ (GeV^{-2}) $q^2=m_\pi^2$	$q^2=m_\rho^2$	$q^2=m_{a_1}^2$
a_1	1.12 ± 0.10	BSW	0.0023	0.0025	0.0032
f_π	131.74 ± 0.15 MeV	ISGW	0.0020	0.0024	0.0030
f_ρ	224 ± 1 MeV	KS	0.0024	0.0027	0.0033
f_{a_1}	298 ± 8 MeV				

at the appropriate q^2. Similarly, a comparison between the polarization in nonleptonic class I decays and semileptonic decays, at fixed q^2, were used as a further test of factorization.

6.3.1 Branching Ratio Test

If factorization holds then the effective Hamiltonian described in Chapter 2 can be used to write down the amplitude for a nonleptonic decay process as the product of two independent matrix elements. In the factorization hypothesis the amplitude is given by

$$A^0=\frac{G_F}{\sqrt{2}}V_{cb}V_{ud}^*\,a_1\langle h^-|\bar{d}\gamma_\mu(1-\gamma_5)u|0\rangle\langle D^{*+}|\bar{c}\gamma^\mu(1-\gamma_5)b|\bar{B}^0\rangle \qquad (6.5)$$

where the operators come from the factorized current-current effective Hamiltonian (Equation (2.15)). The h^- here represents a light meson, either a π,ρ or a_1.

To test factorization we need to experimentally verify that the relation

$$\frac{\Gamma\left(\bar{B}^0\to D^{*+}h^-\right)}{\frac{d\Gamma}{dq^2}\left(\bar{B}^0\to D^{*+}l^-\bar{\nu}_l\right)\Big|_{q^2=m_h^2}}=6\pi^2a_1^2f_\pi^2|V_{ud}|^2 \qquad (6.6)$$

is satisfied. Here q^2 is the mass squared of the lepton-neutrino system and is set to the mass of the of the light mesons to insure that kinematics properties in both systems match.

In order to verify Equation (6.6) we need to evaluate the expression on the right-hand side (R_{th}). The ingredients that go into R_{th} are listed in Table 6.5. The QCD constant a_1 can be obtained, in the factorization approximation, from perturbative QCD (see Equation (2.16),(2.14) and (2.12)). The error in a_1 reflects the uncertainty in the mass scale at which the coefficients C_1 and C_2 were evaluated. The value of $V_{ud} = 0.975 \pm 0.001$ was used.

The values of the decay constants come from a variety of sources. The pion decay constant is obtained from pion decay, and together with the values for the f_ρ and f_{a_1}, are listed in Table 6.5. The decay constant f_ρ can be determined from either $e^+e^- \to \rho^0$ or from τ decays. The first method leads to $f_\rho = 215 \pm 4$ MeV. The second method involves extracting the value of f_ρ from the rate $\Gamma(\tau^- \to \nu_\tau \rho^-)$. The value of f_{a_1} can be similarly obtained through the decay process $\tau^- \to \nu_\tau a_1^-$. A determination of both f_ρ and f_{a_1} has been recently performed in Ref. [51]. The new results are more precise than previous values and are used in this analysis [45].

To evaluate the expression on the right-hand side of Equation (6.6), (R_{exp}), we need to find the differential branching fraction of the semileptonic decay. To do so we must interpolate the results from the observed differential q^2 distribution. In Figure 6.12 the q^2 distribution of $\bar{B}^0 \to D^{*+} l^- \bar{\nu}_l$ is shown. The data are weighted averages of CLEO and ARGUS results and the fits are to the three theoretical models listed in the plot [52]. Since the distribution is poorly measured in the q^2 range of interest ($0 < q^2 < 1.6$ GeV^2) we must rely

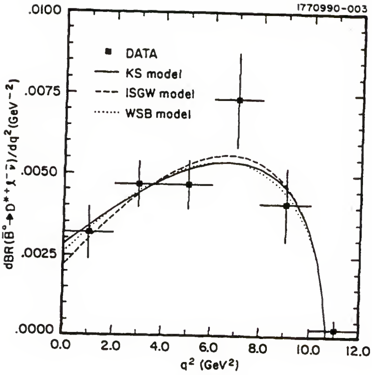

Figure 6.12 The q^2 distribution for $\bar{B}^0 \to D^{*+} l^- \bar{\nu}_l$.

on the theoretical models to determine the semileptonic branching fractions at $q^2 = m_\pi^2, m_\rho^2$ and $m_{a_1}^2$. The spread in the theoretical models is small so we use the prediction of WSB in our comparison. The values obtained at each q^2 are also listed in Table 6.5.

We now have all the necessary ingredients to perform the test of factorization. In Table 6.6 the comparison of the data in the three available q^2 regions are shown. The error in R_{exp} is taken solely from the error in the $\bar{B}^0 \to D^{*+} h^-$ branching fraction. The error in R_{th} is dominated by theoretical uncertainties in a_1. From these measurements we find that at present levels of precision

Table 6.6

Table of constants used for test of factorization

q^2 region	R_{exp} (GeV^2)	R_{th} (GeV^2)
$\bar{B} \to D^{*+}\pi^-$	$1.3 \pm 0.1 \pm 0.2$	1.2 ± 0.2
$\bar{B} \to D^{*+}\rho^-$	$3.4 \pm 0.3 \pm 0.5$	3.3 ± 0.5
$\bar{B} \to D^{*+}a_1^-$	$3.8 \pm 0.4 \pm 0.5$	3.0 ± 0.5

there is good agreement between the experimental results and the expectation from factorization in the q^2 range $0 < q^2 < m_{a_1}^2$.

6.3.2 Polarization Test

As suggested by Körner and Goldstein [53], more subtle test of factorization can be performed by comparing the final state polarization in hadronic two body decays to polarization in semileptonic decays at fixed q^2. For instance, the ratio of longitudinal to transverse polarization (Γ_L/Γ_T) in $\bar{B}^0 \to D^{*+}\rho^-$ should equal the polarization ratio in the semileptonic decay at $q^2 = m_\rho^2 = 0.6$ GeV^2,

$$\frac{\Gamma_L}{\Gamma_T}(\bar{B}^0 \to D^{*+}\rho^-) = \frac{\Gamma_L}{\Gamma_T}(\bar{B}^0 \to D^{*+}l^-\bar{\nu}_L)|_{q^2=m_\rho^2}. \tag{6.7}$$

This method has the added advantage that the QCD coefficient a_1 does not enter the comparison [45]. This coefficient contributes a sizeable uncertainty to the branching fraction test as shown in the previous section.

There are simple physical arguments which describe the polarization of the final states in semileptonic decays. At low q^2 the longitudinal polarization dominates. Here the D^* has the maximum possible momentum and the lepton neutrino pair travel collinearly in the opposite direction with their spins aligned

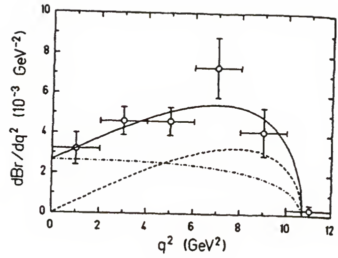

Figure 6.13 Polarization components of q^2 distribution $\bar{B}^0 \to D^{*+}l^-\bar{\nu}_l$.

to conserve angular momentum. This causes the D^* to be longitudinally polarized. As $q^2 \to q^2_{\mathrm{max}}$ we expect that all three polarizations are equally likely since the D^* is almost at rest and its small residual momentum will equally populate the three polarization states. Here we expect $\Gamma_L/\Gamma_T = 1/2$ and thus transverse polarization dominates as $q^2 \to q^2_{\mathrm{max}}$.

From these simple arguments Rosner predicts 88% longitudinal polarization for $\bar{B}^0 \to D^{*+}l^-\nu$ at $q^2 = m_\rho$ [54]. Neubert predicts similar results [55]. Figure 6.13 shows Neubert's results for the production of transversely and longitudinally polarized D^{*+} in $\bar{B}^0 \to D^{*+}l^-\nu$ decays for the whole q^2 range. The dashed solid curve is the fit to data, the dashed curve is the component due to transversely polarized D^*s and the dot-dashed curve is the prediction for longitudinally polarized D^*s. The data are weighted averages of CLEO and

Table 6.7

Table of ratios of color-suppressed branching fractions.

Modes	Ratio of $\mathcal{B}$
$\mathcal{B}(D^0 \to K^0\pi^0)/\mathcal{B}(D^0 \to K^-\pi^+)$	0.57 ± 0.13
$\mathcal{B}(D^0 \to \bar{K}^{*0}\pi^0)/\mathcal{B}(D^0 \to K^{*-}\pi^+)$	0.47 ± 0.23
$\mathcal{B}(D^0 \to \pi^0\pi^0)/\mathcal{B}(D^0 \to \pi^-\pi^+)$	0.77 ± 0.25
$\mathcal{B}(D_s^+ \to \bar{K}^{*0}K^+)/\mathcal{B}(D_s \to \phi\pi^+)$	0.95 ± 0.10
$\mathcal{B}(D_s^+ \to \bar{K}^0K^+)/\mathcal{B}(D_s \to \phi\pi^+)$	1.01 ± 0.16

ARGUS results. The solid line, at $q^2 = m_\rho^2$, gives $\Gamma_L/\Gamma = 85\%$ which is in good agreement with the measured result,

$$\Gamma_L/\Gamma = 90 \pm 3.7 \pm 4.5\%$$

from Section 6.2. This also supports the factorization hypothesis since the comparison reveals similar results for both the nonleptonic and semileptonic decays.

6.4 Determination $|a_1|, |a_2|$ and the Relative Sign of a_2/a_1

Important information on factorization and the contribution to the amplitude from non-factorizable terms can be obtained by finding the values of the parameters a_1 and a_2. In the factorization hypothesis the amplitude for a particular spectator decay process is written in terms of these parameters and factorized hadronic matrix elements. The parameters a_1 and a_2 are defined as

$$a_1 = c_1 + \xi c_2$$

$$a_2 = c_2 + \xi c_1$$

where $\xi = \frac{1}{N_c}$ and a_1 and a_2 are related to the scale dependent Wilson coefficients calculable from perturbative QCD.

In charm data the factorization approach outlined in Chapter 2 does not explain the bulk of exclusive non-leptonic decays. For example, the ratio of color-suppressed to non color-suppressed branching fractions listed in Table 6.7 are in dramatic disagreement with the predicted value [56]. Also the results obtained from a fit to a large sample of charmed decays gives a value of $\xi = 0$ which implies $N_c = \infty$. This corresponds to dropping the contribution from the color mismatched 4-quark operator altogether and seems to suggest that the non-factorizable contributions cancel the contributions from the

$$\frac{1}{N_c} C_2 \langle Dh|\mathcal{O}_1|B\rangle$$

term. In charm decays, however, the situation is complicated by final state interactions since the low momentum transfers allow for the possibility of final state rescattering before the hadrons have moved significantly far away from the strong interaction region. Measurements of these parameters in the B system, where final state interaction are believed to play a less significant role could shed some light as to the role played by the non-factorizable contributions to heavy quark decays [57].

6.4.1 Determination From Branching Fractions Measurements

To determine the the values of the parameter a_1, the magnitude and sign of a_2/a_1 we use the branching fraction measurements in Tables 6.1, 6.2 and the theoretical predictions from Neubert *et al.* and Deandrea *et al.* [19,23]. The theoretical predictions, listed in Table 6.8, have been rescaled to accommodate common values of $f_D = 220$ MeV, $V_{cb} = 0.041$ and $\tau_B = 1.44$ ps [58]. In the Neubert *et al.* approach the heavy quark symmetries, with mass corrections, are employed in determining the form factors in heavy to heavy $(B \to D)$

Table 6.8

Table of theoretical predictions for B branching fractions

B Mode	$\mathcal{B}_{th}$ (%) BSW II	$\mathcal{B}_{th}$ (%) CDDFGN
$D^+\pi^-$	$0.264a_1^2$	$0.278a_1^2$
$D^+\rho^-$	$0.621a_1^2$	$0.717a_1^2$
$D^{*+}\pi^-$	$0.254a_1^2$	$0.278a_1^2$
$D^{*+}\rho^-$	$0.702a_1^2$	$0.949a_1^2$
$D^0\pi^-$	$0.265(a_1+1.230a_2)^2$	$0.278(a_1+1.127a_2)^2$
$D^0\rho^-$	$0.662(a_1+0.662a_2)^2$	$0.717(a_1+0.458a_2)^2$
$D^{*0}\pi^-$	$0.255(a_1+1.292a_2)^2$	$0.278(a_1+1.524a_2)^2$
$D^{*0}\rho^-$	$0.703(a_1^2+0.635a_2^2+1.487a_1a_2)$	$0.949(a_1^2+0.53a_2^2+1.31a_1a_2)$
$D^0\pi^0$	$0.201a_2^2$	$0.502a_2^2$
$D^0\eta$		$0.147a_2^2$
$D^0\eta'$	$0.030a_2^2$	
$D^0\rho^0$	$0.136a_2^2$	$0.077a_2^2$
$D^0\omega$	$0.264a_2^2$	$0.077a_2^2$
$D^{*0}\pi^0$	$0.201a_2^2$	$0.405a_2^2$
$D^{*0}\eta$	$0.264a_2^2$	$0.097a_2^2$
$D^{*0}\eta'$	$0.030a_2^2$	
$D^{*0}\rho^0$	$0.136a_2^2$	$0.270a_2^2$
$D^{*0}\omega$	$0.264a_2^2$	$0.270a_2^2$

Note: Branching fractions in terms of the BSW parameters with $f_D = 220$ MeV, $\tau_B = 1.44$ ps and $|V_{cb}| = 0.041$ [58].

transitions. For heavy to light ($B \to h$) transitions, they use a slightly modified version of the original BSW model where the form factors F_0 and A_1 remain monopole types and the F_1, A_0, A_2 and V form factors have dipole type q^2 dependence. Deandrea *et al.* use exact heavy quark symmetry to extract the form factors in heavy to heavy transitions by extrapolating the Isgur-Wise function from the symmetry point using an improved form of the relativistic oscillator model. The heavy to light form factors are estimated by use of heavy quark and chiral symmetries with mass corrections and monopole type q^2 dependence for all form factors. These models will henceforth be referred to as BSW II and CDDFGN respectively [57,50].

In class I decays, the branching fractions are proportional to the BSW parameter a_1^2. By performing a least squares fit of the branching fractions, $B^0 \to D^+\pi^-, D^{*+}\pi^-, D^+\rho^-$ and $D^{*+}\rho^-$ to the theoretical prediction of BSW II and CDDFGN we obtained

$$\begin{aligned} |a_1| =& 1.18 \pm 0.025 \pm 0.023 \pm 0.198 \quad \text{BSWII} \\ |a_1| =& 1.09 \pm 0.023 \pm 0.021 \pm 0.183 \quad \text{CDDFGN.} \end{aligned} \tag{6.8}$$

The first error is statistical, the second error is the systematic error obtained in the least sqaures fit and includes both branching fraction systematic errors, the third error is due to the uncertainty in the B meson production fractions and lifetimes

$$\frac{f_+\tau_+}{f_0\tau_0} = 1.14 \pm 0.14 \pm 0.13[15].$$

The theoretical uncertainties were not included in the systematic errors.

The relative sign and value of a_2/a_1 can be extracted by comparing class III decays to class I decays by forming the following ratios of branching fractions

$$\begin{aligned}
R_1 &= \frac{\mathcal{B}(B^- \to D^0\pi^-)}{\mathcal{B}(\bar{B}^0 \to D^+\pi^-)} = \left[1+\beta_1\frac{a_2}{a_1}\right]^2 \\
R_2 &= \frac{\mathcal{B}(B^- \to D^0\rho^-)}{\mathcal{B}(\bar{B}^0 \to D^+\rho^-)} = \left[1+\beta_2\frac{a_2}{a_1}\right]^2 \\
R_1 &= \frac{\mathcal{B}(B^- \to D^{*0}\pi^-)}{\mathcal{B}(\bar{B}^0 \to D^{*+}\pi^-)} = \left[1+\beta_3\frac{a_2}{a_1}\right]^2 \\
R_1 &= \frac{\mathcal{B}(\bar{B}^0 \to D^{*0}\rho^0)}{\mathcal{B}(\bar{B}^0 \to D^{*+}\rho^-)} = \left[1+\beta_4\left(\frac{a_2}{a_1}\right)^2+\xi_4\frac{a_2}{a_1}\right]
\end{aligned} \tag{6.9}$$

The numerical constants β_i and ξ_i multiplying the a_2/a_1 terms are functions of the various form factors and decays constants which enter in the covariant decomposition of the amplitudes (see Chapter 2). The theoretical predictions from the BSW II and CDDFGN models are also listed in Table 6.8. The values were used in separate least squares fits to Equations (6.9) and give

$$\begin{aligned}
\frac{a_2}{a_1} &= +0.15 \pm 0.032 \pm 0.043 \pm 0.025 \quad \text{BSWII} \\
\frac{a_2}{a_1} &= +0.16 \pm 0.031 \pm 0.041 \pm 0.027 \quad \text{CDDFGN}
\end{aligned} \tag{6.10}$$

In the fit we ignored the theoretical uncertainties in R_1 through R_4. The systematic errors were first estimated for each ratio separately and then used as weights in the least squares fit. The results both obtain a positive value for the relative sign of a_2/a_1 and are in good agreement in magnitude.

The model predictions for the ration R_4 are believed to be unreliable [58]. To account for this we performed the fit a second time using only the ratio $R_1 - R_3$. The results,

$$\begin{aligned}
\frac{a_2}{a_1}(R_1 - R_3) &= +0.13 \pm 0.034 \pm 0.081 \pm 0.022 \quad \text{BSWII} \\
\frac{a_2}{a_1}(R_1 - R_3) &= +0.15 \pm 0.032 \pm 0.057 \pm 0.025 \quad \text{CDDFGN}
\end{aligned} \tag{6.11}$$

do not differ significantly from the result obtained with all four ratios.

The fits to data described above do not include theoretical uncertainties in calculating the form factors which are quite large (on the order of 50% in some modes). Also, the expected variation between naive factorization and the rule for discarding the $1/N_c$ term in class I amplitudes may not apply for class II amplitudes. These uncertainties renders the global fit procedure somewhat questionable since it relies on ratios of class I decays to class III decays the latter containing both types of amplitudes. To examine the relative sign of a_2 and a_1 Gourdin *et al.*use a method which relies on class III decays only [57]. Their method consists of plotting the allowed region in the a_1, a_2 plane and then look for a non-empty intersection of the allowed domain. In their paper they compare three theoretical models, including BSW II and CDDFGN, already discussed and the original BSW model which they refer to as BSW I. Their plots were recreated with the branching fraction results and numerical predictions listed in Table 6.8 and in Ref. [57].

The plots were made by plotting the 1σ standard deviation results for the branching ratios of class III modes $B^- \to D^0\pi^-$, $D^0\rho^-$ and $D^{*0}\rho^-$. The union of all four bands gives the allowed region for the values of a_1 and a_2. Both the BSW II and CDDFGN models have common intersection domains which intersect in the positive region of a_2 and a_1.

To further constrain the allowed region of a_1 and a_2 we superimposed the a_1 bands from class I decays. The theoretical prediction for the three models considered are also obtained from Ref. [57] and from the values in Table 6.8. The union of all bands gives a graphical indication of how well the data are fit by the theoretical models.

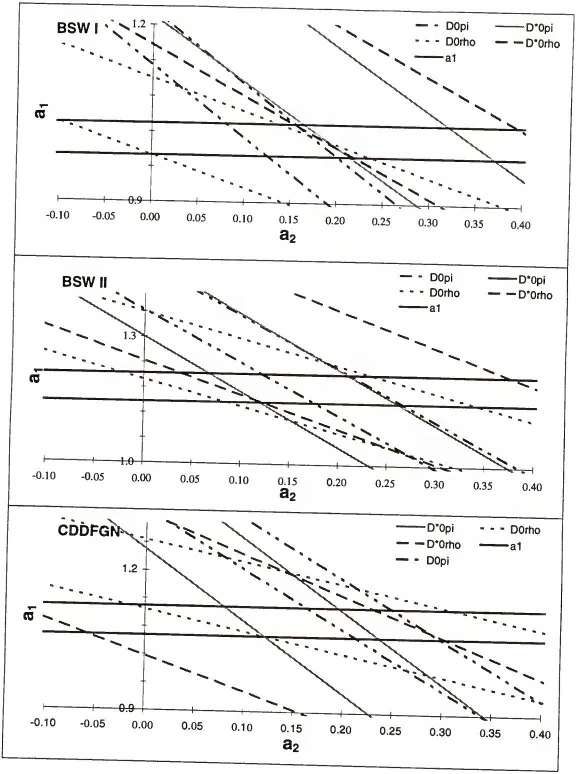

Figure 6.14 Branching fractions of class III modes in the a_1, a_2 plane.

Table 6.9

Theoretical predictions of ρ_L in $B^- \to D^{*0}\rho^-$

ρ_L (FW)	$\zeta = a_2/a_1$	-0.25	-0.20	0.20	0.25
HQET I	BSW II	0.902	0.895	0.839	0.833
	CDDFGN	0.890	0.887	0.839	0.833
	PB	0.899	0.893	0.843	0.838
HQET II	BSW II	0.903	0.894	0.834	0.827
	CDDFGN	0.896	0.890	0.831	0.824
	PB	0.903	0.894	0.837	0.832

6.4.2 Determination From $B^- \to D^{*0}\rho^-$ Polarization

Recently, Keum has pointed to another method of determining the relative sign of a_2/a_1 [50]. His method consists of relating the polarization state in class III vector-vector decays to the decay amplitude which depends on both a_1 and a_2. In particular, the analysis uses the $B^- \to D^{*0}\rho^-$ decay mode.

The longitudinal polarization is related to the amplitudes by

$$\rho_L = \frac{\Gamma_{LL}}{\Gamma} = \frac{|A_{LL} + \zeta B|^2}{\sum_\lambda |A_{\lambda\lambda} + \zeta B_{\lambda\lambda}|} \tag{6.12}$$

where $\zeta = a_2/a_1$, $A_{\lambda\lambda}$ and $B_{\lambda\lambda}$ are the amplitudes for the color-matched and color-mixed amplitudes in a particular helicity state. From the expression above several prediction for the longitudinal polarization were made. In obtaining the predications, factorization is assumed, the effects from final state interactions are ignored and the calculations were done using both zero and finite width approximation for the ρ^- mass. The results obtained, in the finite ρ width approximation, are listed in Table 6.9.

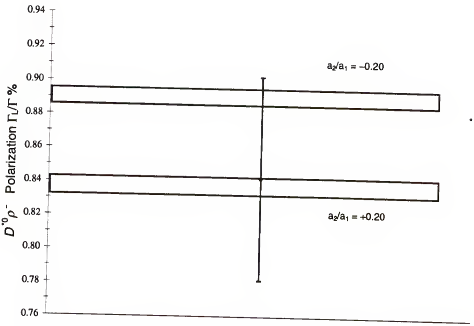

Figure 6.15 The longitudinal polarization in $B^- \to D^{*0}\rho^-$ decays.

The amplitudes used in evaluating Equation (6.12) are computed with hadronic form factors as derived in several theoretical models. In calculating the heavy to heavy $B \to D^*$ form factors, the set of predictions labeled HQET I (as in CDDFGN) are associated with exact heavy quark symmetry. The HQET II predictions include mass corrections (as in BSW II). In computing the heavy to light $B \to \rho$ transitions, BSW II and the CDDFGN are the models already described. In the PB model, monopole and constant terms are assumed for the q^2 dependence of the factors factors [50].

The measurement of the longitudinal polarization in $B^- \to D^{*0}\rho^-$ was discussed in Section 6.2.1 and the value obtained was

$$\rho_L = \frac{\Gamma_L}{\Gamma} = 84.2 \pm 5.08 \pm 4.2\%.$$

This value is compared with the theoretical predication in Figure 6.15. The bands represent the minimum and maximum predictions taken from Table 6.9 for positive and negative $\zeta = 0.20$ values. Our measurement is not sufficiently precise to distinguish between positive and negative values of ζ. The error bars represents the 1σ statistical error.

6.5 Color Suppression

Two types of weak decay diagrams dominate the decay processes of heavy flavor mesons. The external diagram mediates class I decays and is described by the production of a light meson from the hadronization of quark pairs produced at the W vertex. The internal diagram mediates class II decays and the quarks produced at the W vertex hadronize into separate mesons which imposes color matching requirements on the color fields. The color matching requirement implies that class II decays are suppressed relative to class I decays. From simple color counting we expect a suppression rate of

$$\frac{\Gamma(\bar{B}^0 \to D^0\pi^0)}{\Gamma(\bar{B}^0 \to D^+\pi^-)} \sim \frac{1}{2}\left(\frac{1}{9}\right)$$

where the additional factor of 1/2 comes from the π^0 wavefunction.

The naive expectation is modified by hard gluon corrections. If we assume strict factorization we can ignore the non-factorizable terms in the effective Hamiltonians, Equations (¿¿effHa1¡¡) and (¿¿effHa2¡¡), and write the ratios of partial widths in terms of matrix elements and QCD coefficients a_1 and a_2

$$\frac{\Gamma(\bar{B}^0 \to D^0\pi^0)}{\Gamma(\bar{B}^0 \to D^+\pi^-)} \simeq \frac{1}{2}\left|\frac{a_2}{a_1}\right|^2 = \frac{1}{2}\left|\frac{C_2 + \frac{1}{N_c}C_1}{C_1 + \frac{1}{N_c}C_2}\right|^2 . \qquad (6.13)$$

If we use the LLA results

$$C_1 = 1.12 \qquad \text{and} \qquad C_2 = -0.270$$

Table 6.10

Table of ratio of class II to class I B decays

Ratio of branching fractions	UL (90% C.L.)	BSWII	CDDFGN
$\mathcal{B}(\bar{B}^0 \to D^0\pi^0)/\mathcal{B}(\bar{B}^0 \to D^+\pi^-)$	< 0.11	0.0129	0.0406
$\mathcal{B}(\bar{B}^0 \to D^0\eta)/\mathcal{B}(\bar{B}^0 \to D^+\pi^-)$	< 0.11		0.0119
$\mathcal{B}(\bar{B}^0 \to D^0\eta')/\mathcal{B}(\bar{B}^0 \to D^+\pi^-)$	< 0.09	0.0019	
$\mathcal{B}(\bar{B}^0 \to D^0\rho^0)/\mathcal{B}(\bar{B}^0 \to D^+\rho^-)$	< 0.07	0.0037	0.0024
$\mathcal{B}(\bar{B}^0 \to D^0\omega)/\mathcal{B}(\bar{B}^0 \to D^+\rho^-)$	< 0.07	0.0072	0.0024
$\mathcal{B}(\bar{B}^0 \to D^{*0}\pi^0)/\mathcal{B}(\bar{B}^0 \to D^{*+}\pi^-)$	< 0.18	0.0134	0.0328
$\mathcal{B}(\bar{B}^0 \to D^{*0}\eta)/\mathcal{B}(\bar{B}^0 \to D^{*+}\pi^-)$	< 0.16	0.0176	0.0079
$\mathcal{B}(\bar{B}^0 \to D^{*0}\eta')/\mathcal{B}(\bar{B}^0 \to D^{*+}\pi^-)$	< 0.44	0.0020	
$\mathcal{B}(\bar{B}^0 \to D^{*0}\rho^0)/\mathcal{B}(\bar{B}^0 \to D^{*+}\rho^-)$	< 0.14	0.0033	0.0064
$\mathcal{B}(\bar{B}^0 \to D^{*0}\omega)/\mathcal{B}(\bar{B}^0 \to D^{*+}\rho^-)$	< 0.14	0.0064	0.0064

Note: The values of a_2/a_1 used are from Equation (6.10).

we get a suppression factor of 1/200. This results is extremely sensitive to the precise values of the QCD coefficients due to the cancelation of the coefficients in the numerator. For example, the NNLA values gives a suppression factor of 10^{-3}. Other factors such as the precise value of the form factors and the effects of final-state interactions influence the suppression although these tend to be small as can be seen by inspecting the theoretical prediction in Table 6.8.

We set upper limits on color-suppression by taking ratios of class II to class I decays. In Table 6.10 the upper limits at the 90% confidence level are shown. The comparison is made between modes with similar particle content to reduce the systematic errors, some of which cancel in the ratio. Also listed in Table 6.10 are the predictions of Neubert *et al.* and Deandrea *et al.* where the ratios of the BSW parameters a_2/a_1 from Equation (6.11) were used instead of the QCD parameters used in the estimate above. The upper limits listed in Table 6.10are consistent with color-suppression, however the large uncertainties in both the experimental parameters a_2/a_1 and the theoretical models makes it difficult to estimate the expected rate. Both models are consistent with our results.

CHAPTER 7
SUMMARY AND CONCLUSIONS

Using 2,040 pb^{-1} of data collected with the CLEO II detector, we have reconstructed twenty-two decay modes of the B meson, exclusively, in three D^0 and one D^+ decay mode. The large sampled allowed the measurement of branching fractions for twelve of these modes to an accuracy limited, in some modes, only by the systematic errors associated with the branching fraction measurements on charm decays. Two B decay mode branching fractions, the $B^- \to D^0 a_1^-$ and the $\bar{B}^0 \to D^+ a_1^-$ were measured for the first time.

Nine of the twelve non color-suppressed decay modes measured contained a D^0 in the decay chain. For each of these, a new measurement was provided by the $D^0 \to K^-\pi^+\pi^0$ subdecay mode for the first time. All of the branching fraction measurements are listed in Tables 6.1 through 6.3. They form the most precise measurements so far for this important class of decays.

The precision measurements were used to test the factorization hypothesis by comparing class I decays, $B^0 \to D^{*+}h^-$, to semileptonic decays at appropriate q^2. The results were found to be consistent with factorization. In addition, $90.2 \pm 3.7 \pm 4.5\%$ of the $\bar{B}^0 \to D^{*+}\rho^-$ decays were found to be longitudinally polarized also in agreement with the factorization hypothesis.

Th branching fraction measurements were also used to determine the BSW parameters $|a_1|$ and the magnitude and sign of a_2/a_1. The values were obtained by fitting to the branching fractions to two theoretical models. These values are listed below.

	BSW II	CDDFGN
$\lvert a_1 \rvert$	$1.18 \pm 0.025 \pm 0.023 \pm 0.198$	$1.09 \pm 0.023 \pm 0.021 \pm 0.183$
a_2/a_1	$+0.15 \pm 0.032 \pm 0.043 \pm 0.025$	$+0.16 \pm 0.031 \pm 0.041 \pm 0.027$

The positive value for a_2/a_1 differ from the expectation extrapolated from measurements performed on charmed decays. In charm decays the fit to data imply that the non-factorizable terms contribute in such a way as to cancel the effect from the $1/N_c$ term. Extrapolating this to B decays we expect a negative value of a_2/a_1 which is not obtained by the fit to data.

The large sample of $B\bar{B}$ events was also used to search for ten color-suppressed decays of the B mesons to a single charmed plus a light neutral meson. The modes examined were

$$\bar{B}^0 \to D^0\pi^0 \quad \bar{B}^0 \to D^0\eta \quad \bar{B}^0 \to D^0\eta' \quad \bar{B}^0 \to D^0\rho^0 \quad \bar{B}^0 \to D^0\omega$$

$$\bar{B}^0 \to D^{*0}\pi^0 \quad \bar{B}^0 \to D^{*0}\eta \quad \bar{B}^0 \to D^{*0}\eta' \quad \bar{B}^0 \to D^{*0}\rho^0 \quad \bar{B}^0 \to D^{*0}\omega.$$

While no signals were obtained our results showed that color-suppression is active in B mesons according to theoretical expectations. The upper limits set are about a factor of 20 higher than the expectation from naive factorization.

In the near future, the large data sample will be used to further investigate the properties of the B mesons. This includes additional modes such Cabibbo suppressed decays, double D decays and perhaps the addition of other D meson subchannels. Currently, none of the color-suppressed modes have been observed but an intriguing enhancement is seen in one of the D^0 submodes in the $\bar{B}^0 \to D^0\pi^0$ channel. This mode is currently under investigation.

APPENDIX A
MEASUREMENT OF IMPACT PARAMETER SPREAD

Introduction

The spread in the impact parameter varies as a function of both momentum and azimuthal angle ϕ (FICD). The impact parameter (DBCD) of a track is defined as its point of closest approach to the beam spot (see Figure 4.4). The sign of DBCD gives the direction of the track with respect to the displacement from the beam spot. Usually, in CLEO analyses a five or six millimeter cut is placed on a track's impact parameter, independent of its momentum or azimuthal angle. We can improve this selection criteria by imposing a DBCD cut which depends on both the track momentum and angle since the spread in impact parameter varies considerably over both these quantities. In order to use a momentum and ϕ dependent DBCD cut however, we must first measure the dependence of the spread in data. In this appendix we describe the analysis procedure used to measure the spread and also discuss the shift in the mean of DBCD for tracks which is also a function of momentum. After the measurements were performed a set FORTRAN routines were created that return the value of the width of the spread and the shift in the mean of DBCD as a function of momentum and track azimuthal angle ϕ. These routines were used in the B analysis to select tracks from the origin in lieu of the standard flat cut.

The momentum and ϕ dependence of the spread in the impact parameter can be expressed as

$$\sigma^2_{\mathrm{DBCD}}(p,\phi) = \sigma^2_T(p) + \sigma^2_{x_b}\sin^2\phi + \sigma^2_{y_b}\cos^2\phi. \tag{A.1}$$

Here the angular dependence of the overall DBCD spread is assigned to the beam spread with the terms $\sigma_{x_b}, \sigma_{y_b}$ and the momentum dependence is assigned to the σ_T term. All three components, added in quadrature, describe the functional form of the overall spread.

The momentum dependence of the impact parameter (σ_T) is dominated by multiple scattering for tracks that originate at the primary vertex. As a particle traverses detector material, its trajectory is deflected by the influence of the nuclei it encounters. The sum of these deflections, for small angles, follows roughly a Gaussian distribution where the root-mean-square deflection is given by

$$\theta_{rms} = \frac{21\mathrm{MeV}}{\beta cp}\sqrt{\frac{t}{X_0}}, \tag{A.2}$$

here θ_{rms} is deflection angle from the normal to the plane of incidence, X_0 is the radiation lengths and t is the thickness of the media being traversed. The momentum dependence of the r.m.s deflection thus influences the momentum dependence of the impact parameter spread since the spread is the r.m.s distance between the track's point of closest approach and the beam spot. Other factors, such as poorly reconstructed tracks and non-primary vertex decays also contribute to the impact parameter spread. To allow for these factors the momentum dependence of the spread was not taken directly from the multiple scattering form, instead the function

$$\sigma_T(p) = \frac{A}{p^{1.3}} + Bp + C \tag{A.3}$$

was used where the parameters A, B and C were determined from fits to data. The functional form of Equation (A.3) was found to adequately fit the data.

A.1 Data Sample and Analysis Procedure

The data used consisted of 4s2 through 4s8 hadronic sample used in the B meson analysis. To limit the number of events, only 1000 events were taken from each run. Track selection requirements were also kept minimal. The only selection requirement imposed was that the tracks hit at least 10 layers in the drift chamber. In addition a 40,000 $B\bar{B}$ event sample of production Monte Carlo events used to verify that the Monte Carlo simulated the data well.

The momentum dependence of the spread in DBCD was determined by measuring the standard deviation of DBCD as a function of momentum at a fixed azimuthal angle $|\cos\phi| \leq 0.96$. The distributions for a selection of the 4s2 data are shown in Figure A.1 [59]. The distributions were fitted to a double Gaussian plus a Chebychev polynomial where the width of the secondary Gaussian was constrained with respect to the primary. The standard deviations for each of the DBCD distributions were then plotted as a function of momenta and fit to Equation (A.3). As a consistency check the 4s2 impact parameter spreads were refit with a single Gaussian plus a higher order Chebychev polynomial. The widths obtained did not change significantly but the χ^2 for the fits were much worse.

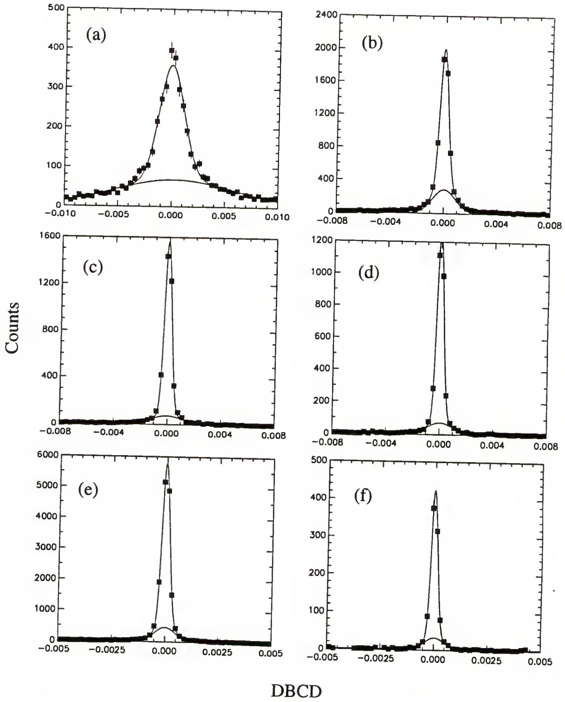

Figure A.1 The impact parameter as a function of momenta.

The momenta of the tracks increase from (a) to (f). The width of the momentum bins were 100 MeV for all but the last two bins which are 500 MeV MeV and 2.0 GeV respectively. The momentum bins are centered about (a) 110 MeV, (b) 400 MeV, (c) 700 MeV, (d) 850 MeV, (e) 1.75 GeV and (f) 4.0 GeV.

The impact parameter spread verses momentum distributions determined by the double Gaussian fits are shown in Figure 4.5 for each of the 7 data sets plus the 4s2-4s3 $B\bar{B}$ Monte Carlo. The value of the fit parameters can be found in Ref. [59]. To insure that the momentum dependence was well modeled for low momentum tracks the lowest momentum bin in the 4s2 sample was divided into 20 MeV bins centered at 70 MeV, 90 MeV, 110 MeV and 170 MeV. The DBCD spread verses momentum distributions were then refit to Equation (A.3). The results obtained did not change appreciably from the large low momentum bin results. Figure 4.5 shows the variation in the spread of from data set to data set. The maximum variation is approximately 60 microns at 1.0 GeV between the 4s8 and 4s3 data samples. The variations between data sets are automaticly included in the FORTRAN routines.

To measure the azimuthal dependence of the impact parameter spread the momentum was fixed between 1.0 GeV and 1.2 GeV. This momentum interval corresponds to a slowly varying region of the momentum spectrum. The standard deviation of the spread was then measured in $\cos\phi$ bins 0.1 units wide. The combined 4s2-4s4 plus the Monte Carlo data were fit as before and the standard deviations were plotted as a function of $\cos\phi$. The two plots, Figure A.2 (a) and (b) were fit to the square-root of equation (A.1)

$$\sigma_{\mathrm{DBCD}} = \sqrt{\sigma_T^2 + \sigma_{x_b}^2(1-\cos^2\phi) + \sigma_{y_b}^2\cos^2\phi} \tag{A.4}$$

with the value of σ_{y_b} fixed to the known beam spread in y.† The value of the spread in x, the fit parameter σ_{x_b}, is the x component of the overall spread

† The 30 micron value used in the fit to Monte Carlo data is the default QQ value. The 5.6 micron value used in the fit to data is the CESR beam dimension in y divided by $\sqrt{2}$.

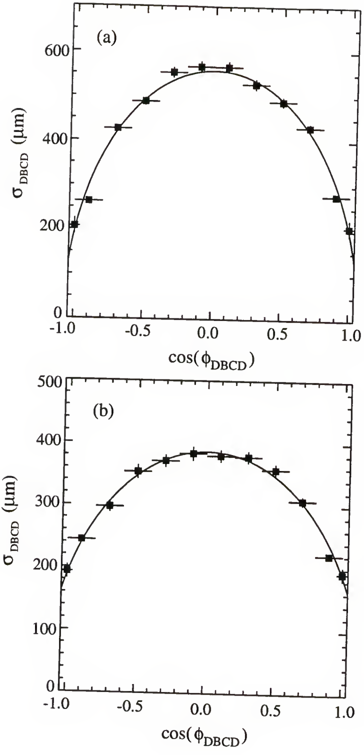

Figure A.2 The azimuthal dependence of the spread in DBCD. The fitted distribution in (a) Monte Carlo and in (b) 4s2-4s4 data.

due to the spread of the colliding beams in the horizontal direction (σ_h). The value obtained was

$$\sigma_{x_b} = 336.1 \pm 11.3 \pm 14.0.$$

As a check, the horizontal beam spread obtained from Monte Carlo was compared with the known QQ default value of 500 microns. The value obtained from the fit to Monte Carlo data was 520.9 microns. The difference between the fit result and the default QQ value was used as the systematic error.

A.2 Shift in Mean of DBCD

Mike Zoeller performed a similar analysis on the momentum dependence of DBCD [60]. He found a track sign and momentum dependent shift of the mean of DBCD which was clearly visible for low momentum tracks. In Figure A.3 (a) and (b) the DBCD distributions for positive and negative low momentum tracks, in 4s2 data, are shown together with the Monte Carlo predictions for the momentum dependence of the shift, Figure A.3 (c).

The track-sign dependence of the shifts can be understood if we both the sign convention of DBCD and the effect of energy losses on charged track curvatures. The energy loss effect is shown in Figure A.4. Without energy losses, both of the tracks in Figure A.4 have equal but opposite values of DBCD. Energy losses increase the curvature of the tracks affecting the track on the left-hand differently than the track on the right. The track on the left side of the beam-spot, which is defined to be positive, moves towards the beam-spot. The track whose point of closest approach lies on the other side is shifted away from the beam-spot. Thus tracks with the same sign but with

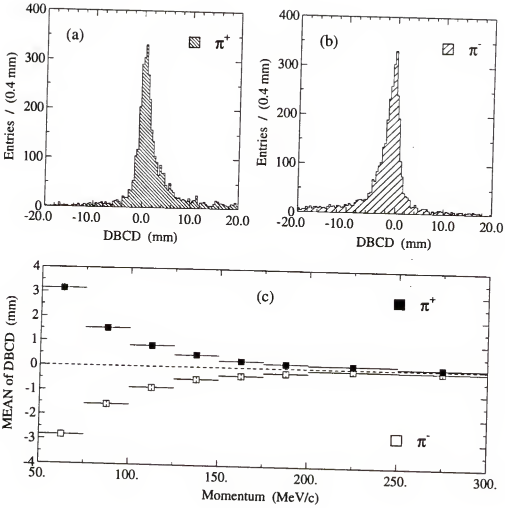

Figure A.3 Shift in mean of DBCD for positive and negative tracks.

The DBCD distributions for (a) positive and (b) negative low momentum pions. In (c) the Monte Carlo predictions for the momentum dependence of the shift in the mean of DBCD for low momentum $\pi^{\pm}$ [60].

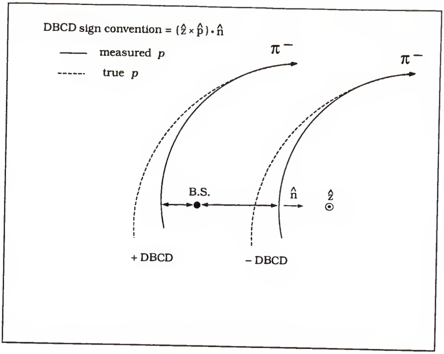

Figure A.4 The effect of energy losses on primary tracks.

points of closest approach on opposite sides of the beam-spot are shifted from zero in one direction or the other depending on the sign of the track.

The shifts in the mean were measured in 4s2 data using a sample of low momentum pions from D^* decays with azimuthal angle $\phi = 0$. Since low momentum tracks can curl multiple times in the large drift chamber volume, the possibility exists that the tracking software will pick up the same track more than once, each time assigning it an opposite charge. These multiply found tracks were found to explain the large asymmetric backgrounds in the distributions of the spread in DBCD (see Figure A.3 (c)). We verified this in Monte Carlo where similar backgrounds were eliminated by requiring that both the impact parameter in the z direction (Z0CD) be less than 1.5 cm and that the charge of the reconstructed track match the charge of the generated track.

APPENDIX B
EFFICIENCY CHECKS

Introduction

Various studies were performed to verify the accuracy of the Monte Carlo simulations and to test the performance of the selection criteria used in the reconstruction procedure. The accuracy of the Monte Simulations is important in extracting absolute branching fractions since Monte Carlo efficiencies were used to correct the event yields. The tracking errors used in the systematic error estimates were determined in these studies. In this appendix we outline the analyses used to verified the Monte Carlo accuracy with references provided to the work performed by various members of the CLEO collaboration. Also, we tested the responce of the Monte Carlo effeciencies and under the particular particle ID consistency requirement used in the B analysis. Finally, we present the analysis used to select the momentum and azimuthal dependent impact parameter cut, testing the performance and verifying the response of the Monte Carlo.

B.1 Monte Carlo Verification Studies

The accuracy of detection efficiencies for charged and neutral tracks were checked in several ways, by various members of the CLEO collaboration. The results are used in all CLEO analyses as an estimate of the accuracy of the Monte Carlo efficiencies. Work on reducing these tracking errors is an ongoing and important process since some analysis are already dominated by systematic errors. In fact, this is case for some of the higher multiplicity modes in the B analysis.

The uncertainty in detection efficiencies for tracks above 225 MeV was determined by measuring the probability of **not** finding two tracks in radiative Bhabha ($e^+e^- \rightarrow \gamma e^+e^-$) events selected using calorimeter information alone. This is then repeated in Monte Carlo and the results are compared [61]. For tracks below 225 MeV the expectation that the decay angle distributions in $D^{*+} \rightarrow D^0\pi^+$ decays are symmetric about zero was used to estimate the uncertainty in detection efficiency. The relative corrections between Monte Carlo and data were compared to arrive at the 5.0% tracking error used it the B meson analysis. To find the uncertainty in the neutral pion detection efficiency the ratio of $\eta \rightarrow \gamma\gamma$ to $\eta \rightarrow \pi^0\pi^0\pi^0$ with $\pi^0 \rightarrow \gamma\gamma$ is measured and compared to the average PDG value. The combined systematic and statistical errors, together with the assumption that the simulation of $\pi^0 \rightarrow \gamma\gamma$ and $\eta \rightarrow \gamma\gamma$ are similar enough so that the ratio of their efficiencies cancel, gives an uncertainty of 5.0% in detection efficiency for single neutral pions [62]. Several other consistency checks including comparisons between full and partially reconstructed $D^0 \rightarrow K^-\pi^+\pi^0$ event, other decay angle distributions tests, other ratio of branching fraction measurements and comparison of inclusive D^{*+} with D^{*0} cross-section were used as well to verify the uncertainty in the detection efficiencies. A synopsis of these analysis is presented, with further references, in Ref. [63].

Table B.1

dE/dx PID efficiency for data and Monte Carlo

p_{D^0} (GeV/c)	ϵ_{MC} (%)	ϵ_{DATA} (%)
$2.0 - 2.5$	97.6 ± 2.9	97.6 ± 4.3
$2.5 - 3.0$	99.0 ± 3.5	98.7 ± 3.9
$3.0 - 3.5$	98.0 ± 3.5	98.3 ± 3.8

B.2 Efficiency Checks of Particle Identification by dE/dx Losses

To insure that cuts based dE/dx particle ID information are accurately modeled in Monte Carlo a check on the efficiency of applying these cuts to both data and Monte Carlo events were compared. The particle ID based cuts were imposed on a sample of high momentum continuum D^{*+}s where the kinematics of the low q^2 decay $D^{*+} \to D^0\pi^+$ can be exploited to yield clean signals before and after application of the dE/dx particle ID cuts. In Table B.1 the efficiencies obtained by applying the 3σ consistency requirement used in the B meson analysis for Monte Carlo and data are listed in three different D^0 momentum regions. The σ here implies a one standard deviation from the measured specific energy loss for a particular particle hypothesis. The results for data and Monte Carlo differ by less than half of a percent for D^0s in the momentum region of relevance to the B meson analysis. This indicats that the effect of a 3σ dE/dx particle ID cut is well modeled by our Monte Carlo simulations.

B.3 Efficiency Checks in $D^{*+} \to D^0\pi^+$ Analysis

To test the performance of the momentum and azimuthal dependent impact parameter cut based on the analysis described in Appendix B we tested various selection criteria on a sample of high momentum D^{*+}s. The D^{*+} was reconstructed in the $D^{*+} \to D^0\pi^+_{slow}$ with $D^0 \to K^-\pi^+$. The performance was tested by comparing the signal and background yields of various cuts a single track in the decay chain to the yield obtained with no impact parameter cut. The performance in Monte Carlo was also checked with the same procedure to test the response of the Monte Carlo under the same selection requirements.

The data used were continuum 4s2-4s4 D^{*+}s ($x_p \geq 0.5$) and a D^{*+} continuum 4s2 Monte Carlo sample. The energy losses of tracks used in reconstructing the D^0 candidates were required to be within 3σ of the K/π hypothesis. In addition events with $|m_{D^{*+}} - m_{D^0} - m_{\pi^+}| \leq 0.0025$ were selected. These selection requirements alone provided a very clean signal in the m_D and m_{D^*} invariant mass distributions and allowed accurate yield measurements.

B.3.1 Efficiency Measurements on Pions From D^0

The efficiency measurements were made by comparing the D^0 invariant mass yields with a cut on the impact parameter (DBCD) of the π^+ from the D^0 decay to the yield obtained without the DBCD cut on any track in the event. The absolute value of the impact parameter was required to within 1,2,3,4 and 5 standard deviations of the measured spread in DBCD. The spread varies as a function of momentum, track azimuthal angle at the origin (ϕ) and run number as described in Appendix A. The invariant mass distributions were fit to a double Gaussian plus a first order Chebychev with all Gaussian parameters,

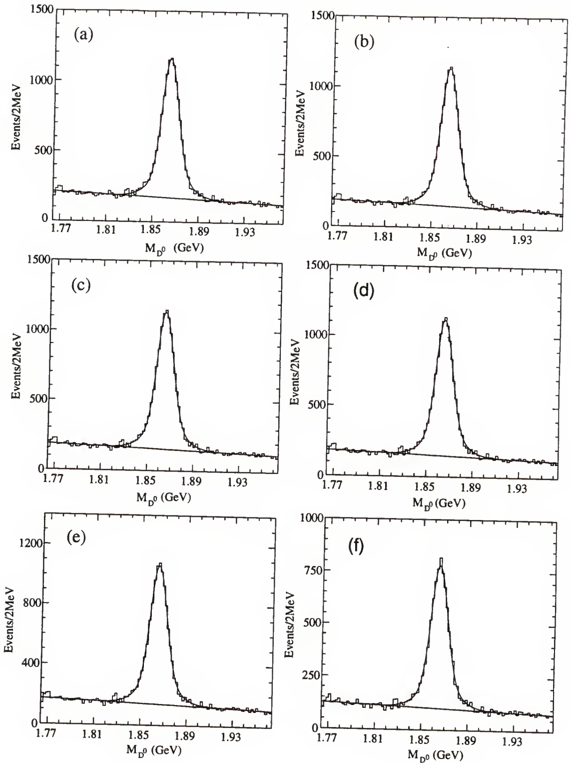

Figure B.1 Fitted D^0 mass spectra for different DBCD cuts.

In (a) the invariant mass distribution without a DBCD cut. In (b-f) the invariant mass distribution with a DBCD cut of 5,4,3,2 and $1\sigma_{\mathrm{DBCD}}$ respectively.

Table B.2

Efficiencies of DBCD cuts on the π^+ in D^0 mass yields

DBCD Cut	ϵ_{mc} (%)	ϵ_{signal} (%)	ϵ_{bkg} (%)	$\frac{S}{\sqrt{S+N}}$
6mm	99.9	99.9	95.1	76.6
5σ	99.4	99.3	89.6	77.2
4σ	99.2	99.0	88.4	77.3
3σ	98.6	97.9	86.2	77.1
2σ	94.3	93.2	80.8	75.5
1σ	68.1	68.5	59.2	64.7

except the area, fixed to the values obtained in the normalization plot. The D^0 mass distributions are shown in Figure B.1 with the five different DBCD requirements (b-f). The plot in Figure B.1 (a) is the normalization plot. The double Gaussian fits are superimposed on each histogram.

The efficiency results for the five different DBCD cuts together with a constant 6 mm cut are listed in Table B.2. Also listed in the table are the results obtained for the Monte Carlo data, the background efficiencies and the signal to noise ratio $S/\sqrt{S+B}$. The background efficiencies were determined by integrating the polynomial functions under the mass peaks. The efficiencies measurements show that the momentum and ϕ dependent DBCD cut improves the signal to noise ratio in the momentum regions above 250 MeV over the flat 6mm cut commonly used. With a 4σ cut the background is reduced by 11.6% while the signal only drops by 0.8% compared to the 6mm cut were only 5% of the background is eliminated with only a slight gain in signal efficiency.

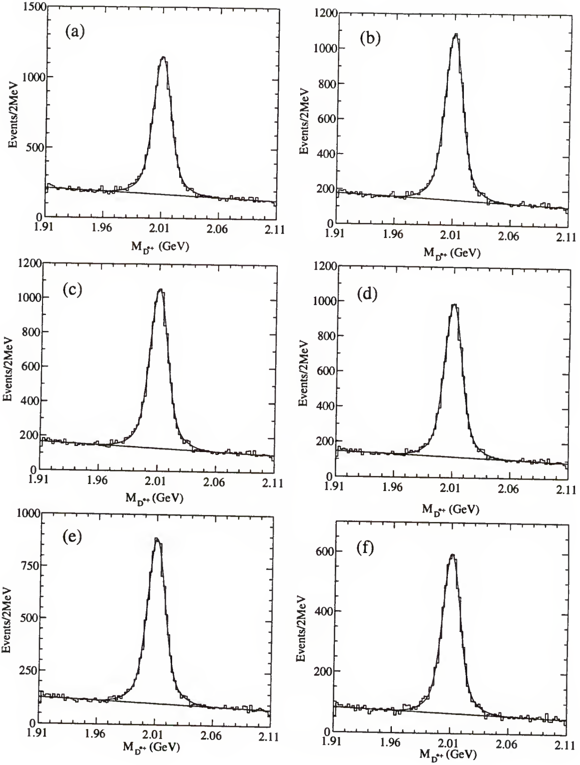

Figure B.2 Fitted D^{*+} mass spectra for different DBCD cuts

In (a) the D^{*+} invariant mass distribution without a DBCD cut. In (b-f) the invariant mass distribution with a DBCD cut of 7,5,3,2 and $1\sigma_{\text{DBCD}}$, respectively.

Table B.3

Efficiencies of the DBCD cuts on the π^+_{slow} in D^{*+} mass yields

DBCD Cut	ϵ_{mc} (%)	ϵ_{signal} (%)	ϵ_{bkg} (%)	$\frac{S}{\sqrt{S+N}}$
6mm	96.8	94.1	73.2	78.1
7σ	96.5	95.3	78.0	77.8
6σ	95.7	94.8	77.2	77.7
5σ	94.8	93.9	75.3	77.5
4σ	93.1	92.4	73.3	77.1
3σ	90.4	89.5	69.0	76.3
2σ	83.1	82.2	61.5	73.5
1σ	59.5	59.4	43.2	62.8

B.3.2 Efficiency Measurements on Slow Pions From D^{*+}

To test the DBCD cut in a different momentum region the same procedure was repeated on the D^{*+} invariant mass distribution with the DBCD cut now imposed exclusively on the bachelor pion (π^+_{slow}) defined to be below 225 MeV. A selection of the invariant mass distributions with various DBCD cuts are shown in Figure B.2. Since the DBCD spread for low momentum tracks is large, an 8 mm DBCD cutoff was imposed in addition to the momentum and ϕ dependent cut. The results for the various cuts on data and Monte Carlo are listed in Table B.3. The reduction in efficiency over that expected for normal distributions is due to the non-Gaussian distribution of the spread in DBCD for low momentum tracks (see Figure A.1 (a)). Imposing a DBCD cut of 7σ reduces the background by 22% while retaining 97% of the signal.

REFERENCES

[1] CDF Collaboration, F. Abe *et al.*, *Fermilab-Pub-95/022-E* (1995).

[2] Particle Data Group, M. Aguilar-Benitez *et al.*, Phys. Rev. D **50**, 1173 (1992).

[3] D. Gross and F. Wilczek, Phys. Rev. Lett. **30**, 1343 (1973); D. Gross and F. Wilczek, Phys. Rev. D **8**, 3633 (1973).

[4] H.D. Politzer, Phys. Rev. Lett. **30**, 1346 (1973).

[5] S. Weinberg, Phys. Rev. Lett. **19**, 1264 (1967); A. Salam, in "*Elementary Particle Theory*," Stockholm, Sweden, edited by N. Svartholm, Almquist & Wiksells, (1968).

[6] All local gauge theories with massless gauge bosons are renormalizable. The renormalizability of gauge theories was proved by 't Hooft for theories with and without spontaneous symmetry breaking. G. 't Hooft, Nucl. Phys. B **33**, 173 (1971); G. 't Hooft, Nucl. Phys. B **35**, 167 (1971).

[7] CFS Collaboration, S. W. Herb *et al.*, Phys. Rev. Lett. **39**, 252 (1977).

[8] CLEO Collaboration, D. Andrews *et al.*, Phys. Rev. Lett. **44**, 1108 (1980).

[9] CUSB Collaboration, T. Bohringer *et al.*, Phys. Rev. Lett. **45**, 1111 (1980).

[10] CLEO Collaboration, C. Bebek *et al.*, Phys. Rev. Lett. **46**, 84 (1981).

[11] CLEO Collaboration, A. Brody *et al.*, Phys. Rev. Lett. **48**, 1070 (1982).

[12] E. Eichten *et al.*, Phys. Rev. D **17**, 3090 (1979); Phys. Rev. D **21**, 203 (1990); J. L. Richardson, Phys. Lett. **B82**, 272 (1979).

[13] W. Buchmüller and S. H. Tye, Phys. Rev. D **24**, 132 (1981).

[14] T. Mannel, G. A. Schuler, CERN preprint CERN-TH. 7523/94 (1994).

[15] CLEO Collaboration, B. Barish *et al.* Phys. Rev. D **51**, 1014 (1995).

[16] CLEO Collaboration, J. Gronberg *et al.*, CLEO CONF 94-6, paper submitted to the a ICHEP94 conference in Glasgow; Also see R. Wang, Ph.D. Dissertation, University of Minnesota (1995).

[17] M. Neubert, Phys. Rept. **245** 259 (1994).

[18] R. Rückl, "Flavor Mixing in Weak Interactions," in *Ettore Majorana International Science Series*, edited by Ling-Lie Chau, Pleum Press, New York (1984).

[19] M. Neubert, V. Rieckert, B. Stech and Q. P. Xu in *Heavy Flavours*, edited by A. J. Buras and H. Lindner, World Scientific, Singapore (1992).

[20] D. M. Coffman, Ph.D. Dissertation, California Institute of Technology (1987).

[21] M. K. Gaillard and B. W. Lee, Phys. Rev. Lett. **33**, 108 (1974); G. Altarelli and L. Maiani, Phys. Lett. **B 32**, 251 (1974).

[22] K. G. Wilson, Phys. Rev. **179**, 1499 (1969).

[23] A. Deandrea, N. Di Bartolomeo, R. Gatto and G. Nardulli, Phys. Lett. **B 318**, 549 (1993).

[24] M.J. Dugan, B. Grinstein, Phys. Lett. **B225**, 583 (1990).

[25] M. Bauer, B. Stech and M. Wirbel, Z. Phys. **C29** 639 (1985).

[26] M. Bauer, B. Stech and M. Wirbel, Z. Phys. **C34** 103 (1985).

[27] B.D. McDaniel, IEEE Trans. on Nucl. Sci., **NS-28**, 1984 (1981).

[28] CLEO Collaboration, Y. Kubota *et al.*, Nucl. Instr. and Meth. **A320** 66 (1992); D. Bortoletto, *et al.*, Nucl. Instr. and Meth. **A320** 114 (1991); D.G. Cassel, *et al.*, Nucl. Instr. and Meth. **A252** 325 (1986).

[29] D.G. Cassel, *et al.*, Nucl. Instr. and Meth. **A252** 325 (1986).

[30] CLEO Collaboration, Y. Kubota *et al.*, Nucl. Instr. and Meth. **A320** 66 (1992).

[31] D. Bortoletto, *et al.*, Nucl. Instr. and Meth. **A320** 114 (1991).

[32] C. Bebek, *et al.*, Nucl. Instr. and Meth. **A302** 261 (1991).

[33] K. Kinoshita, *et al.*, Nucl. Instr. and Meth. **A276** 242 (1989).

[34] CLEO Collaboration, Y. Kubota, *et al.*, Nucl. Instr. and Meth. **A320** 66 (1992); see also E. C. Chu, Ph.D. Dissertation, Cornell University (1991).

[35] Bebek, C. J., *et al.*, Nucl. Instr. and Meth. **A338** 447 (1994).

[36] E. C. Chu, Ph.D. Dissertation, Cornell University (1991).

[37] B. K. Heltsley, "*CLEVER User's Guide*," CLEO Internal Report, CSN 90/281, (1990).

[38] P. Avery *et al.*, "*QQ. A Monte Carlo Generator*," CLEO Internal Report, CSN-85/212.

[39] K. Sparks, "*CLEOG: The CLEO II Monte Carlo*," CLEO Internal Report CSN 89/282 (1989).

[40] R. Brun *et al.*, GEANT 3.14, CERN DD/EE84-1 R.

[41] N. Katayama, "Object Oriented Approach to B Reconstruction (II)," in *Proceedings of the International Conference on Computing in High Energy Physics*," 523-526, edited by C. Verkerk and W. Wojcik, (1992).

[42] G. Fox and S. Wolfram, Phys. Rev. D **41**, 1581 (1978).

[43] Sheldon Stone, "*Exclusive B Decays to $D^* n\pi$*," CLEO Internal Report, CBX 92-74 (1992).

[44] The ARGUS Collaboration, H. Albrecht *et al.*, Z. Phys. C **48**, 543 (1990).

[45] CLEO Collaboration, M. S. Alam *et al.* Phys. Rev. D **50**, 1 (1994).

[46] CLEO Collaboration, F. Butler *et al.* Phys. Rev. Lett. **69**, 2041 (1992).

[47] CLEO Collaboration, D. Akerib *et al.* Phys. Rev. Lett. **71**, 3070 (1993). The systematic error does not include the tracking errors since they are common to this analysis and are already included.

[48] T. Bergfeld, M. Selens. "*A Measurement of $\mathcal{B}(D^0 \to K^-\pi^+\pi^0)/\mathcal{B}(D^0 \to K^-\pi^+)$*," CLEO Internal Report, CBX 95-59, (1995).

[49] CLEO Collaboration, R. Balest *et al.* Phys. Rev. Lett. **72**, 2328 (1994).

[50] Y.Y. Keum, Phys. Lett. **B348**, 247 (1995).

[51] A. Weinstein, "*The Decay Constants f_ρ and f_{a_1} from Tau Decay*," CLEO Internal Report, CBX 95-28 (1995)

[52] The various theoretical models are referenced in: D. Bortoletto and S. Stone, Phys. Rev. Lett. **65**, 2951, (1990).

[53] J. Körner and G. Goldstein, Phys. Lett. **89B**, 105 (1979).

[54] J. L. Rosner, Phys. Rev. D **42**, 3732 (1990).

[55] M. Neubert, Phys. Lett. **B 264**, 455 (1991).

[56] H. Y. Cheng, Int. J. Mod. Phys., **A4**, 495 (1989).

[57] M. Gourdin, A. N. Kamal, Y. Y. Keum, and X. Y. Pham, Phys. Lett. **B 333**, 507 (1994).

[58] T. E. Browder, K. Honscheid, "*B Mesons*," UH 511-816-95, To appear in Progress in Nuclear and Particle Physics, Vol. 35 (1995).

[59] J. L. Rodriguez, "*Momentum and Azimuthal Dependence of Track Impact Paramter Spread*," CLEO Internal Report, CBX94-70, (1994).

[60] M. M. Zoeller, Ph.D. Dissertation, State University of New York at Albany (1994).

[61] Brian K. Heltsley, "*Tracking Inefficiencies*," CLEO Internal Report, CBX 92-107 (1992).

[62] G. Ludwig, CLEO Internal Report, CBX 92-25 (1992).

[63] Dave Besson, "*Charged and Neutral Particle Detection Efficiency in Data and Monte Carlo*," CLEO Internal Report, CBX 93-001 (1993).

BIOGRAPHICAL SKETCH

Jorge Luis Rodriguez was born on that infamous Island whose current leader almost brought the world to the first and probably last nuclear war. Jorge was born in the province of Havana 33 months after Fidel Castro became Cuba's Prime Minister. Sometime in his fourth year, his father acquired the necessary documents to travel abroad. The family moved to Spain for a short time and then immigrated to Miami, Florida where he remained until 1985.

Jorge graduated from Carol City Senior High school in 1980 and received a Powerplant certificate from George T. Baker aviation school were he was simultaneously enrolled. Many important lessons were learned during his years in high school none of them had anything to do with Science. He re-enrolled in George T. Baker shortly after graduating and received an Airframe certificate a year later. Licensed as an aviation technician, he began what was believed a life-long career as an aircraft technician.

After a few years of gainful employment as an aircraft technician, Jorge decided to better himself by once again enrolling in school. This time he decided on Miami-Dade Community College. After graduating with Honors from Miami-Dade, Jorge transfered to the University of Chicago where he received a Bachelors of Arts degree in Physics. He then began graduate work at the University of Florida, in Gainesville, and now hopes to finish his dissertation so that he can get on with his life.

This past June, Jorge married his long time friend and sweetheart Lori Lewis. A few weeks before, Jorge also accepted a postdoctoral position from the University of Hawaii to work on the CLEO and BELLE experiments. He and Lori are currently planning the move to Hawaii. They trust that their new life together will provide many new adventures.

I certify that I have read this study and that in my opinion it conforms to acceptable standards of scholarly presentation and is fully adequate, in scope and quality, as a dissertation for the degree of Doctor of Philosophy.

Paul Avery

Paul R. Avery, Chair
Associate Professor of Physics

I certify that I have read this study and that in my opinion it conforms to acceptable standards of scholarly presentation and is fully adequate, in scope and quality, as a dissertation for the degree of Doctor of Philosophy.

John Yelton

John M. Yelton, CoChair
Associate Professor of Physics

I certify that I have read this study and that in my opinion it conforms to acceptable standards of scholarly presentation and is fully adequate, in scope and quality, as a dissertation for the degree of Doctor of Philosophy.

P. Ramond

Pierre Ramond
Professor of Physics

I certify that I have read this study and that in my opinion it conforms to acceptable standards of scholarly presentation and is fully adequate, in scope and quality, as a dissertation for the degree of Doctor of Philosophy.

R. P. Field

Richard P. Field
Professor of Physics

I certify that I have read this study and that in my opinion it conforms to acceptable standards of scholarly presentation and is fully adequate, in scope and quality, as a dissertation for the degree of Doctor of Philosophy.

Theodore Johnson

Theodore Johnson
Assistant Professor of Computer and Information Sciences

This dissertation was submitted to the Graduate Faculty of the Department of Physics in the College of Liberal Arts and Sciences and to the Graduate School and was accepted as partial fulfillment of the requirements for the degree of Doctor of Philosophy.

August 1995

Richard L. Fuchs

Dean, Graduate school